

Adaptive optics comissioning in O3A and a study of the Pockels effect for an GaAs/Al_{0.92}Ga_{0.08}As mirror coating

by

Daniel Vander-Hyde

B.S. California State University, Fullerton, CA, 2015

M.S. Syracuse University, NY, 2016

Submitted in partial fulfillment of the requirements

For the degree of

Doctor of Philosophy in physics

at

SYRACUSE UNIVERSITY

July 2022

Abstract

Abstract goes here

Dedication

To my brother, Mikey.

Declaration

I declare that

Acknowledgements

Contents

1	Introduction	1
1.1	Gravitational waves	1
1.1.1	Gravitational wave astronomy	1
1.2	Detector configurations	3
1.2.1	Interferometry with a Michelson configuration	3
1.2.2	Fabry-Pérot Michelson (FPMI)	4
1.2.3	Dual-Recycled Fabry-Perot Michelson (DRFPMI)	7
1.3	ALIGO	10
1.3.1	Reaching “Observing Mode”	10
1.4	Coating Thermal Noise	14
1.4.1	Brownian Thermal Noise	15
2	TCS comissioning for O3	20
2.1	Pre-loading for O3a	20
2.2	Optimizing RH thermo-optic response	22
2.2.1	Dynamic Thermal compensation	24
2.3	Point absorbers in O3a	25
2.3.1	Studies	26
2.3.2	Actuation using a CO ₂ laser and mask	26

CONTENTS

3 Electro-optic study of a GaAs/Al_{0.92}Ga_{0.08}As coated mirror	27
3.0.1 Anisotropic media	28
3.0.2 GaAs and Al _{0.92} Ga _{0.08} As crystal classification	32
3.0.3 Induced anisotropy in zincblende crystals	33
3.0.4 Electro-optic modulation	35
3.0.5 Optical anisotropy of a HR GaAs / Al _{0.92} Ga _{0.08} As stack	36
3.0.6 Measured birefringence from HR GaAs/Al _{0.92} Ga _{0.08} As mirrors	39
3.1 Projected DARM coupling	40
3.2 Short, in-air, Pound-Drever-Hall locked, Fabry-Perot cavity experiment	40
3.2.1 PDH servo	42
3.2.2 Servo Parameters	45
3.2.3 Longitudinal Pockels Cell mirror mount assembly	47
3.3 Results	52
3.3.1 Measurement Calibration	53
3.3.2 Mounting Strategies	53
4 Conclusion	63
4.1 Thermal compensation system comissioning for O3	63
4.2 AlGaAs Electro-optic effect	63
5 Appendix	64
5.1 The Equipartition theorem and the Fluctuation dissapation theorem	64
5.2 Mode matching data for Electro-optic sample cavity	65
5.2.1 Pre MMT beam scan	65
5.2.2 “Just another mode matching tool” (JAMMT) solution	66
5.2.3 Post MMT beam scan	66
5.2.4 Laser PZT sweep	67
5.3 Assembly blueprints and alternative views	68

CONTENTS

5.3.1	Assembly 1	68
5.3.2	Assembly 2	70
5.4	Assembly 3 [MACOR](blueprint)	73
5.5	Calibration	73
5.6	Single frequency	88
5.7	Laplace calculator / code	88
5.8	HVA	88
5.9	FSS	88
5.10	Measuring OLG [H]	89
References		89

Chapter 1

Introduction

1.1 Gravitational waves

“Space-time tells mass how to move; mass tells space-time how to curve” provides a sufficient summarization of Einstein’s theory of general relativity [1]. Built into this theory are insights on high energy astrophysical phenomena (highly massive binary coalescences, spherically assymetric compact objects, etc.) one being space-time distortions known as gravitational waves. Explicitly, this is seen as a perturbation in the metric tensor defining a local space-time geometry:

Metric tensor

Refer to GR notes

Information on the progenitors of these systems are encoded in these waves and the detection and study of them open an entirely new chapter in astronomy.

1.1.1 Gravitational wave astronomy

Gravitational wave detection has a history starting with a desire for further experimentation in relativity. The literature provided by those part of this history offers important motivations and details of the field supplemented by fascinating and humbling stories.

CHAPTER 1. INTRODUCTION

As of September 14th 2015 the LIGO detectors transitioned from the most sensitive differential displacement sensors ever built to also becoming the first ever gravitational wave observatory with ?? confirmed gravitational wave detections from O1 to O3b as of the date of the submission of this dissertation. [Figure of detections published from O1 to the end of O3.](#)

1.2 Detector configurations

1.2.1 Interferometry with a Michelson configuration

Initially used by Michelson and Morley for an experiment intended to support the existence of luminiferous aether, the optical design was discovered nearly a century later to lend itself to a gravitational wave detection schema. The perpendicular beam paths set by the beamsplitter and two end mirrors is the novel geometry offered by A. Michelson, and sets an interference condition by the returning beams at the beamsplitter. This condition is disrupted by differential path length changes which can be tracked at the (anti-symmetric) detection port using the following equation:

$$P_{\text{out}} = \frac{P_{\text{in}}}{2}(1 + \cos(2(k_x L_x - k_y L_y))) \quad (1.1)$$

Knowing the Michelson will register a differential arm shift with adjusting fringe brightness, the length response can be reframed into a phase response of the Michelson from a time-dependent metric perturbation:

$$\Delta\phi = \phi_x - \phi_y = \int_{t-2L/c}^t \Omega \left[1 + \frac{1}{2}h(t) \right] dt - \int_{t-2L/c}^t \Omega \left[1 - \frac{1}{2}h(t) \right] dt \quad (1)$$

$$\Delta\phi(\omega) = h_0 \frac{2L\Omega}{c} e^{-iL\omega/c} \frac{\sin(L\omega/c)}{L\omega/c} \quad (1.2)$$

Where $h(t)$ is the time dependent metric perturbation from a gravitational wave with amplitude h_0 angular frequency ω , L is the length of the interferometer arms, c is the speed of light, Ω is the angular frequency of light.

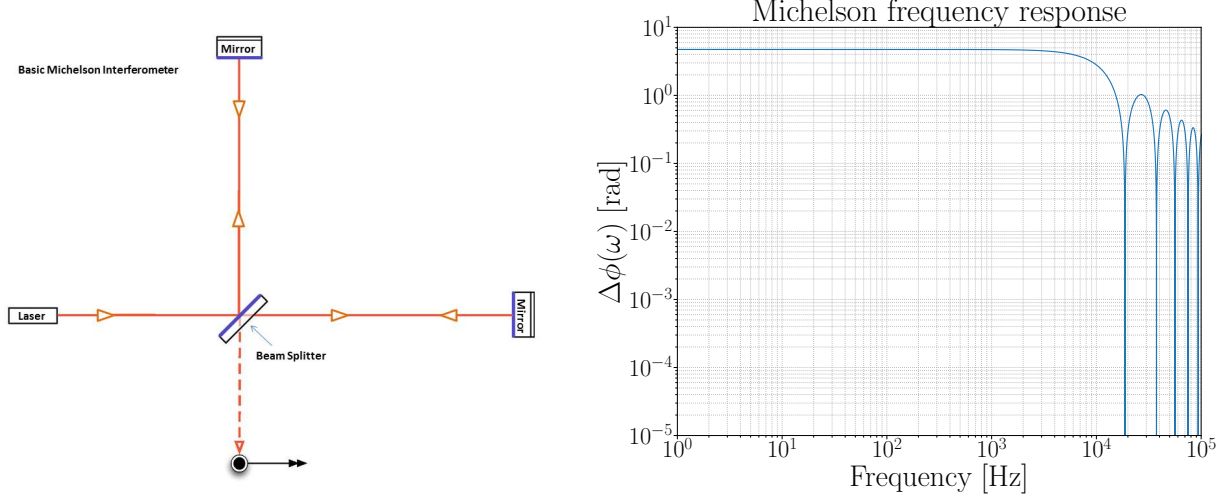


Figure 1.1: **PENDING UPDATE** The simple 4km Michelson with associated differential arm length response (left is optical schema, right is frequency response)

Assuming a LIGO configuration (with 4km arm length), the differential arm response provides a reasonable optical gain proportional to the differential phase until you reach a frequency that correlates to an integer number of gravitational wave half periods $n\lambda_g w/2$ to the interferometer arm length in such a way that the response is null.

1.2.2 Fabry-Pérot Michelson (FPMI)

At the time of proposal, financial and physical constraints for terrestrial gravitational wave detectors required a compact solution for extending arm lengths on the build []. Two proposed techniques were considered: the Delay Line and the Fabry-Perot cavity. Though choice ultimately became the Fabry-Perot cavity.

The Fabry-Pérot cavity

Prior to this discussion, the Michelson interferometer would not provide a sufficient optical gain for any practical arm length, so how does a Fabry-Pérot cavity offer a solution or even relate? To understand we consider an idealized coherent light wave encountering an optical cavity with input and output mirror transmission and reflection coefficients of t_1 , r_1

and t_2, r_2 respectively (and assuming a loss coefficient of $l = 0$).

Figure of Fabry-Pérot cavity

It enters the cavity only after passing the input mirror with a field amplitude reduced by the mirror reflection coefficient. So far this doesn't seem quite useful as we have already reduced the power for the phasefront of interest, until the realization that said phasefront will stay stored within the cavity until its final photon exits the cavity; this "cavity storage time" ($\tau_s \propto Lr_1r_2$) can be imagined as length elongation with the phasefront travel history encoded in the arrival time of the phasefront's photons back at the light source source. But this assumes that the photons of belonging to a particular phasefront can be experimentally tracked, and with a constant source at the cavity input the phasefronts entering the cavity are superimposed onto the circulating cavity field and, more often than not, add incoherently which makes this thought experiment this seem silly. It is with careful microscopic tuning of mirror positions that there can be coherent addition of these intra-cavity phasefronts and the true novel of the Fabry-Pérot can be fully realized. This condition described is known as cavity resonance and appears when deriving the cavity reflection and transmission coefficients:

$$r_c = -r_1 + \frac{t_1^2 r_2 e^{-i2kL}}{1 - r_1 r_2 e^{-i2kL}} \quad (1.3)$$

$$t_c = \frac{t_1 t_2 e^{-ikL}}{1 - r_1 r_2 e^{-i2kL}} \quad (1.4)$$

The storage time of the phasefronts within the cavity can now be correlated to the amplitude of the superimposed intracavity field, which can be measured as a power reflected and/or transmitted from the resonant cavity.

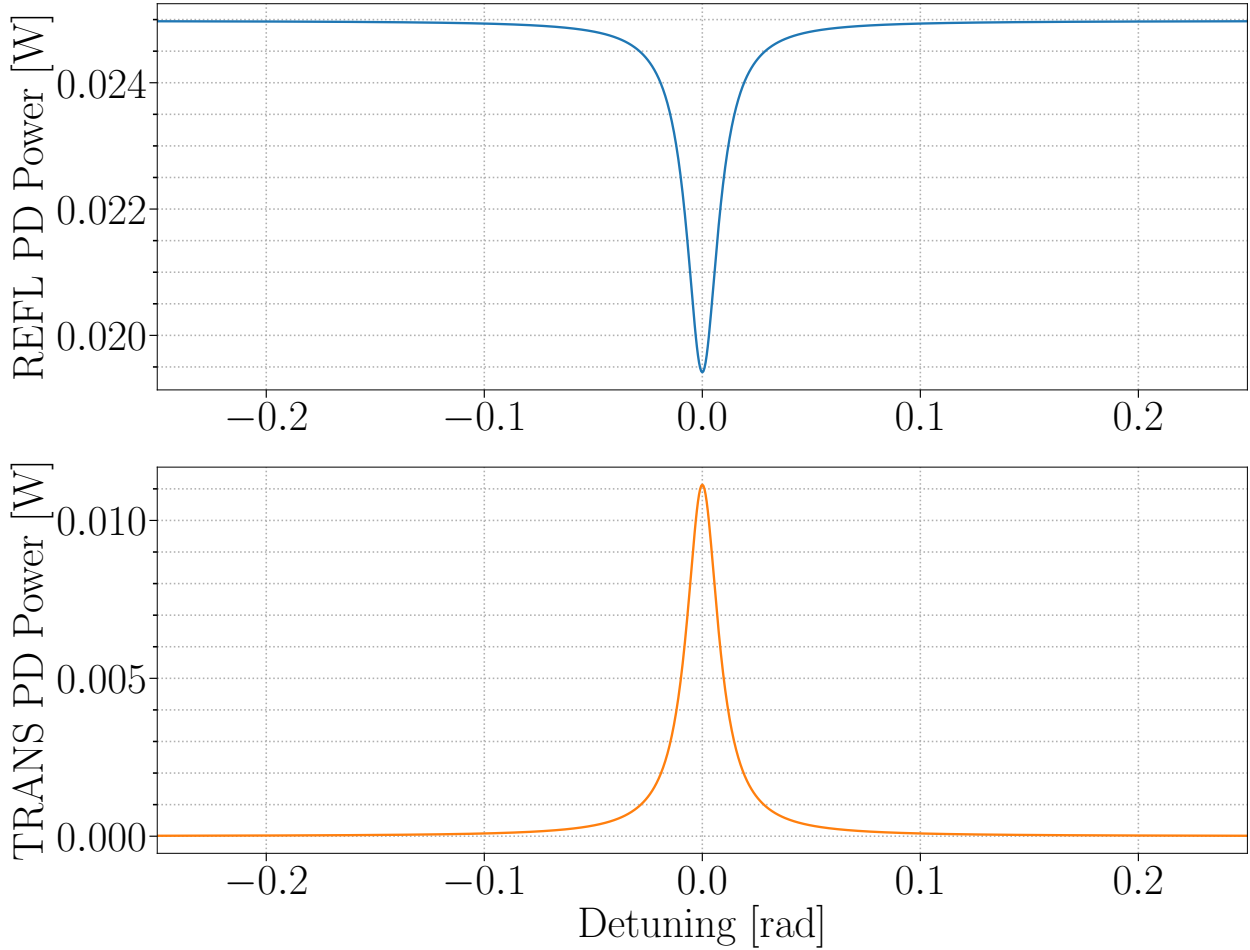


Figure 1.2: Reflected and transmitted power around resonance. Phase as dotted line?. The resonance peak full width half maximum and the cavity free spectral range can be summarized by a cavity parameter defined as the finesse ($F = \frac{\text{FWHM}_{\text{res}}}{f_{\text{FSR}}} = \frac{\pi\sqrt{r_1 r_2}}{1-r_1 r_2}$). The finesse of the cavity used for the figure simulation is ?.

Derived by analogy to the delay line, the Fabry-Pérot cavity storage time (τ_s) is defined in [2] as:

$$\tau_s = \frac{L}{c} \frac{r_1 r_2}{1 - r_1 r_2} \approx \frac{LF}{c\pi} \quad (1.5)$$

You may begin to see that the solution for arm elongation is not answered in a literal sense with the Fabry-Pérot. This is to say that, although there is no physical arm elongation through the usage of Fabry-Perot cavities, a higher sensitivity to differential phase of the light within the cavity for a given cavity length can be achieved and is seen in the difference

in the improved frequency response. Though the reader may view the initial part of this discussion of Fabry-Perot cavities as misleading, the intuition gained when addressing their effectiveness for gravitational wave detectors [3], exhibits the usefulness in this approach.

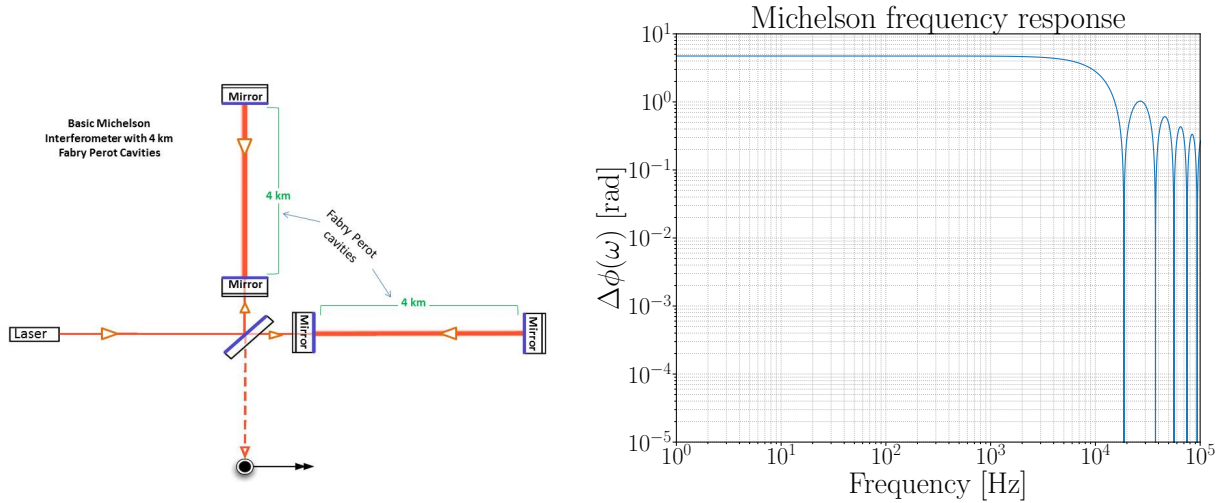


Figure 1.3: **PENDING UPDATE** The Fabry-Perot Michelson optical schema with associated differential arm length response (left is optical schema, right is frequency response)

Advanced LIGO, with it's length and estimated Finesse has a storage time of ?. It's curious how a laser and two mirrors with empty space between them can be such a ubiquitous and invaluable tool in experimental science, though its application for high sensitivity differential phase measurements can provide sufficient explanation for it's use [?].

1.2.3 Dual-Recycled Fabry-Perot Michelson (DRFPMI)

Recycling mirrors are an extension of the FPMI that provide a means of enhancing the optical gain of the instrument through different means by the nature of their placement at the symmetric and anti-symmetric ports.

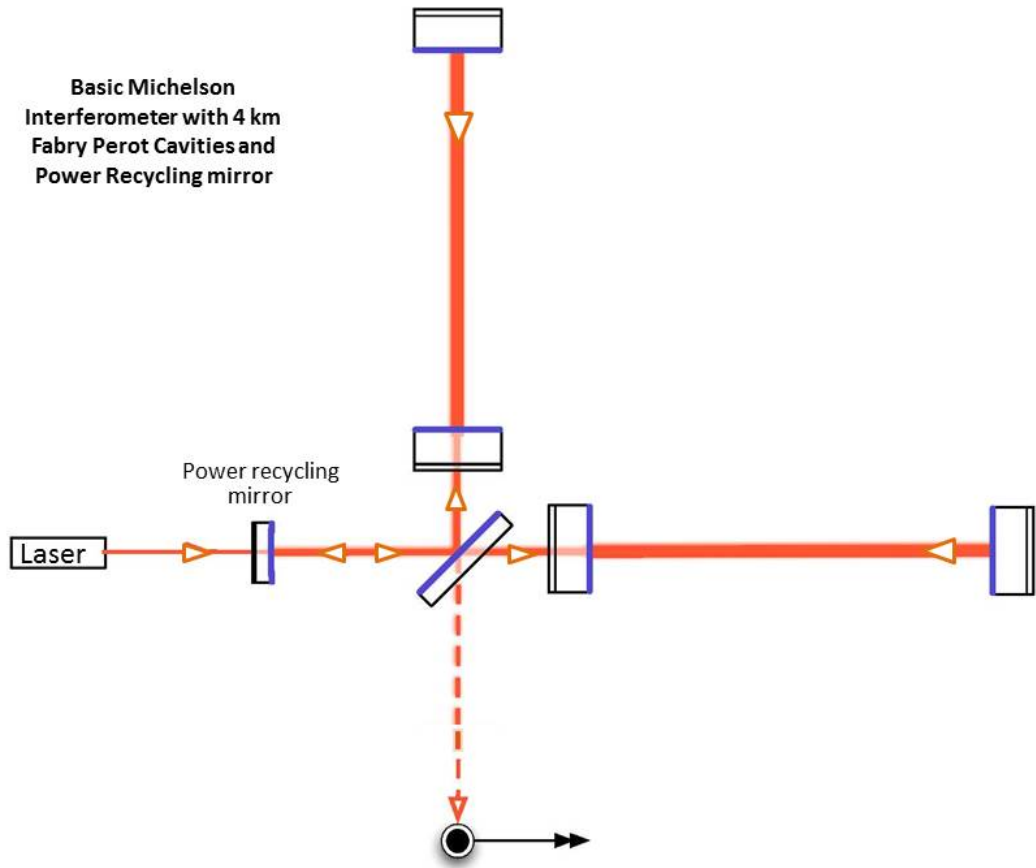


Figure 1.4: PENDING UPDATE (also, borrowed figure does not have SR mirror) The Dual-Recycled Fabry-Perot Michelson optical schema with associated differential arm length response (left is optical schema, right is frequency response)

Power Recycling

When operating a FPMI, power often gets reflected back to the symmetric port leading to a significant waste of power if simply dumped. An additional partially reflective mirror is placed at said port to recirculate (or “recycle”) that power back to the arm cavities. Its positioning is kept fixed enough so that the input light adds coherently with the laser input, while the macroscopic positioning from ITMX/Y is better understood once addressing optical sidebands.

Signal Recycling

This technique is commonly addressed to last because of it's contribution after considering the response from the PRFPMI. The principle can be understood similarly as most of the prior discussions; the use of a Fabry-Perot as an optical amplifier. By simply placing a mirror at the output port it is understood that you would take whatever light leakage coming from the PRFPMI (caused by differential arm motion) and re-introduce it to the arms. Now the question is, can that light add coherently for a signal that you are interested in detecting? As it turns out, it definitely can but careful choices must be made. Mirror location (macroscopic and microscopic tuning) as well as reflectivity have some interesting impacts to the cavity frequency response. But the general statement can be made: when introducing a mirror of relatively low reflectivity at the anti-symmetric port, you increase the detector bandwidth but at the cost of reducing the optical gain.

1.3 ALIGO

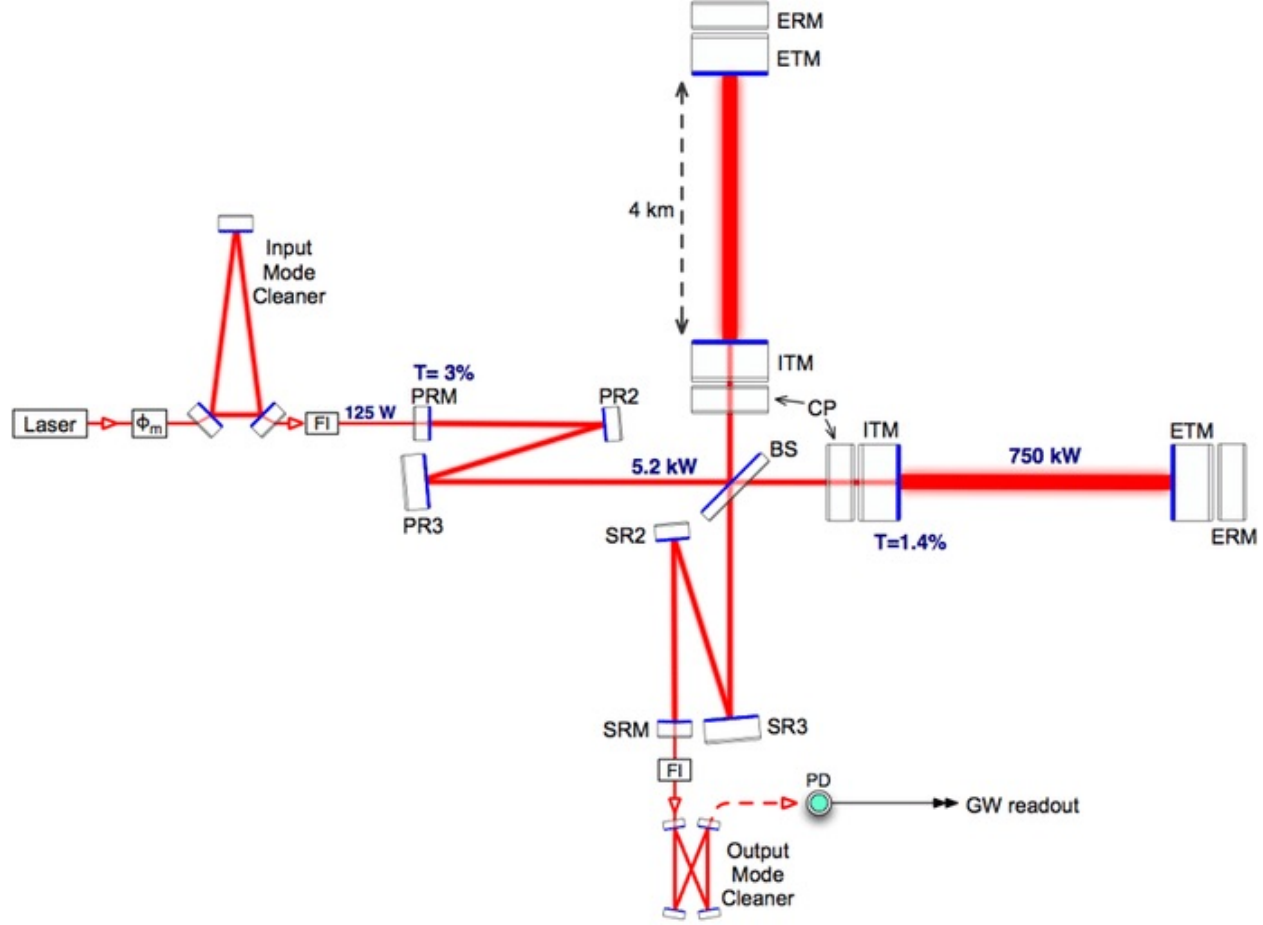


Figure 1.5: DRFPMI configuration used in ALIGO

“Core optics” (Recycling mirrors, Beam splitter, and FP cavity mirrors) are kept suspended with quadruple pendulum suspensions so to decouple seismic activity from the mirror positions.

1.3.1 Reaching “Observing Mode”

The requirements for the operation of the interferometer require that the interferometer be “locked”; meaning that there are some necessary configurations / criteria in order for the instrument to act as an observatory with the designed sensitivity. Cavity length and align-

ment stabilization as well as mode matching are some general requirements for observatory operation.

Length Stabilization

With LIGO’s coupled cavity configuration, maintaining mirror positions is imperative. Techniques such as the offset lock (using a DC photodiode to measure the transmitted, reflected, or circulating power within a linear and slightly off resonance point) [] and the Pound-Drever-Hall technique (see 3.2.1) are used to maintain cavity length stabilization. Stabilizing cavity lengths to configure the detector into a highly sensitive differential arm sensor is a process that is worthwhile understanding with more ample discussions [4].

Gaussian Beams

So far, we’ve discussed light and phase fronts in such a manner that hasn’t addressed the necessary geometric constraints when using Gaussian laser light. We consider a general complex Gaussian beam mode propagating along the beam axis (z) with wavelength λ .

$$E(r) = E_o \frac{\sqrt{[\lambda z_o]/\pi}}{W(z)} e^{-r^2/W^2(z)} e^{-ikz-ik[r^2/(2R(z))]+i\zeta} \quad (1.6)$$

Where E_o is a complex amplitude, $r = \sqrt{x^2 + y^2}$ defines the transverse beam coordinates, k is the wave number, $W(z)$ is the beam width, $R(z)$ is the beam radius of curvature, and ζ is the Gouy phase.

Derived from the paraxial approximation of the Helmholtz equation, this field is not the only solution for optical cavities. Alternative higher order solutions are commonly present and are expressed in terms of two mathematical bases: the Hermite-Gauss and Laguerre-Gauss modes. These higher order modes are more often than not power parasites when operating Fabry-Pérot cavities as displacement sensors and are a symptom of altered cavity geometry; though by virtue of this they can provide error signals for sensing and actuation schemes. This is what is done with ALIGO and is accomplished with the align-

ment sensing and control (ASC) system and thermal compensation system (TCS) for mode matching actuation.

FIGURE: ALIGO Sensor and Actuation schema?

Alignment sensing and control

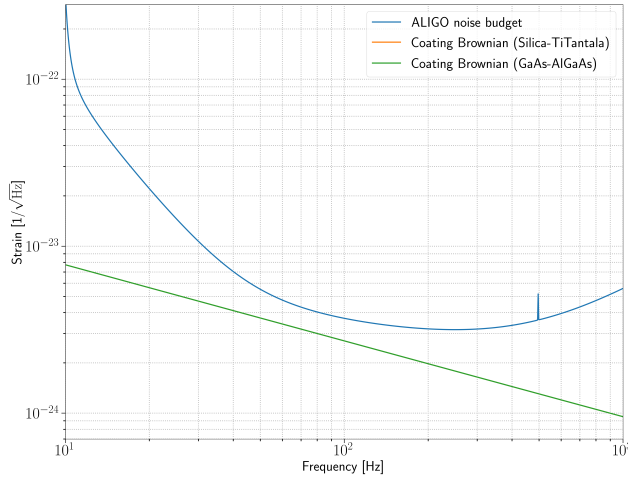


Figure 1.6: A misaligned Fabry-Pérot cavity scatters circulating light into higher order Hermite-Gauss modes.

$$E_{n,m}(x, y, z) = E_o \left[\frac{W_o}{W(z)} \right] H_n \left[\frac{\sqrt{2}x}{W(z)} \right] H_m \left[\frac{\sqrt{2}x}{W(z)} \right] e^{-(x^2+y^2)/W(z)-ikz-ik[(x^2+y^2)/(2R(z))]+i(n+m+1)\zeta(z)} \quad (1.7)$$

Even with state-of-the-art isolation from ground motion for terrestrial gravitational detectors and high mass mirrors, current gravitational wave detectors still suffer limitations and require sensing and feedback loops to maintain mirror alignments.

Mode Matching

For Gaussian beams, there are further requirements of macroscopic mirror positions and radius of curvatures in order to maximize resonant power in the fundamental mode. Failure to plan and maintain these successfully results in a mismatch of the beam mode to the cavity

mode and scattering power into higher order Laguerre-Gauss modes.

$$E_{n,m}(\rho, \phi, z) = E_o \left[\frac{W_o}{W(z)} \right] H_n \left[\frac{\rho}{W(z)} \right]^2 L_m^n \left[\frac{\sqrt{2}\rho^2}{W^2(z)} \right] e^{-\rho^2/W(z)-ikz-ik[\rho^2/(2R(z))]-jn\phi+i(n+2m+1)\zeta(z)} \quad (1.8)$$

Even with ultra-low absorption fused silica substrates and coatings, circulating power is estimated to reach ≥ 200 kW, distorting the radius of curvatures of the arm cavity mirrors by \approx m. In LIGO's coupled cavity configuration, these distortions can introduce significant optical loss due to mode mismatch, and as gravitational wave detector sensitivity approaches the quantum noise threshold, we limit ALIGO sensitivity two-fold with mode mismatch [1]. The solution implemented in ALIGO to mitigate mode mismatch consists of hartmann wave-front sensors with 800 nm and 833 nm probe beams for providing real-time mirror lensing / surface distortion data, and thermal actuation on mirrors throughout the interferometers with particular focus on the arm cavity mirrors. The thermal actuation of the core optics comes in two types: a CO₂ laser actuator impinging upon a pre-installed fused silica compensation plate (CP) for positive lens actuation and an annular ring heater for negative lens actuation [2].

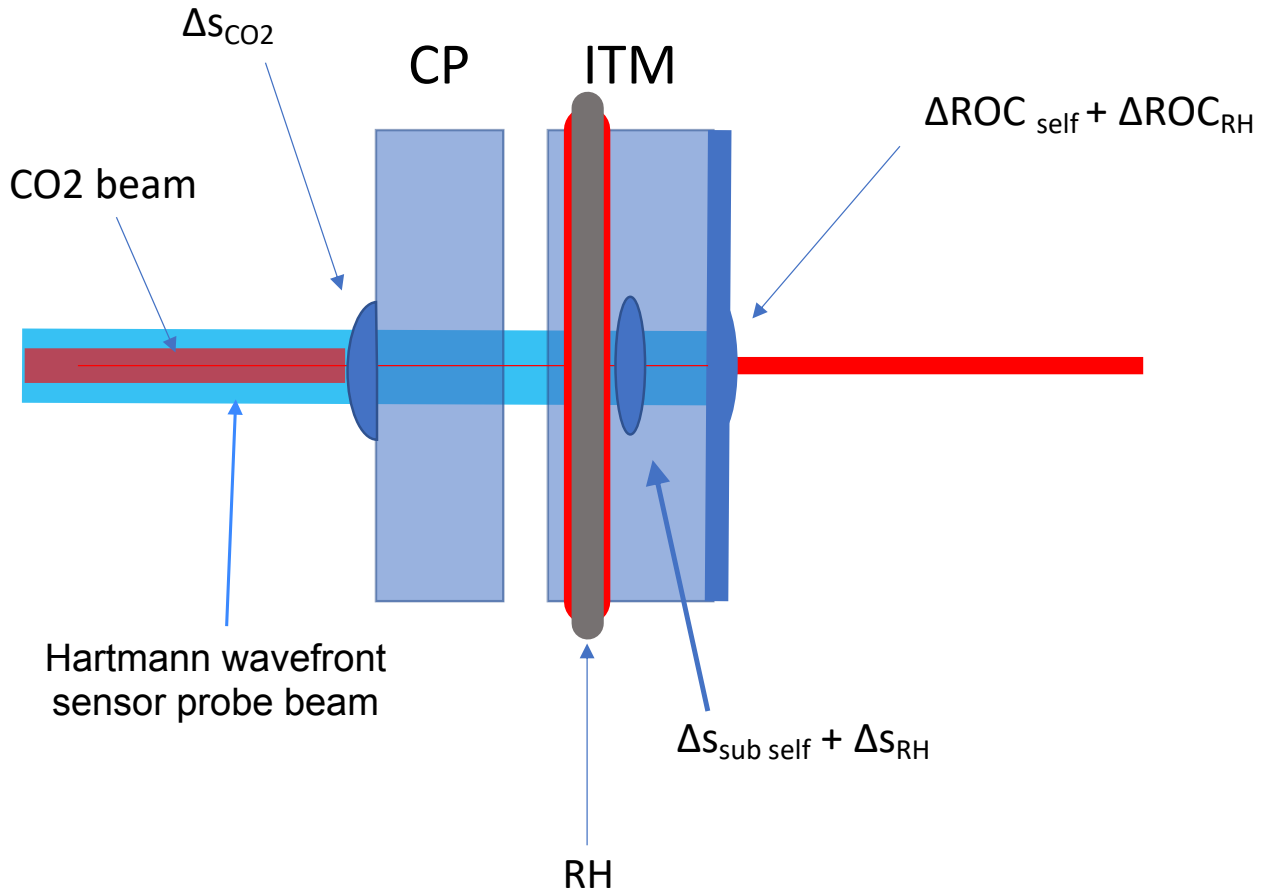


Figure 1.7: Thermal compensation at a single Fabry-Pérot input mirror coupler for ALIGO.

1.4 Coating Thermal Noise

Contributions of categorized noises for gravitational wave detectors are organized in a "noise budget", comprised of a collection of technical (noise imposed by the practical operation of the detector) and fundamental (inherent physical limitations of DRFPMIs by design) noise sources that impose limitations on gravitational wave detection. Contributions of categorized noises for gravitational wave detectors the "noise budget" ((LHO and LLO O3?) or just GWINC?)

1.4.1 Brownian Thermal Noise

Might move this section back to the Al_{0.92}Ga_{0.08}As Electro-optic noise chapter

In 1827 the Scottish botanist Robert Brown noticed a constant motion of pollen particulates on the surface of water; witnessing randomized collisions of the water molecules holding a kinetic energy proportional to the temperature ($k_B T$) [5]. It is because of his documented observations we name the phenomena Brownian motion. And although the observations were on motion of particulates in liquids, molecules and atoms within gases and solids also exhibit Brownian motion. For high precision optical experiments operating at room temperature (and higher due to high power resonant beams), understanding how much differential phase noise is imparted on the interferometer light passing through and reflecting from core optics is crucial. This requires knowledge of the mean squared displacement from each degree of freedom of the system which can be realized through the Fluctuation Dissipation theorem. Derived by H.B. Callen and T.A. Welton, the theorem states that for a randomly fluctuating linear force [6]:

$$F_x^2(f) = 4k_B T \Re[Z] \quad (1.9)$$

Where $\Re[Z]$ is the real part of the impedance of the system. This impedance directly relates to equations of motion:

$$Z = \frac{F}{\dot{x}} \quad (1.10)$$

Another useful form is the power spectrum of the fluctuating motion:

$$x^2(f) = \frac{4k_B T}{(2\pi f)^2} \Re[Y] \quad (1.11)$$

Where Y is the inverse of the impedance or admittance. With this power spectra, modelling and budgeting notable LIGO fundamental noise contributions attributed to the choice

of the materials used for mirror substrates, and highly reflective mirror coatings becomes less daunting. Though adequate modelling of internal force couplings for the aforementioned components is required.

Internal friction in Materials and Loss angle

Zener provides a model of the internal friction of materials incorporating anelasticity into the equations of motion [7]:

$$F = k(1 + i\phi)x + m\ddot{x} \quad (1.12)$$

Where m is mass attached to a spring with a spring constant $k(1 + i\phi)$ incorporating the degree of anelasticity ϕ . From equations 3.5 and 3.3 we perform a Laplace transform and acquire the following form of admittance:

$$Y(s) = \frac{\dot{x}(s)}{F(s)} = \frac{-s}{k(1 + i\phi) + ms^2} \quad (1.13)$$

Or more transparently the Fourier representation since we assume a linear time invariant system:

$$Y(\omega) = \frac{\dot{x}(\omega)}{F(\omega)} = \frac{-i\omega}{k(1 + i\phi) - m\omega^2} = \frac{k\omega\phi - i\omega(k - m\omega^2)}{(k - m\omega^2)^2 + k^2\phi^2} \quad (1.14)$$

Plugging equation 1.14 back into 1.11:

$$x^2(f) = \frac{2k_B T}{\pi} \frac{k\phi}{(k - 4\pi^2 m f^2)^2 + k^2 \phi^2} \quad (1.15)$$

Computing the admittance from a Gaussian beam impinging upon a HR mirror can require expansion of all individual mechanical degrees of freedom of the test mass system across a relevant frequency range, and with that approach convergence is not guaranteed. Saulson and Gonzalez provide an alternative method to computing the admittance coined the “direct

approach” by Levin when computing the noise from a Gaussian beam on a LIGO HR test mass. The admittance can be acquired through:

$$\Re[Y] = \frac{W_{\text{diss}}}{F_o^2} \quad (1.16)$$

W_{diss} is the dissipated power from the system due to an oscillating force F_o . This form of the admittance reveals an important result of the fluctuation dissipation theorem where an undriven system with a dissipative actor, imparts motion to the degrees of freedom via a driving force by virtue of that same actor at finite temperatures. This direct approach also allows the surface pressure applied by the Gaussian beam to interrogate which mechanical modes of the test mass impose a significant energy when 1.16 is plugged into 1.11. In the case of the gaussian beam / uncoated test mass studied by Levin [8]:

$$S_x(f) = \frac{4k_B T}{f} \frac{1 - \sigma^2}{\pi^3 E_o r_o} I \phi \left[1 - O\left(\frac{r_o}{R}\right) \right] \quad (1.17)$$

Refer to Levin appendix for more on how elasticity parameters are introduced? Where ϕ and E_o are the Poisson ratio and Young’s modulus respectively, and $O(\frac{r_o}{R})$ contains a correction term contribution as a function of the small beam radius (r_o) relative to the mirror radius (R).

Coating Brownian thermal noise

Further investigations into the beam/optic system utilizing this approach and elasticity theory led to a deeper understanding about Brownian thermal noise contributions from LIGO test masses (substrate, suspensions, HR coating). Levin mentions, with details from Harry, that the noise contributed by a lossy mirror coating is proven to be the most significant contributor of brownian thermal noise. Hong provides a power spectral density [9]:

$$S_j^X = \frac{4k_B T \lambda \phi_x^j (1 - \sigma_j - 2\sigma_j^2)}{3\pi^2 f Y_j (1 - \sigma_j)^2 \omega_o^2} \quad (1.18)$$

Where X represents bulk and shear with $j = \text{odd}$ (material 1) and $j = \text{even}$ (material 2) alternating layers representing high and low index materials $j = \text{odd}$ (material 1) $j = \text{even}$ (material 2) for an HR coating.

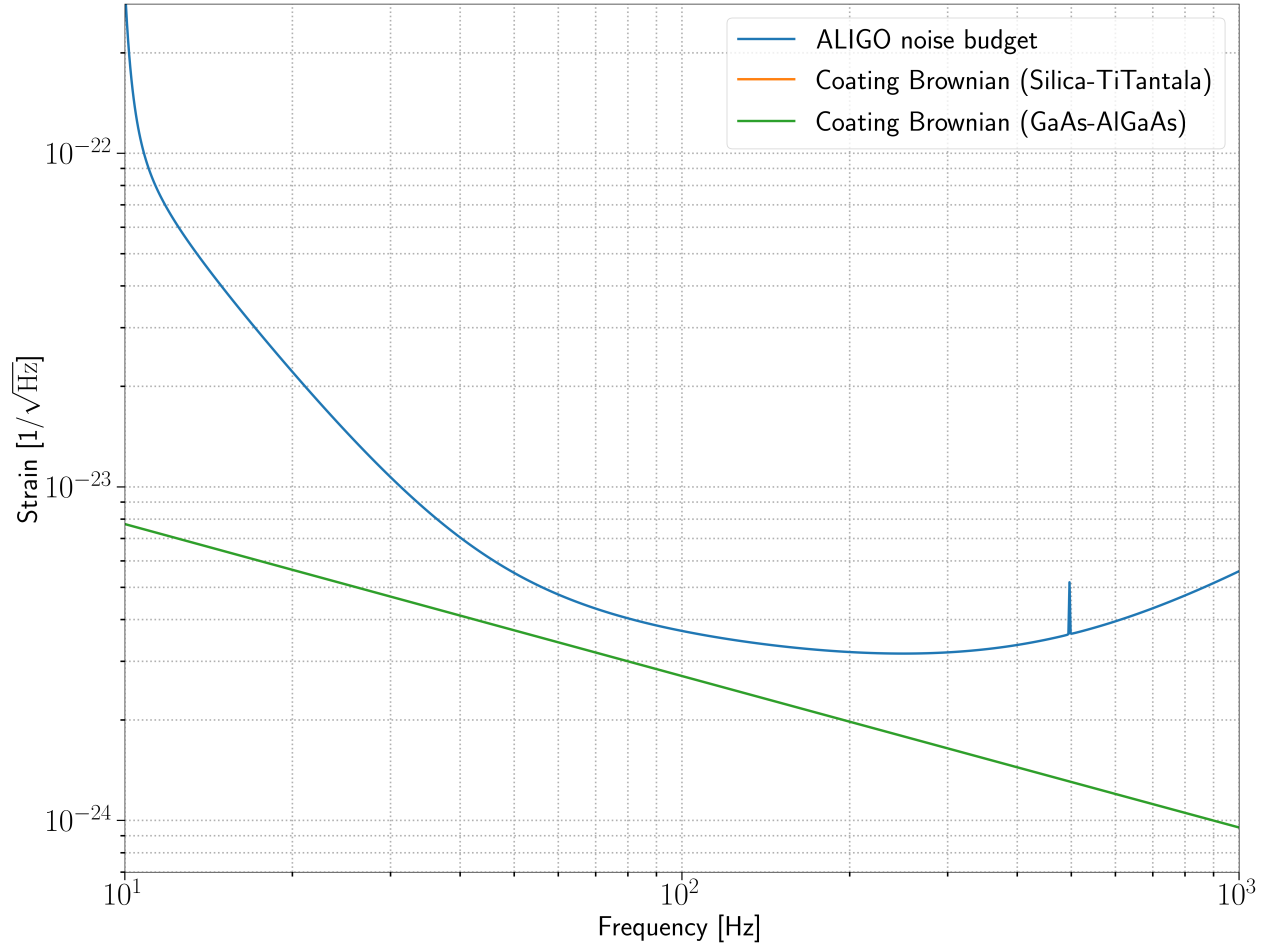


Figure 1.8: ALIGO noise budget placeholder for silica-tantala, and gaas-algaas brownian noise comparison

SiO₂/TiO₂ : Ta₂O₅ coating parameters

Currently the LIGO interferometers deposit $\lambda/4$ stacks of silica and titania doped tantalum on fused silica test mass substrates. Effective loss angle measurements [10]

Current SiO₂/TiO₂ : Ta₂O₅ elasticity params, power spectra, and strain spectral density (order of magnitude estimate)

GaAs/Al_{0.92}Ga_{0.08}As coating parameters

Specific coating parameters for most promising Al_{0.92}Ga_{0.08}As candidates? Chat with Steve.

Or just mention parameters that are listed in Cole 2013 [11]

Insert computed curves of the most precise and recent (effective) loss angle measurements (Nick Demos measurements?). More instructive to plot strain spectral density or displacement power spectra

Currently thermal noise from the SiO₂/TiO₂ : Ta₂O₅ optical coatings is the largest contributor of Brownian noise in LIGO compared to estimated substrate and suspension thermal noise [10]. As of the end of O3, Brownian thermal noise is estimated to be ? orders of magnitude below the current sensitivity and it will prove to be the limiting source of noise as that sensitivity is increased with various other upgrades mitigating fundamental and technical noise. (already mentioned in intro prior to this thermal noise section. Need to re-iterate in more detail?)

Chapter 2

TCS comissioning for O3

During O3a circulating arm power reached beyond 180 kW and the potential optical loss due from thermo-optic effects at arm powers of this level can cause a reduction in sensitivity (by how much exactly?). This motivated the thermal compensation system comissioning detailed in this chapter at the LIGO Hanford observatory which includes: a citation and implementation of the initial O3 TCS pre-load, the installation of a real-time digital filter for increased ring heater actuation by a factor of ≈ 6 allowing dynamic thermal compensation for mode matching actuation and reduction of parametric instabilities, and some studies on the effects of high absorption points aka point absorbers and attempts at mitigating them.

2.1 Pre-loading for O3a

An initial counter to the thermo-optic test mass response from the self heating that occurs at high circulating arm powers is an initial pre-load of the ring heaters and CO₂ lasers. The objective is to maintain the 50 km test mass substrate lens can be roughly preserved while increasing the interferometer input power to the arms. And although estimates of wavefront distortion due to thermal lensing from self heating and ring heater actuation are available and can be computed [12, 13], they can also be directly measured using Hartmann wavefront sensors sensitive to auxiliary beams imaged onto the test mass mirror surfaces. The

measured distortion is then mapped in real time to Zernike polynomials with coefficients used to compute the differential thermal lens in diopters.

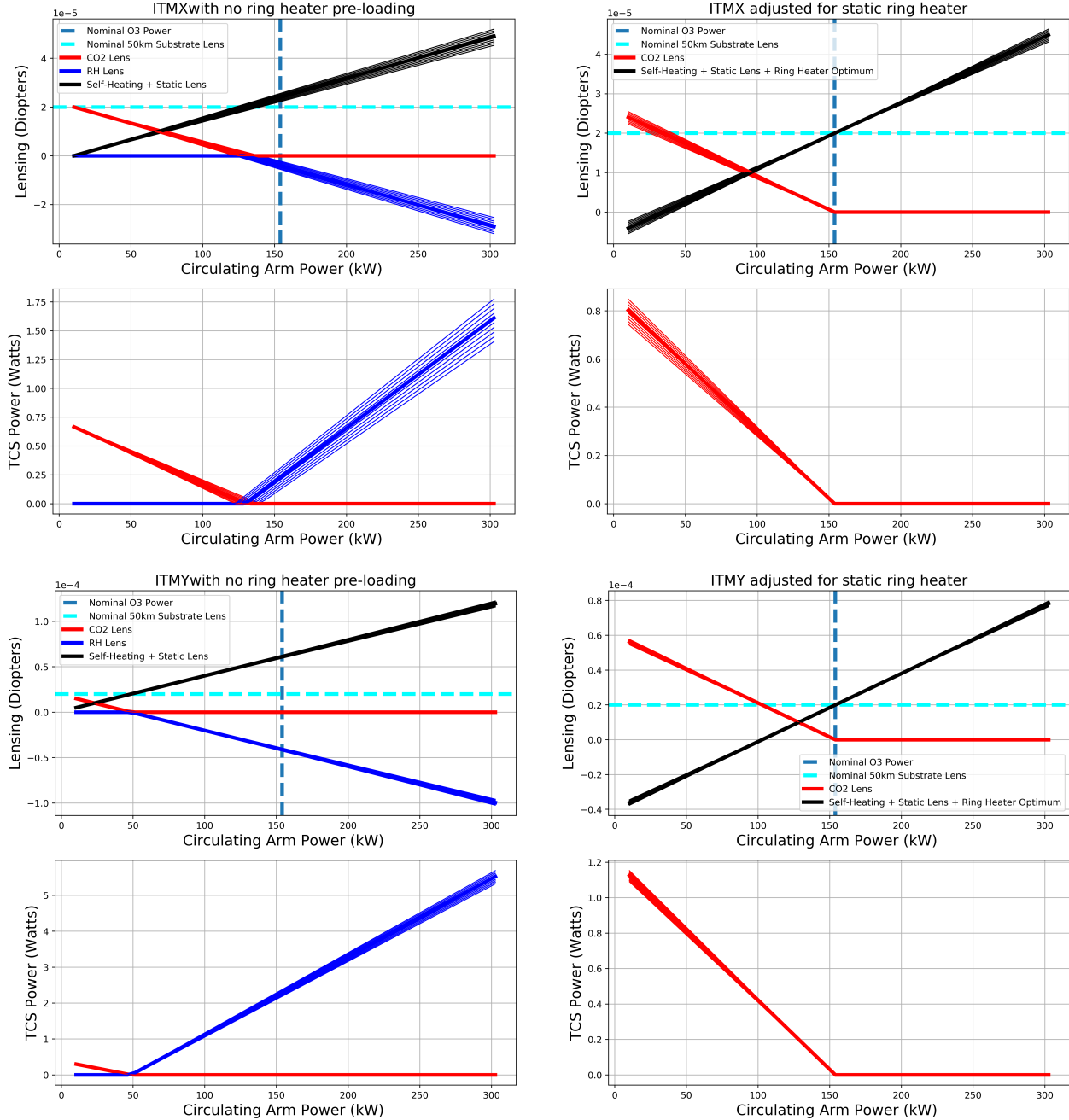


Figure 2.1: The initial pre-load estimates for the ITMs at the LIGO Hanford Observatory for O3a as provided in [14]

2.2 Optimizing RH thermo-optic response

An analytical model of transient ring heater actuation from a radially symmetric thermal aberration ($\Psi(t, r)$) is realized [12]:

$$\Psi(t, r) = 2 \frac{dn}{dT} \sum_{m,p=1}^{\infty} A_{m,p} c_p^u \sin(u_m h/2a) (a/u_m) [1 - e^{-\alpha t}] J_0(\zeta_p r/a) \quad (2.1)$$

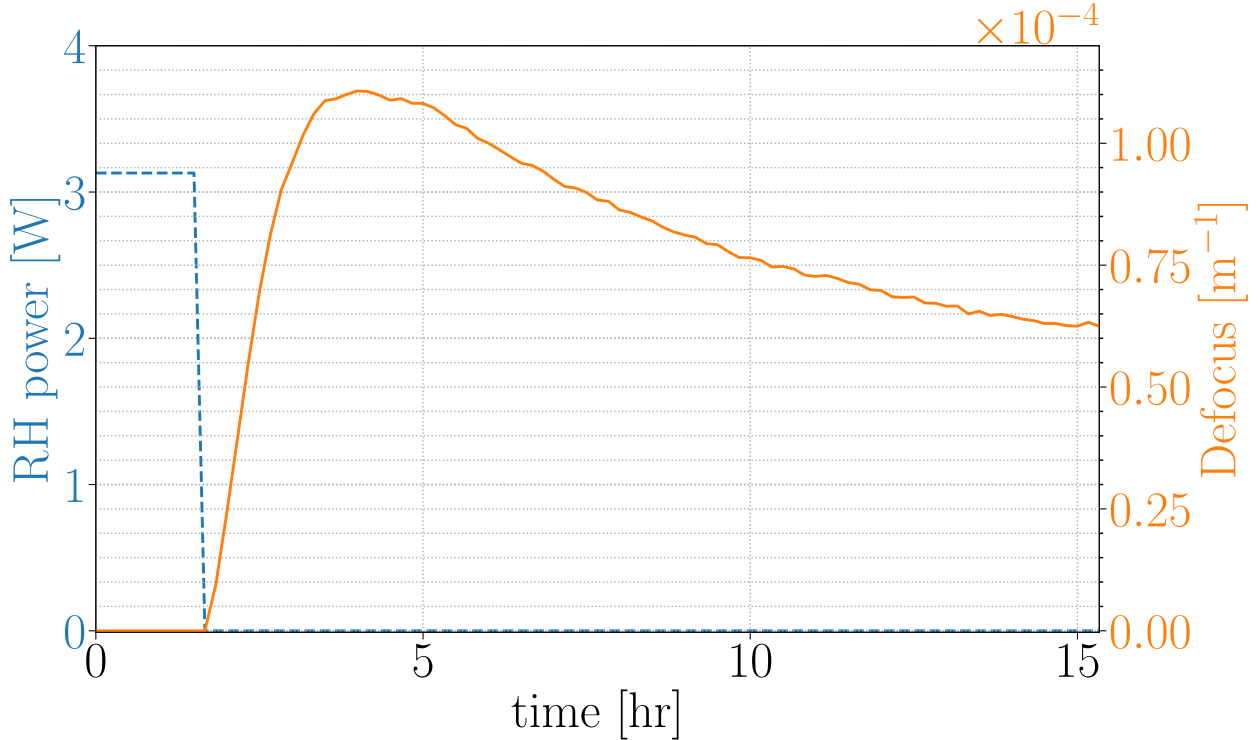


Figure 2.2: ITMY thermo-optic response to a 3.13 Watt power reduction to the top and bottom ring heater elements. It's after ≈ 12 hours after the change was made do you start to see a small enough $\frac{d\alpha_{sp}}{dt}$ when you can assume a steady thermal lens.

The measured transient response can exhibit a prolonged differential defocus on the time scale of ≈ 12 to 15 hours; which can make ring heater adjustments another layer of complexity to the comissioning process when leaving the the detector with unideal mode matching conditions for an extended period. Reduced actuation times are possible with the construction and implementation of a real time digital filtering applied to the ring heater

input power step.

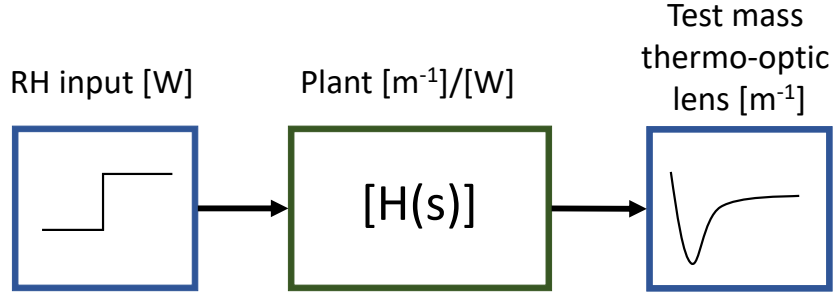


Figure 2.3: A pictograph showing how the plant transforms the signal. The example of this can be seen in Fig [2.2]

The construction of the filter is realized with the following prescription:

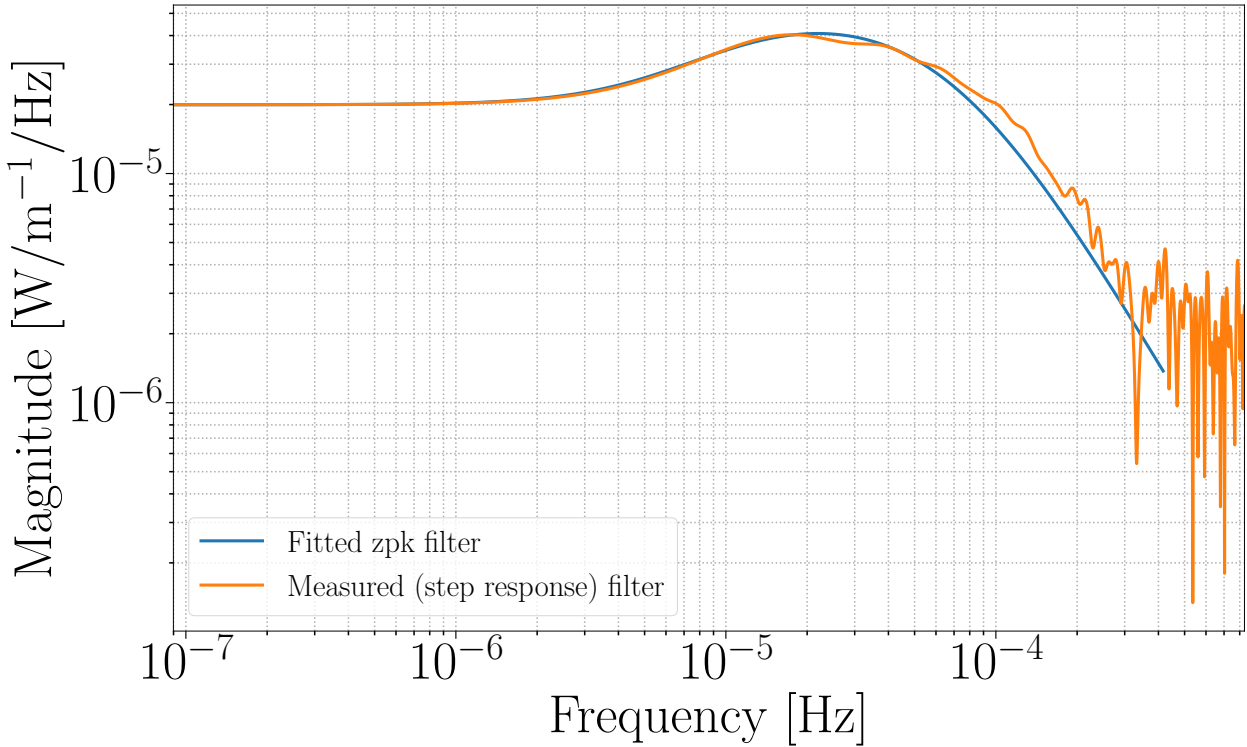


Figure 2.4: Showing the PSD of the RH response (normalized by the input RH power) over a an ≈ 12.5 hour period. The zpk model of the fitted filter ($H(s)$) is $9.2545e - 12 \frac{(s+3.14210e-5)}{(s+8.168e-5)(s+0.0003142)(s+0.0005969)}$

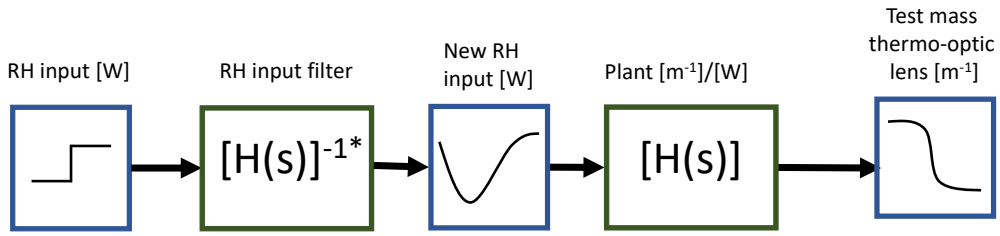


Figure 2.5: A pictograph showing the system with real time digital filtering for an improved thermo-optic response. The RH input filter is created by inverting the plant filter combine with a low pass and added poles to the zpk model to ensure stability.

2.2.1 Dynamic Thermal compensation

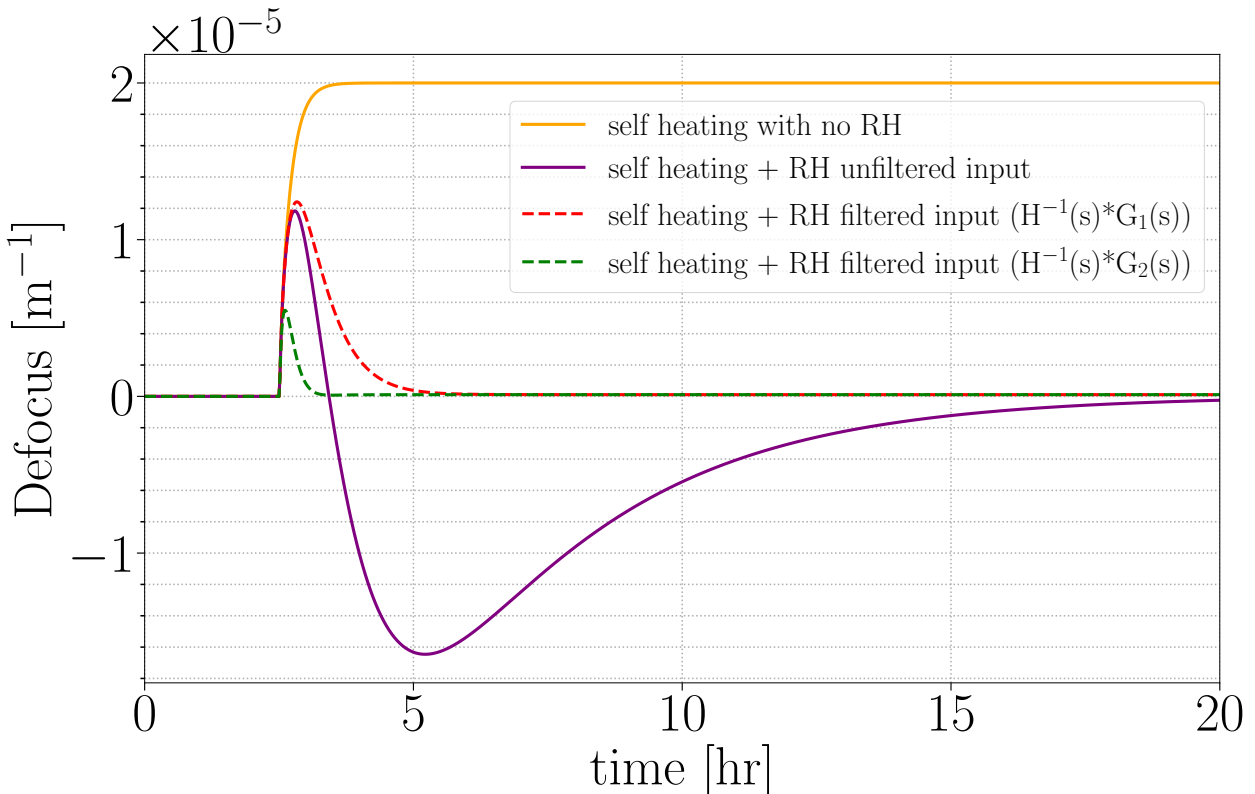


Figure 2.6: Comparison of the natural RH response and the response to the conditioned input. The above plot is simulated in Matlab by passing the RH input time series (top plot) through the $[H(s)]^{-1*}$ and $H(s)$ to acquire with the result lensing behavior on the bottom plot.

Limitations

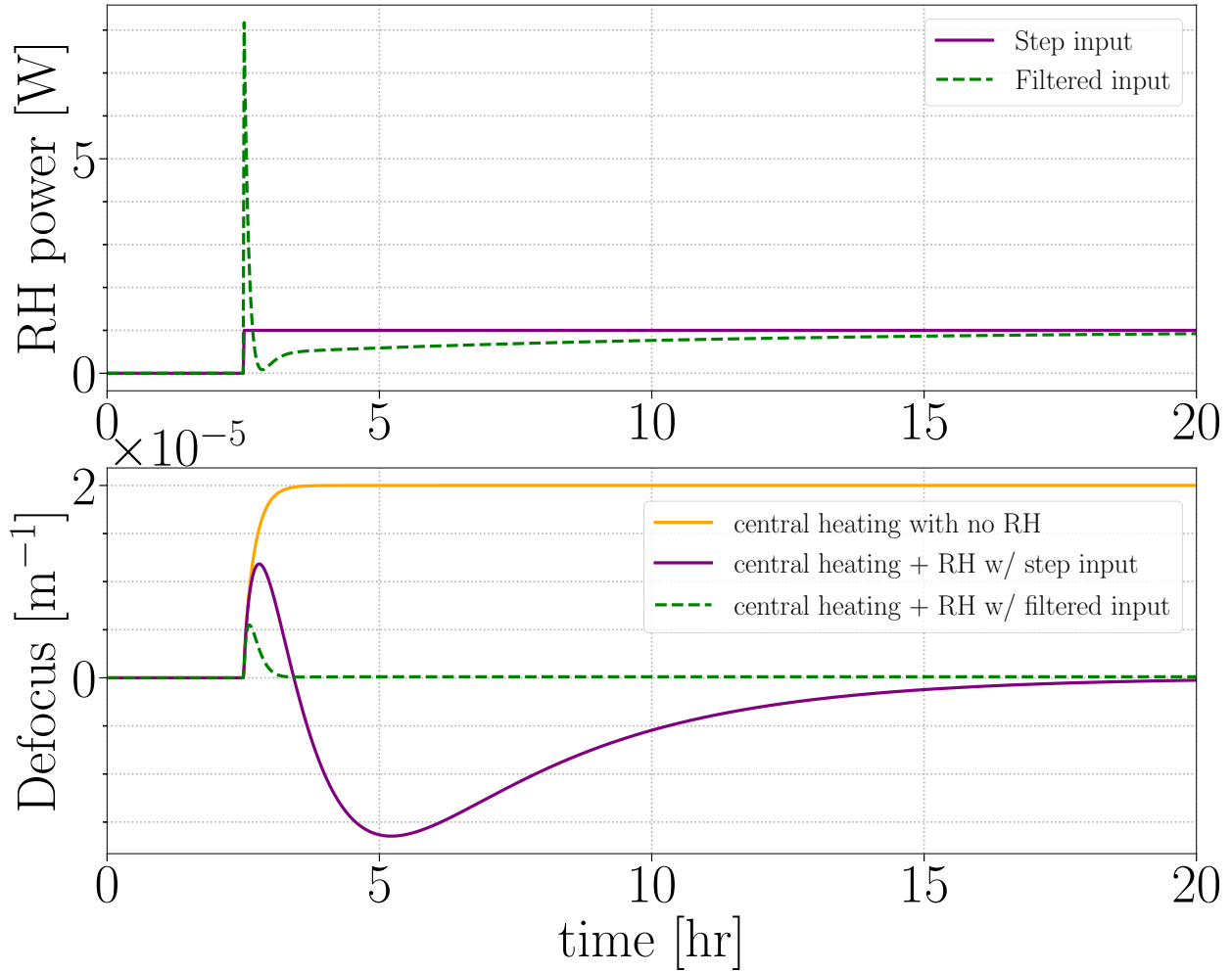


Figure 2.7: Comparison of the natural RH response and the response to the filtered input with RH power

Limitation on RH power is set at 8W **Double check source?**

Implementation into CDS at LHO (appendix?)

2.3 Point absorbers in O3a

- Impact on RF sidebands with interferometer thermalization

2.3.1 Studies

2.3.2 Actuation using a CO₂ laser and mask

- Aiden's design
- Imaging
- Installation
- Metric of improvement? (Impact on sidebands after thermalization) (Tracking dither line amplitudes)

Chapter 3

Electro-optic study of a GaAs/Al_{0.92}Ga_{0.08}As coated mirror

As mentioned in Section one of the many LIGO fundamental noise sources is coating thermal noise from the SiO₂/TiO₂ : Ta₂O₅ aLIGO coatings. As aLIGO approaches its designed sensitivity various coating solutions are currently proposed to mitigate thermal noise coupling into the detector output [?]. With the potential to reduce coating Brownian noise by a factor of 10, GaAs/Al_{0.92}Ga_{0.08}As shows much promise with next generation detectors for a potential strain reduction by a factor of 5 [11], in comparison to the current aLIGO coatings. Though inherent material property differences of these crystalline coatings introduce new and potentially significant noise couplings; one being the linear electro-optic property of crystalline materials (dn/dE), also known as the Pockels effect [15]. Prior to commitment of a GaAs/Al_{0.92}Ga_{0.08}As coating in gravitational wave detectors, a thorough study of these notable noises is worthwhile. This section details a study of starting with a survey of the distinguishing optical and material properties of crystalline materials like GaAs and Al_{0.92}Ga_{0.08}As by reviewing: light propagation through anisotropic materials, and induced optical anisotropy of zincblende materials. Immediately after, estimates of the differential phase of light reflected from a GaAs/Al_{0.92}Ga_{0.08}As coating caused by electric field noise

are computed with potential impacts to current generation gravitational wave detectors. With adequate motivation, an experiment designed to measure the pockels effect from a HR GaAs/Al_{0.92}Ga_{0.08}As coated “witness” sample was constructed and the design, results are discussed.

3.0.1 Anisotropic media

Unlike with isotropic media, we cannot assume that the index of refraction of anisotropic media is the same for all chosen wave vectors. This is a direct consequence of the birefringence of anisotropic media; characterized by the dielectric, permittivity, and polarization tensors.

The Dielectric tensor

Further elaborating on the nature of a generalized dielectric tensor for any wavevector is required to proceed:

$$D_i = \varepsilon_{ij} E_j \quad (3.1)$$

Where D is the displacement vector and E is the electric field vector and ε is the dielectric tensor. The displacement vector for isotropic media is retrieved when $i = j$ and $\varepsilon_i = \varepsilon$. To further understand the nature of the dielectric tensor we assert Poynting’s theorem providing an energy conservation requirement:

$$\nabla \cdot \vec{S} = \frac{dU}{dt} \quad (3.2)$$

Where $\vec{S} = \vec{E} \times \vec{H}$ is the poynting vector and $U = \frac{1}{8\pi}(\vec{E} \cdot \vec{D} + \vec{B} \cdot \vec{H})$ is the electromagnetic field density. The reader is left to perform the exercise and show that in order for 3.2 to hold true given 3.1

$$\varepsilon_{ij} = \varepsilon_{ji} \quad (3.3)$$

Demonstrating that the dielectric tensor is symmetric - exhibiting only six unique terms. Diagonalizing the tensor, the presence of two unique eigenvectors and eigenvalues indicates the existance of two eigenpolarizations with paired eigenindices.

Monochromatic plane wave propogation

Revisiting Maxwell's equations for simple monochromatic plane wave solution gives provides further direction on how crystalline media may effect incident light. Further elaborating, the following assumptions are made:

$$\vec{E} = E_o e^{(i\omega(\frac{n}{c}\vec{r}\cdot\vec{s}-t))} \quad (3.4)$$

Where n is the index of refraction, c is the speed of light, \vec{r} is the position vector and \vec{s} is the unit wave normal.

$$\nabla \times \vec{H} = \frac{\partial \vec{D}}{\partial t} \quad (3.5)$$

Where \vec{H} is the magnetic field assuming the permeability μ , and the generalized displacement vector \vec{D} and electric field vector \vec{E} .

$$\nabla \times \vec{E} = -\mu \vec{H} \quad (3.6)$$

Reducing to only the displacement and electric fields:

$$\vec{D} = \frac{n^2}{\mu} [\vec{E} - \vec{s}(\vec{s} \cdot \vec{E})] \quad (3.7)$$

Maxwell's equations show that the electric field is not necessarily parallel to the displacement field and in most materials with non-zero polarizability tensors and dielectric tensors, it is not. But as specified above, the displacement vector, Electric field and unit wave normal are co-planar while remaining orthogonal to \vec{H} . Assuming we are operating within a coordinate

system aligned with the principal dielectric axes, we substitute 3.1 into 3.7:

$$E_i = \frac{n^2 s_i (\vec{E} \cdot \vec{s})}{n^2 - \mu \varepsilon_i} \quad (3.8)$$

From here it can be shown that for a general plane wave there exist two unique refractive index solutions within the constructed dielectric. Though using this result to show this requires revisiting geometrical conditions that are best visualized using a method introduced in the next section. **For a more rigorous proof, see Appendix H in [16]**

Indicatrix

Acquiring solutions of the two indices along with the corresponding directions of propagation in the crystal for a general plane wave with unit wave vector \vec{s} can be done via a convenient geometrical construction. The construction begins by considering a constant electric energy density (U_e) surface in the \vec{D} space; an ellipsoid is formed:

$$\frac{D_x}{\varepsilon_x} + \frac{D_y}{\varepsilon_y} + \frac{D_z}{\varepsilon_z} = 2U_e \varepsilon_o \quad (3.9)$$

With redefined coordinates $(\vec{D}/\sqrt{2U_e \varepsilon_o}) \rightarrow \vec{r}$ and setting $\varepsilon_i = n_i^2$:

$$\frac{x^2}{n_x^2} + \frac{y^2}{n_y^2} + \frac{z^2}{n_z^2} = 1 \quad (3.10)$$

This equation for the ellipsoid is known as the indicatrix. Given the co-planar solution demonstrated in the last section, we can impose the normal of the plane $\vec{r} \cdot \vec{s} = 0$:

$$\vec{r} \cdot \vec{s} = x s_x + y s_y + z s_z = 0 \quad (3.11)$$

Equations 3.9 and 3.11 both contribute constraints to the method of finding extrema using Lagrange multipliers for the function:

$$r^2 = x^2 + y^2 + z^2 \quad (3.12)$$

The Lagrangian (\mathcal{L}) with the introduced multipliers (λ_1, λ_2) then becomes:

$$\mathcal{L}(\vec{r}, \vec{s}, \lambda_1, \lambda_2) = x^2 + y^2 + z^2 + \lambda_1(xs_x + ys_y + zs_z) + \lambda_2\left(\frac{x^2}{\varepsilon_x} + \frac{y^2}{\varepsilon_y} + \frac{z^2}{\varepsilon_z} - 1\right) \quad (3.13)$$

With the generated system of equations from the Lagrange multiplier method ($\partial F_i / \partial x_i = 0$, and $\partial F_j / \partial \lambda_j$) where index $i = x, y, z$ and $j = 1, 2$ we obtain a system of 3 equations:

$$i\left(1 - \frac{r^2}{\varepsilon_i}\right) + s_i\left(\frac{xs_x}{\varepsilon_x} + \frac{ys_y}{\varepsilon_y} + \frac{zs_z}{\varepsilon_z}\right) = 0 \quad (3.14)$$

The result is verified when substituting $r \rightarrow \frac{\vec{D}}{\sqrt{\vec{E} \cdot \vec{D} \varepsilon_o}}$ back which recovers 3.8.

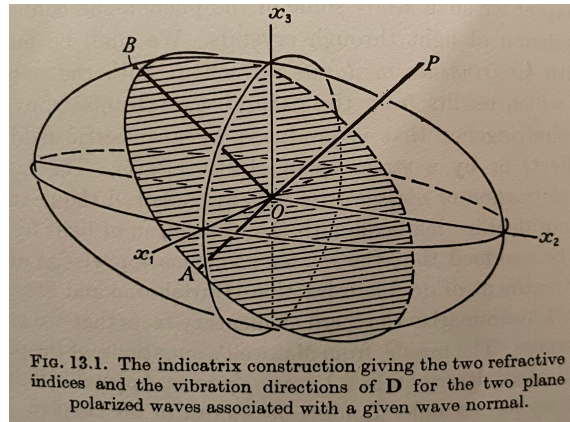


Figure 3.1: General ellipsoid indicatrix with a general propagation direction (Using Nye's figure as placeholder as of now)

3.0.2 GaAs and Al_{0.92}Ga_{0.08}As crystal classification

The space group of GaAs as well as Al_{0.92}Ga_{0.08}As are within the $F\bar{4}3m$ space group. Crystals of this particular space group are commonly known as zincblende crystals; a common crystal configuration named after zinc sulfide (ZnS). Cubic crystals by their crystallographic structure display optically isotropic characteristics when stress free and no DC and/or slowly varying electric fields are present. Is this true? Yes. Though the birefringence seen from HR GaAs coatings is said to be due to an “intrinsic stress” in the high and low index layers. (What is breaking the symmetry to cause this? Heteroepitaxy? Annealing? Defects? Is this birefringence the same for all samples?) I think a dedicated high precision birefringence measurement on multiple samples would be cool.

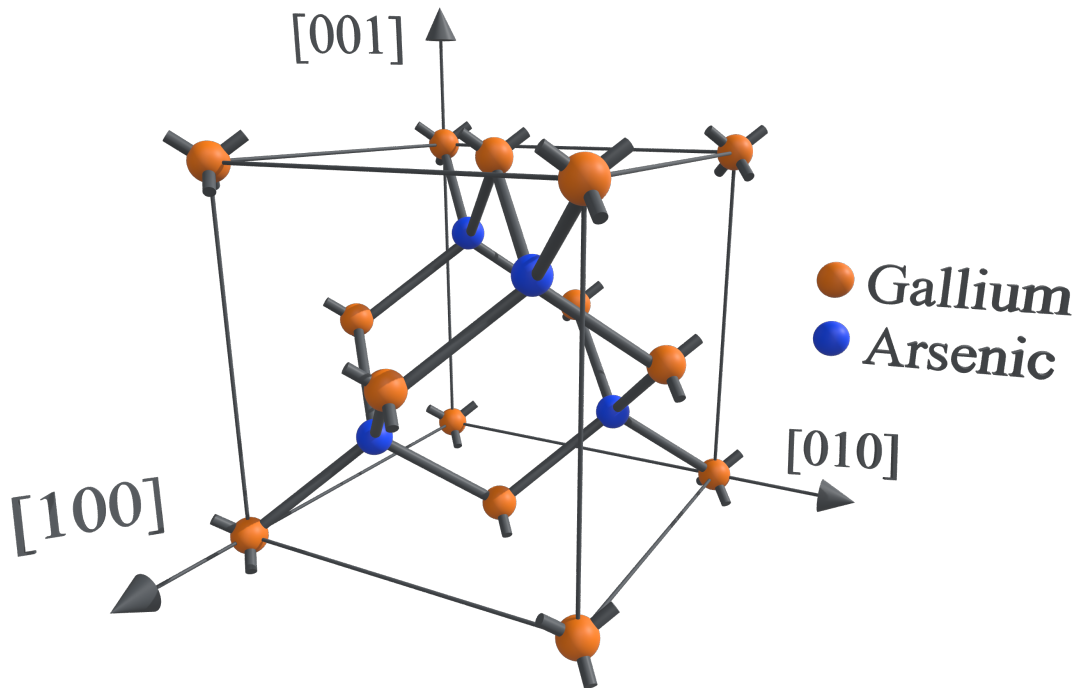


Figure 3.2: The unit cell of gallium arsenide (GaAs) with associated miller indices as coordinate axes

Mention the difference in lattice cell constant between GaAs and Al_{0.92}Ga_{0.08}As?

3.0.3 Induced anisotropy in zincblende crystals

Zincblende structures, like the crystalline materials in question can exhibit birefringent properties when under the influence of two factors: stress in the material, and present within DC electric fields. These two properties of crystalline materials are known as the photoelastic and electro-optic effects respectively.

The (linear) electro-optic (Pockel's) effect

For non-centrosymmetric crystalline media there exists a non-zero rank 2, 6×3 tensor (r_{ij}) connecting a low-frequency¹ electric field $\vec{E}(f) = [E_x(f), E_y(f), E_z(f)]$ directly to the indicatrix [17, 16]:

$$\begin{bmatrix} \left(\frac{1}{\Delta n^2}\right)_1 \\ \left(\frac{1}{\Delta n^2}\right)_2 \\ \left(\frac{1}{\Delta n^2}\right)_3 \\ \left(\frac{1}{\Delta n^2}\right)_4 \\ \left(\frac{1}{\Delta n^2}\right)_5 \\ \left(\frac{1}{\Delta n^2}\right)_6 \end{bmatrix} = \begin{bmatrix} r_{11} & r_{12} & r_{13} \\ r_{21} & r_{22} & r_{23} \\ r_{31} & r_{32} & r_{33} \\ r_{41} & r_{42} & r_{43} \\ r_{51} & r_{52} & r_{53} \\ r_{61} & r_{62} & r_{63} \end{bmatrix} \begin{bmatrix} E_x(f) \\ E_y(f) \\ E_z(f) \end{bmatrix} \quad (3.15)$$

The i index runs over the terms in the indicatrix equation:

$$\left(\frac{1}{\Delta n_x^2}\right)x^2 + \left(\frac{1}{\Delta n_y^2}\right)y^2 + \left(\frac{1}{\Delta n_z^2}\right)z^2 + 2\left(\frac{1}{\Delta n_{xz}}\right)xz + 2\left(\frac{1}{\Delta n_{yz}}\right)yz + 2\left(\frac{1}{\Delta n_{xy}}\right)xy = 1 \quad (3.16)$$

Detail on some prior knowledge of $f \leq f_{\max}$? (Pockels cell specs?)

¹"low frequency" meaning orders of magnitude smaller than an optical field it effects

r_{ij} for zincblende crystals ($r_{\bar{4}3m,ij}$)

The form of the electro-optic tensor for zincblende crystals (including GaAs and Al_{0.92}Ga_{0.08}As) reduces such that $r_{ij} = r_{41} = r_{52} = r_{62} \neq 0$ with all other terms being zero:

$$r_{\bar{4}3m,ij} = \begin{bmatrix} 0 & 0 & 0 \\ 0 & 0 & 0 \\ 0 & 0 & 0 \\ r_{41} & 0 & 0 \\ 0 & r_{52} & 0 \\ 0 & 0 & r_{63} \end{bmatrix} \quad (3.17)$$

Where also $r_{41} = r_{52} = r_{63}$

New principal (electro-optic) dielectric axis for zincblende structures

In general the principle dielectric axes of the new ellipsoid do **not** coincide with the axes of the ellipsoid of the unperturbed crystal. The form of the index ellipsoid for a zincblende crystalline material accounting for the electro-optic tensor and some generalized DC electric field \vec{E} expressed in terms of the crystallographic axes is given by:

$$\left(\frac{1}{n_o^2}\right)x^2 + \left(\frac{1}{n_o^2}\right)y^2 + \left(\frac{1}{n_o^2}\right)z^2 + 2r_{41}E_{[100]}yz + 2r_{41}E_{[010]}xz + 2r_{41}E_{[001]}xy = 1 \quad (3.18)$$

Where we have set $n_x = n_y = n_z = n_o$ for zincblende structures.

The two principal axes are given by the eigenvectors of the the matrix given from the equation above:

$$\begin{bmatrix} \left(\frac{1}{n_o^2}\right) & r_{41}E_{[001]} & r_{41}E_{[010]} \\ r_{41}E_{[001]} & \left(\frac{1}{n_o^2}\right) & E_{[100]} \\ r_{41}E_{[010]} & r_{41}E_{[100]} & \left(\frac{1}{n_o^2}\right) \end{bmatrix} \quad (3.19)$$

The photoelastic effect

When a general strains $S_{kl}(r) = \frac{1}{2} \left[\frac{\partial u_k(r)}{\partial x_i} + \frac{\partial u_i(r)}{\partial x_k} \right]$ are applied to a material, the photoelastic tensor p_{idkl} relates to the indicatrix by the following relation:

$$\left(\frac{1}{\Delta n^2} \right)_{id} = p_{idkl} S_{kl} \quad (3.20)$$

Supplementary comment to the measured birefringence from the mentioned intrinsic strain of the high and low index layers

The generalized indicatrix

$$\left(\frac{1}{\Delta n^2} \right)_{ij} = r_{ij} E_j + p_{ijkl} S_{kl} \quad (3.21)$$

Need to fix these indices

New principal dielectric axes for zincblende structures (zincblende photoelastic tensor, zincblende electro-optic tensor)

3.0.4 Electro-optic modulation

A common application of this effect is phase modulation onto a optical carrier field. Electro-optic modulators or Pockel cells accomplish this by sandwiching two capacitor plates around crystal with a single electrical input port designed to take in a frequency (Ω) within a specified modulation bandwidth. When the field amplitude across the crystal is driven by a voltage controlled oscillation, we experience a change in the electro-optic tensor. The voltage amplitude of the signal input is proportional to the strength of the phase modulation on the optical carrier field of frequency (ω) and is commonly quantified in terms of a modulation index (β).

Consider specific crystal that gives us our $\beta \sin(\Omega t)$

$$E_{\text{inp}} = E_o e^{i\omega t + \beta \sin(\Omega t)} \quad (3.22)$$

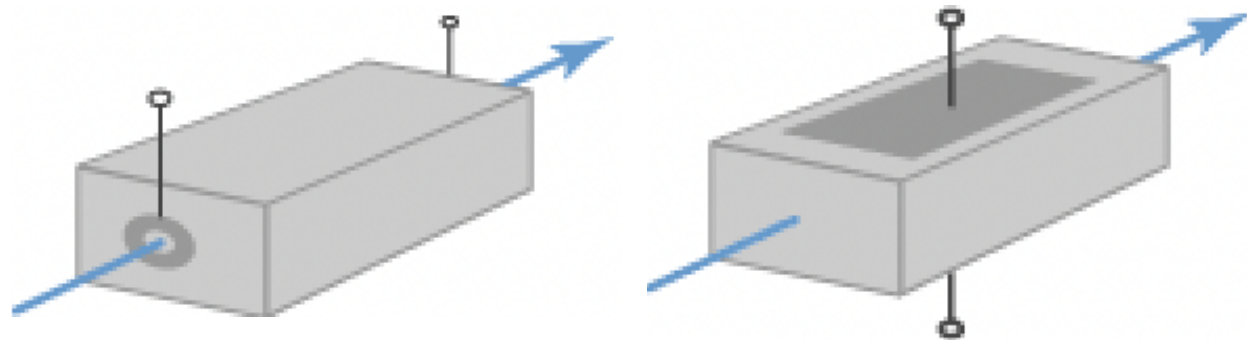


Figure 3.3: PENDING UPDATES currently borrowed image from rp photonics Longitudinal and Transverse Pockels cells

This construction resembles that of the electrostatic optical mount used to drive a longitudinal electric field

3.0.5 Optical anisotropy of a HR GaAs / Al_{0.92}Ga_{0.08}As stack

Our interests primarily lie with the study of birefringent properties of a candidate highly reflective GaAs/Al_{0.92}Ga_{0.08}As mirrorstack. This section is intended to provide a comprehensive review by: 1) making considerations of crystal coordinates when asserting an optical axis on a highly reflective crystalline stack manufactured by Thorlabs, 2) citing coating parameters and observed intrinsic birefringence from the highly reflective coating stack in question, 3) analyzing differential linear electro-optic effect on the phase of a reflected beam, and 4) estimating the the differential phase noise in LIGO based on calibrated electric field measurements.

Miller indices for highly reflective coatings GaAs/Al_{0.92}Ga_{0.08}As coatings

Up until this point we have discussed three different coordinate axes: the crystal axis (indicated by Miller index plane normals), the principal dielectric axis (coordinates based in diagonalization of the indicatrix), and an optical axis (when considering a desired (laser) light propagation). We assert the beam axis [?] with linearly p-polarized light.

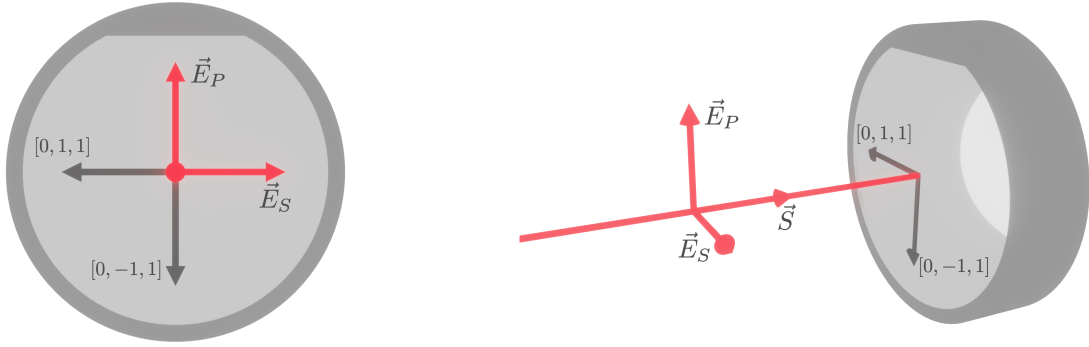


Figure 3.4: The beam propagation axis (\vec{S} , $[−100]$) with respect to the AlGaAs/GaAs crystal axes. The axis formed by the $[100]$ plane normal is parallel with the beam axis (z-axis) and the polarizations of incident and reflected beam oscillate along vectors within the plane formed by the normal of that axis. The AlGaAs coating is grown with a flat indicating a line within the $[0-11]$ plane; where the plane normal points towards the sample center.

Electro-optic coupling to the reflected phase of a HR mirror coating

With our coordinate considerations and established beam axis, it is now worth considering the influence of an isotropic white noise field ($E_n = [E_{nx}, E_{ny}, E_{nz}]$):

$$\begin{bmatrix} \left(\frac{1}{n_o^2}\right) & r_{41}E_{ny} & r_{41}E_{nx} \\ r_{41}E_{ny} & \left(\frac{1}{n_o^2}\right) & r_{41}E_{nz} \\ r_{41}E_{nx} & r_{41}E_{ny} & \left(\frac{1}{n_o^2}\right) \end{bmatrix} \quad (3.23)$$

Assuming E_n is small, the indicatrix change of E_{nx} and E_{ny} relative to E_{nz} (as seen by the beam polarization) will be small ($r_{41}E_{n(x/y)} \ll r_{41}E_{nz}$). After diagonalizing with relevant terms ² in the tensor, we are left with the following eigenindices:

$$\begin{aligned} n'_x &= n_o - r_{41}E_{nz} \\ n'_y &= n_o + r_{41}E_{nz} \end{aligned} \quad (3.24)$$

²Note that the form of the tensor is still in the crystal coordinates but the E_n terms are placed in the tensor such that their directions align with beam axis coordinates.

For GaAs @ 10.6μ $r_{41} = 1.6 \times 10^{-12}$ [m/V]

Adachi estimate for Al_xGa_{1-x}As?

Relevant eigenpolarizations, non-optical field $E_y = E_z = 0$?

Figure: Transformed indicatrix (Before and after E_x)

Figure: Ellipse cross section. New eigenpolarizations and corresponding indices and their influence on incident field (Marty's result)

Assuming we are operating in a coordinate system suggested in Figure 3.4, which plane is impacted by some E_{noise} ? Revisiting the indicatrix we can see that for even non-zero z and y components that the only coupling to the input beam polarization is the index along the cross coupled zy axis through E_z is that of the E_x term. This gives us the ability to easily diagonalize the indicatrix tensor by setting the non-relevant field terms to zero. Fejer and Bonilla take an analytical approximation approach when finding the impact of the electric field to the change in phase of the light through a crystalline anisotropic thin film ($\lambda/4$) stack [18].

$$\hat{\phi}' = \frac{\pi n_1 z}{1 - z^2} (z^{2N} - 1) \frac{z^{2N} \frac{(n_f)^2}{n_2 n_3} (n_2 \kappa_{\gamma 2} + n_3 \kappa_{\gamma 3}) - (n_2 \kappa_{\gamma 3} + n_3 \kappa_{\gamma 2})}{(n_1)^2 - (n_f)^2 z^{4N}} \quad (3.25)$$

$$\text{with } z = \frac{n_2}{n_3} \text{ and } \kappa_{\gamma j} = \frac{d}{d\gamma} \log(n_j h_j) \Big|_{\gamma=\gamma_O} \left(\frac{\hat{n}'_j}{\hat{n}_j} + \frac{\hat{h}'_j}{\hat{h}_j} \right)$$

With κ being a scalar parameter.

FIGURE: Cross sectional view of multilayer coating

Numerical estimate

In the appendix of [19] Ballmer constructs a coating layer transfer function for a given coating layer k with index n_k , and thickness d_k , defining right and left propagating modes

$\Psi^{R,L}$ respectively:

$$\begin{bmatrix} \Psi^R \\ \Psi^L \end{bmatrix}_{k+1} = Q_k D_k \begin{bmatrix} \Psi^R \\ \Psi^L \end{bmatrix} \quad (3.26)$$

D_k applies the phase ($\phi_k = 4\pi n_k d_k / \lambda_0$) from a given coating layer, and Q_k applies the transfer function between high-low/low-high index layers transition:

$$Q_k = \frac{1}{2n_{k+1}} \begin{bmatrix} n_{k+1} + n_k & n_{k+1} - n_k \\ n_{k+1} - n_k & n_{k+1} + n_k \end{bmatrix} \quad (3.27)$$

$$D_k = \begin{bmatrix} e^{-i\phi_k/2} & 0 \\ 0 & e^{i\phi_k/2} \end{bmatrix} \quad (3.28)$$

Defining a HR coating stack, the total transfer matrix from vaccum Q_0 to the N th coating layer is:

$$M = Q_N D_N \dots Q_k D_k \dots Q_1 D_1 Q_0 \quad (3.29)$$

The impact of a differential electric noise field (E) on M due to the electro-optic effect on the k th layer, we use the chain rule:

The coating to be studied consists 36 $\lambda/4$ thick layers of GaAs interspersed with 35 layers of $\lambda/4$ thick Al_{0.92}Ga_{0.08}As. GaAs forms the top and bottom layer to prevent oxygen absorption from the AlGaAs layer. The GaAs layers have an index of $n_{\text{GaAs}} = 3.480$ and a thickness of $\Delta d_{\text{GaAs}} = 76.43$ nm while the low index Al_{0.92}Ga_{0.08}As layers are $n_{\text{Al}_{0.92}\text{Ga}_{0.08}\text{As}} = 2.977$ with thickness $\Delta d_{\text{Al}_{0.92}\text{Ga}_{0.08}\text{As}} = 89.35$ nm. With the cosntructed matrices, we apply these parameters and compute a differential phase of:

3.0.6 Measured birefringence from HR GaAs/Al_{0.92}Ga_{0.08}As mirrors

There seems to be different accounts of a measured birefringence from HR GaAs / Al_{0.92}Ga_{0.08}As (Satoshi, CTN, Aidan)

Is the measured birefringence static? (Layer bonding method might introduce something?)

Does it change from different mounting methods? (Photoelastic) (order of magnitude estimate)

Measurement precision of the coating birefringence? Cavity length, Polarization drifts, etc.

The measured birefringence is estimated to be caused by an intrinsic strain between the epitaxial layers of GaAs/Al_{0.92}Ga_{0.08}As. [11]

Marty's document about Birefringence in Crystalline mirror coatings V.8

3.1 Projected DARM coupling

To estimate how much DARM coupling can occur, we use use a measured field spectra acquired from installed electric field meters located within LIGO Hanford Observatory EX and EY vacuum chambers. Taking the upper and the lower EFM measurements in $.3 \text{ [V/m}/\sqrt{\text{Hz}}]$ @ 60 Hz and $4 \times 10^{-3} \text{ [V/m}/\sqrt{\text{Hz}}]$ @ 4kHz [20]. I don't think these values are calibrated. According to Martynov et al. 2016, the fluctuations in the electric filed is $\sim 10^{-5} \text{ [(V/m)}/\sqrt{\text{Hz}}]$.

This along with computed estimate above allows us to create an upper limit for what this noise might be assuming incoherent fields between the end stations and a flat frequency response within LIGO's bandwidth.

FIGURE: GWINC noise against calibrated electro-optic noise estimate.

3.2 Short, in-air, Pound-Drever-Hall locked, Fabry-Perot cavity experiment

To attempt to acquire a calibrated estimate of the Electro-optic effect, we propose and use a single, in-air cavity, Pound-Drever-Hall servo to maintain resonance with a 1064nm carrier beam; while the GaAs/Al_{0.92}Ga_{0.08}As coated cavity end mirror installed in a custom longitudinal Pockels cell mirror mount. behind this work is the necessity to acquire a calibrated

estimate of the pockels effect from a GaAs/Al_{0.92}Ga_{0.08}As mirror sample from Thorlabs' crystalline mirror coatings. As seen in the prior section, the size of the imparted phase noise for currently existing gravitational wave detector configurations is estimated to be small but notable. Investigation through measurement of said effect requires detection methods with sufficient sensitivity for the differential phase noise imparted by the effect. A Pound-Drever-Hall servo to maintain resonance of a 1064nm carrier field to a Fabry-Perot cavity, with the aforementioned crystalline coated cavity end mirror installed in a custom longitudinal pockels cell mirror mount was tried. Details and specifications of the detection schema are discussed along with relevant measurements and results.

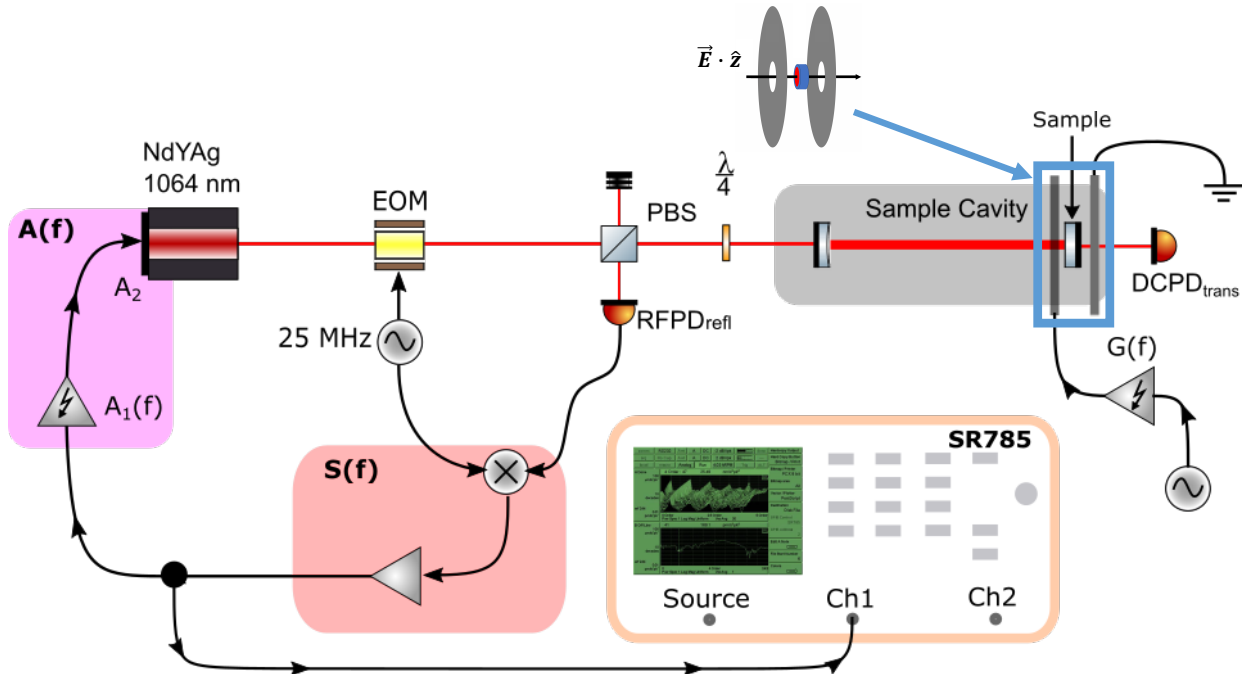


Figure 3.5: A simplified and modular schematic of the PDH servo used along with an electrostatic drive mount design comprised of a disk capacitor sandwiching the HR AlGaAs sample, a high voltage amplifier, and a signal / network analyzer.

Measurability of the electro-optic effect is contingent upon two initial design criteria: the sensitivity of the optical plant to be implemented in the PDH servo, and the maximum achievable electric field strength along the beam axis ($|E_z|_{\max}$).

3.2.1 PDH servo

The Pound-Drever-Hall technique, originally imagined for laser frequency stabilization to an ultra-stable length reference, allows the tracking of the linear phase response of an input carrier field through cavity resonance. The servo fully realizes the ability of an optical cavity to act as a length / frequency discriminator. The alternative cavity offset lock provides a linear response in intensity, which is adequate for some applications but with reduced sensitivity due to the required power reduction by operating off resonance. The phase measurement is achieved through an optical heterodyne; the co-propagation of a separate (but phase-locked) optical field with a known frequency separation to the carrier reflected from the cavity input. To accomplish this, the PDH servo offers a way to avoid complicated phase-locked two laser configurations, by imposing a phase modulation on the carrier field via an electro-optic modulator (aka Pockels cell) mentioned in section 3.0.4. If the modulation depth given by 3.22 is set such that $\beta < 1$ then the input field may be approximated in terms of the first two Bessel functions J_0 , J_1 :

$$E_{\text{inp}} \approx E_0[J_0(\beta)e^{i\omega t} + J_1(\beta)e^{i(\omega+\Omega)t} - J_1(\beta)e^{i(\omega-\Omega)t}] \quad (3.30)$$

With a high enough modulation frequency the terms given above can be far enough from the carrier frequency, so that the phase modulation onto the carrier field is mathematically and physically equivalent to imposing separate optical fields (sidebands) which in most cases do not resonate in the optical cavity of interest. Setting a photodiode of area (A_{PD}) in reflection of the cavity with a coefficient of $r_{\text{cav}}(\omega, L)$, we measure the reflected power of the

input field given by 3.30:

$$\begin{aligned}
 P_{\text{refl}} &\approx \frac{|E_{\text{refl}}|^2}{A_{\text{PD}}} \\
 &\approx \frac{E_0^2}{A_{\text{PD}}} \left\{ J_0^2 |r_{\text{cav}}(\omega, L)|^2 + J_1^2(\beta) |r_{\text{cav}}(\omega + \Omega, L)|^2 - J_1^2(\beta) |r_{\text{cav}}(\omega - \Omega, L)|^2 + \right. \\
 &\quad \left. J_0 J_1(\beta) [r_{\text{cav}}(\omega, L) r_{\text{cav}}^*(\omega + \Omega, L)] - J_0 J_1(\beta) [r_{\text{cav}}(\omega, L) r_{\text{cav}}^*(\omega - \Omega, L)] \right\} \tag{3.31}
 \end{aligned}$$

The two trailing terms in the above equation for P_{refl} generate a beat frequency term between the carrier and lower and upper sidebands. The magnitude and sign of these beat terms directly relate to the phase of the reflected carrier field and can be measured and transformed to the error signal seen in 3.6 using resonant electronics (tuned to a chosen sideband frequency) for amplification and a mixer for demodulation.

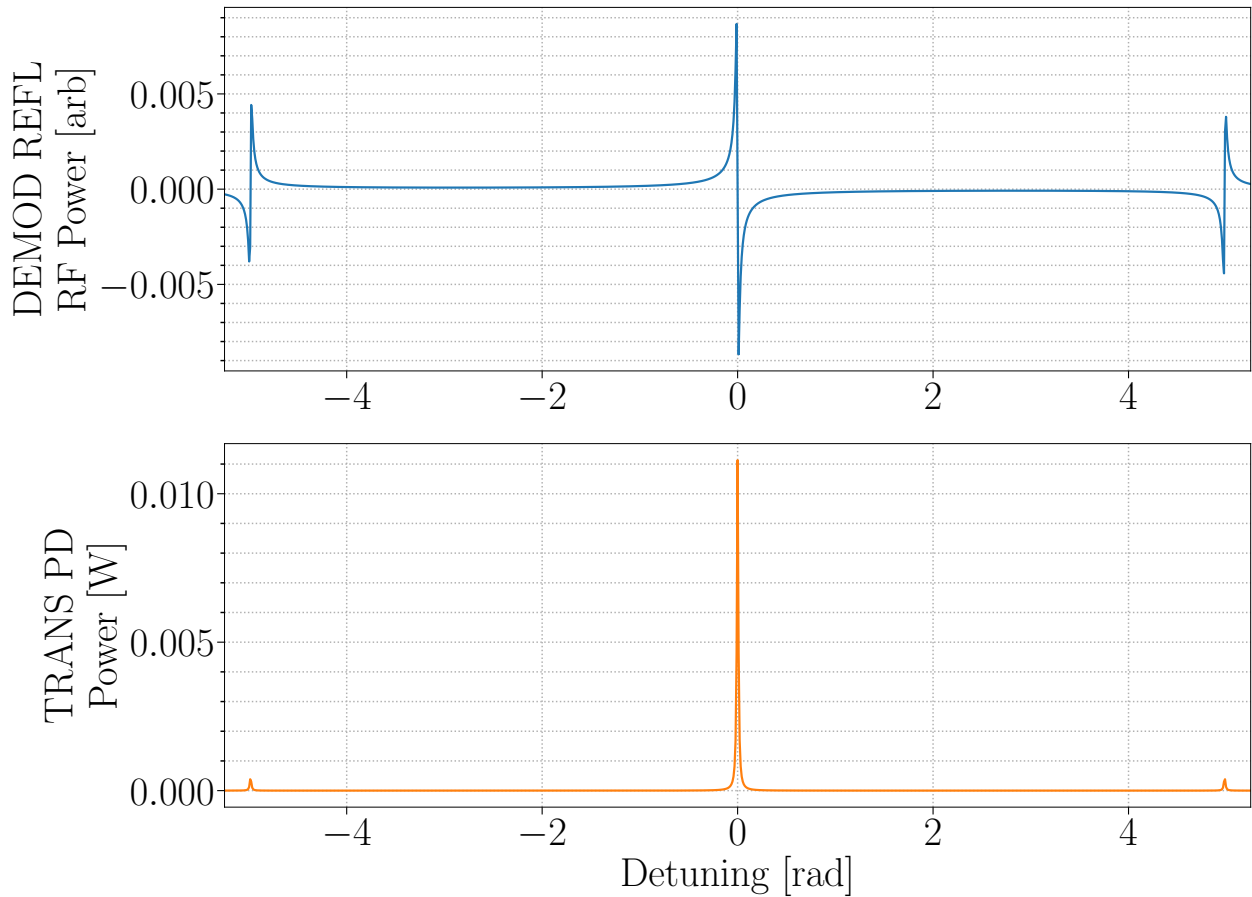


Figure 3.6: By imposing 25 MHz RF sidebands we have introduced a constant reflected reference field near carrier resonance which when beat with the carrier offers a linear response after demodulating the sideband power. With the introduction of high and low frequency sideband fields, their presence is also detected through the DCPDs and PDH error signal. Their separations from carrier resonance are equal in phase (length, and frequency).

With this linearity and sensitivity at cavity resonance, implementation into PID feedback is the next task as any small detuning of the cavity can be registered as a drift from the loop's zero point and fed back to an actuator with an estimated calibration gain factor. When implemented into a low-noise design, this servo can also be used for a high sensitivity lock-in measurement; and with well characterized instrumentation, calibration of the induced differential phase of the light within the stable reference cavity into differential length (or frequency).

3.2.2 Servo Parameters

The quantity we are attempting to measure is on the order of a length change of $\approx \text{m}/(\text{V/m})$, motivating a short cavity design as the relative differential length (phase) change scales with the sensitivity $\Delta f/f = \delta L/L$. Considerations of the lab mirror inventory and mode matching criteria lead us to two candidate plano-concave (ROC = 0.333m) HR IBS coated sample input couplers; one from CVI Melles-Griot and another from ATFilms. When paired with the plano-plano GaAs/Al_{0.92}Ga_{0.08}As mirror from the Crystalline Mirror Solutions (CMS) division of Thorlabs we create a 0.1665 m long cavity.

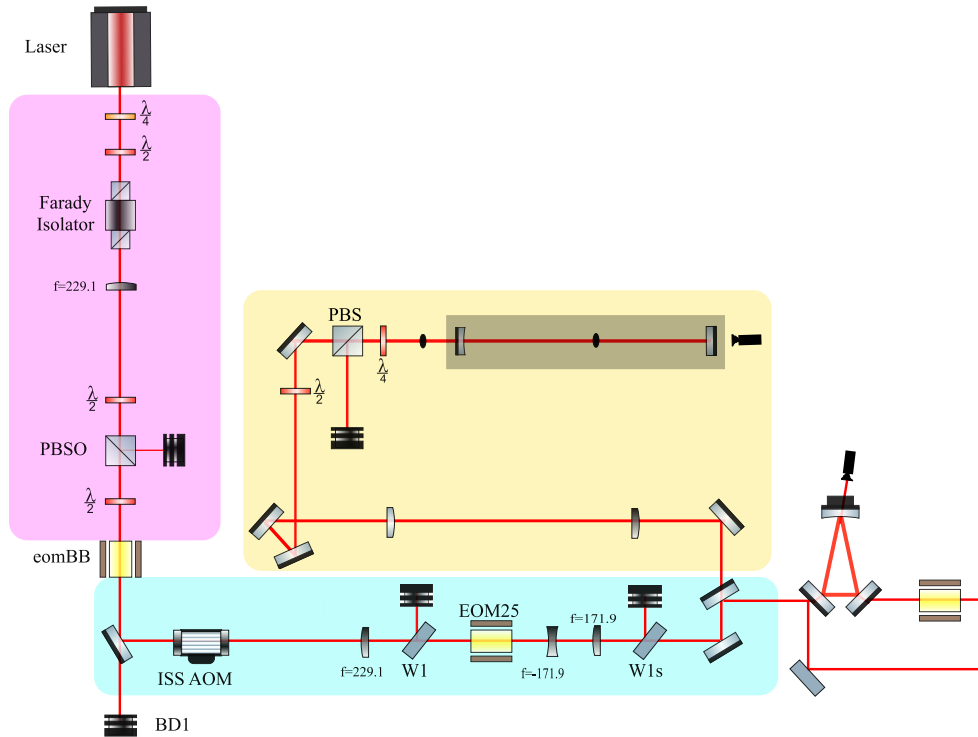


Figure 3.7: **Final figure still pending** Detailed optical schema of the experiment. Components highlighted in magenta indicate laser back-reflection protection and output power control. All optics highlighted in PURPLE indicate their function as alignment and mode matching for locking to a triangular ALIGO PMC **Multiple citations (DCC doc / Fabian's experiment / Erik's experiment)**. Optics highlighted in YELLOW indicate function for alignment and mode matching to the experimental cavity utilizing the HR GaAs/Al_{0.92}Ga_{0.08}As coated mirror sample. Beam profiling to the sample cavity is indicated. For the sake of the numerous mounting strategies tried, the longitudinal pockels cell mirror mount is kept general with the pictured mirror between two disk capacitors

FIGURE: Servo diagram caption: A simplified diagram of the servo used. The highlighted regions of the schematic are intended to provide a modular view; highlighting the components required for the PDH servo to operate.

The implemented servo design uses a light source from a Mephisto 2000 NE Nd:YAG (1064nm) laser with a 25 MHz phase modulation from a New Focus Model 4003 IR resonant phase modulator. As indicated in the figure above, the electronics chain can be decomposed into various filter components: $S(f)$, $A(f)$, and $A_{\text{thermal}}(f)$

Sensing S(f)

The sensing filter electronics are composed of a single element photodiode (from?) with a QE of ? and the response found in appendix ?. The signal is then mixed with a 25 MHz oscillator phased 180 degrees ? m of cable so the measured beat signal while sweeping through resonance generates the PDH error signal profile.

- 25 MHz RFPD
 - Transimpedance measurement (necessary? or should I just use the mixer out PDH to summarize PD/mixer response)
- Frequency Stabilization servo (modified MIT FSS (DCCD980536)) (LTspice model in appendix)

Actuation A(f)

- Mephisto 2220 PZT response (capacitance estimated from HVA drive measurement with and without connection to PZT)
- Channel 3 of SVR 350-3 BIP High Voltage Amplifier from Piezomechanik GmbH with Pomona box (elog 412)
- Figure of frequency response of A(f)

Low frequency servo (Thermal loop)

- Passed signal from FSS → integrators → Laser thermal actuator input

OLG(f)

Isn't quite $A(f) * S(f)$ as stated. Doesn't entirely account for the optical plant. How the measurement is taken (important to take between installations to account for the changes in the optical plant) (elog 831)

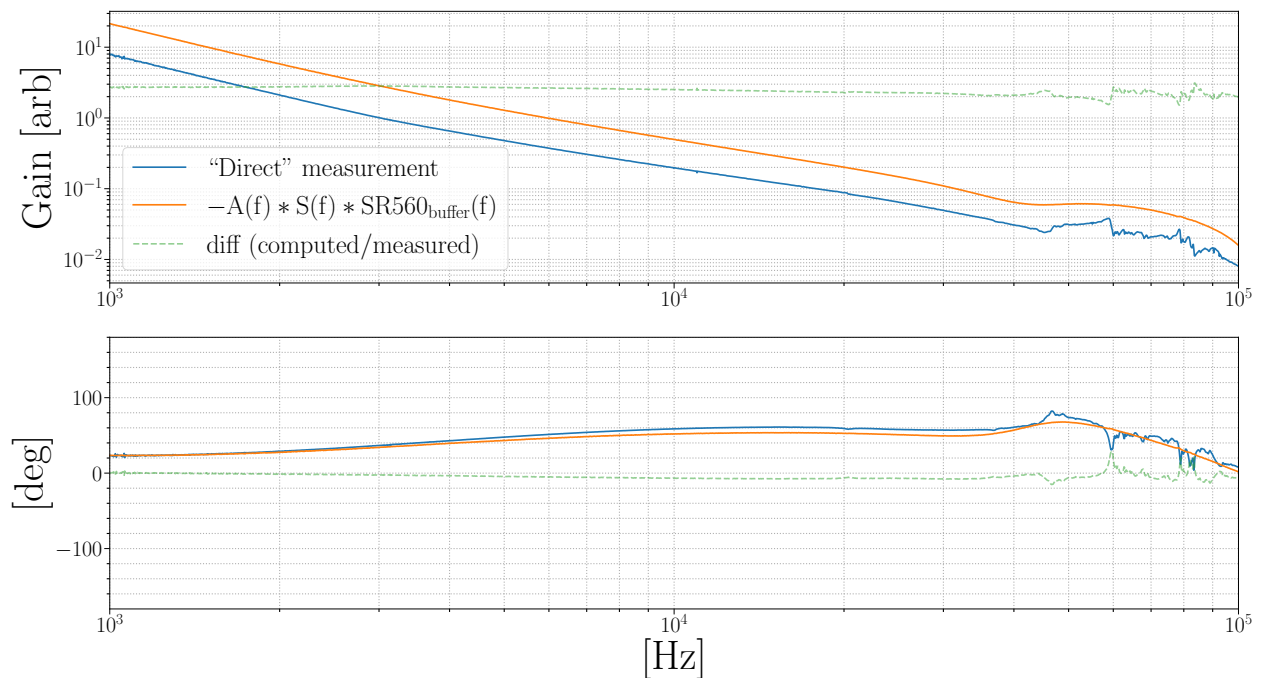


Figure 3.8: Comparison of the open loop gain measurement against the multiplied servo electronics measurements. The maximum gain difference is about a factor of 2.8 which is low passed to a difference of 2.0.

3.2.3 Longitudinal Pockels Cell mirror mount assembly

Maximizing a controlled and well defined electric field ($|E_z|$) within the coating while requiring a through beam to and through the HR coating lead us to a design very similar to that of a longitudinal pockels cell []. The most common assembly in for this study is comprised of

two electrodes with a 3mm central aperture which is chosen to be at least 5 times larger than the beam size at the plate locations; to avoid significant beam clipping while maximizing field strength at the coating region of interest. There is also a required separation of at least 1/4" accounting for the thickness of the optical sample. Considering these constraints, modelling the system and computing the estimated field strength screened by the coating is the next step to the construction of the assembly.

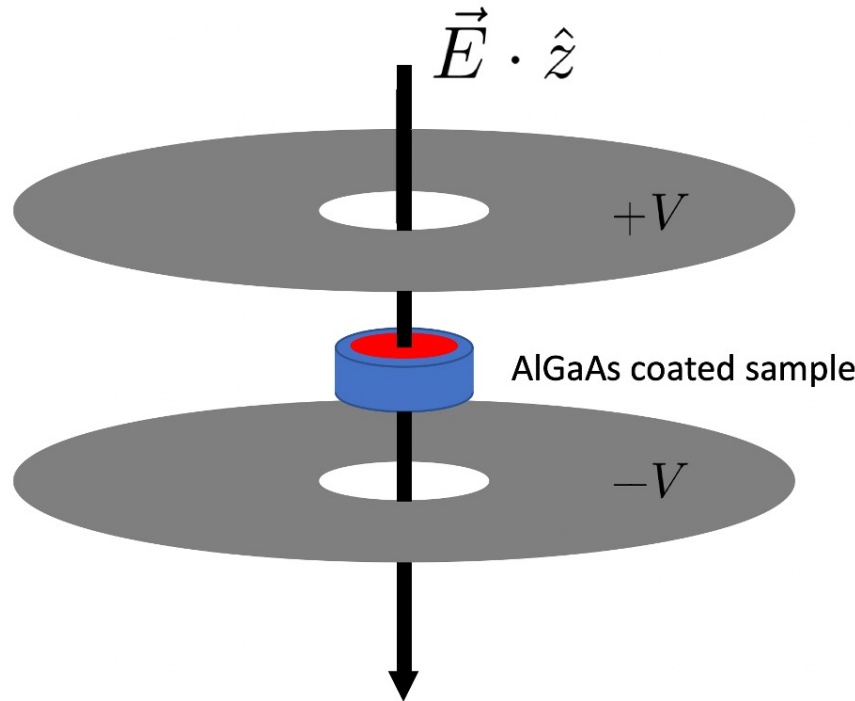


Figure 3.9: Concept image of the longitudinal Pockels cell assembly

Modelling

To find the Electric field screened by the coating we begin with Gauss' Law:

$$\nabla \cdot D = \rho_{\text{free}} \quad (3.32)$$

For our problem we assume no free charge, but the fused silica substrate with the AlGaAs coating presents dielectric material between the plates. Our initial boundary conditions are

also expressed in terms of plate potentials so it is natural to first solve for the potential (V) for every point within our system. We can exploit the cylindrical symmetry with the optic and plate geometry in the r coordinate so we shall express the Laplacian accordingly:

$$(1 - \chi(z)) \left[\frac{1}{r} \frac{\partial}{\partial r} \left(r \frac{\partial}{\partial r} \right) + \frac{\partial^2}{\partial z^2} \right] V = 0 \quad (3.33)$$

Where $\chi(z)$ is the electric susceptibility.

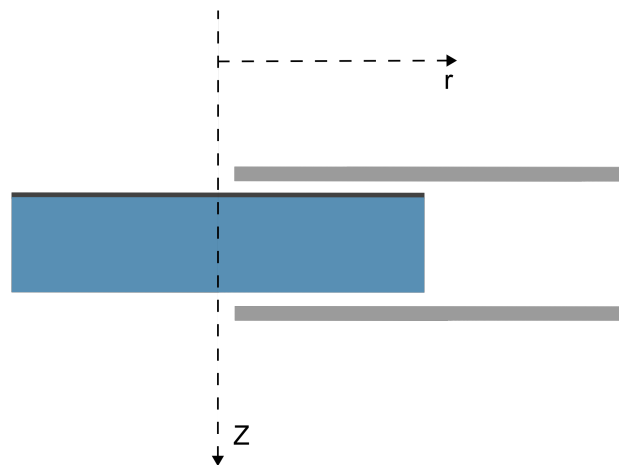


Figure 3.10: Use relevant cross sectional figure to establish coordinates for GaAs/Al_{0.92}Ga_{0.08}As, as well as the fused silica substrate so the computation is transparent. Cross sectional diagram indicating relevant axes and boundary conditions utilized in the numerical computation.

Numerical recipe in appendix

- Potential map computation in cylindrical
- Computing E_z from potential map
 - inside coating
 - outside coating

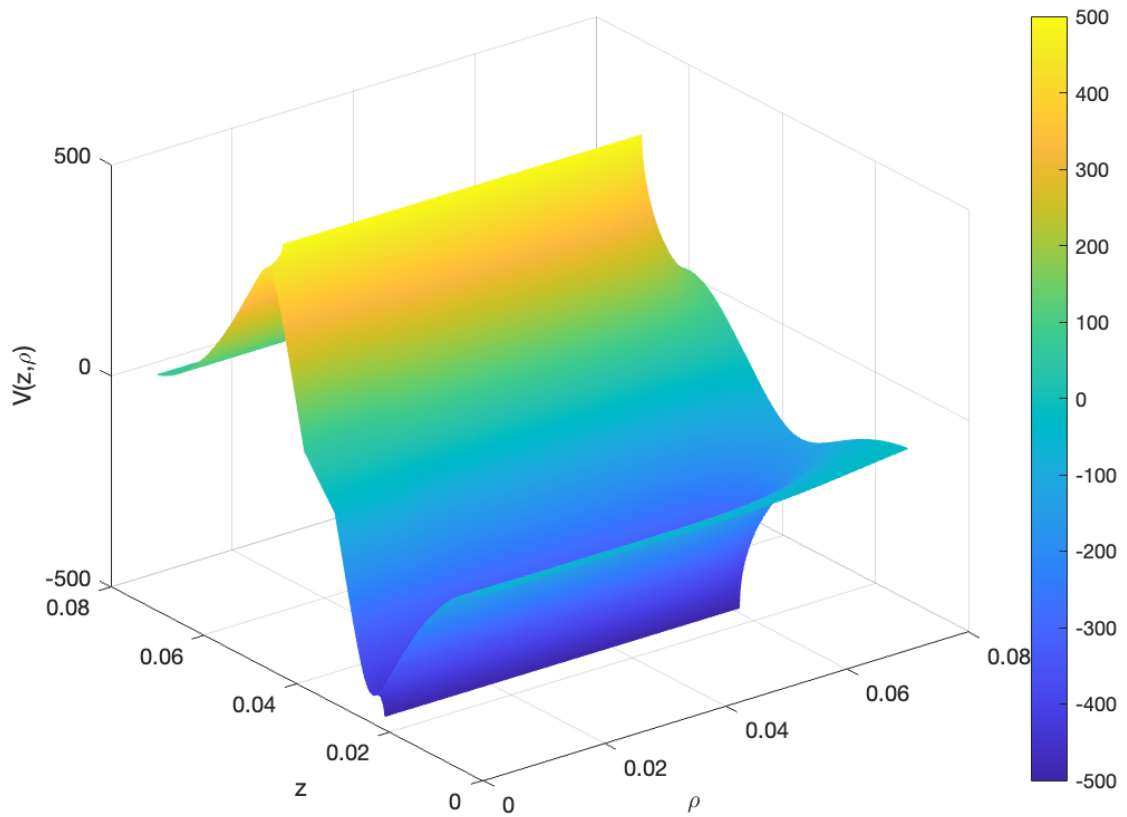


Figure 3.11: Poisson calculator output potential map ($V(z, r)$) in cylindrical coordinates)

Voltage drive electronics

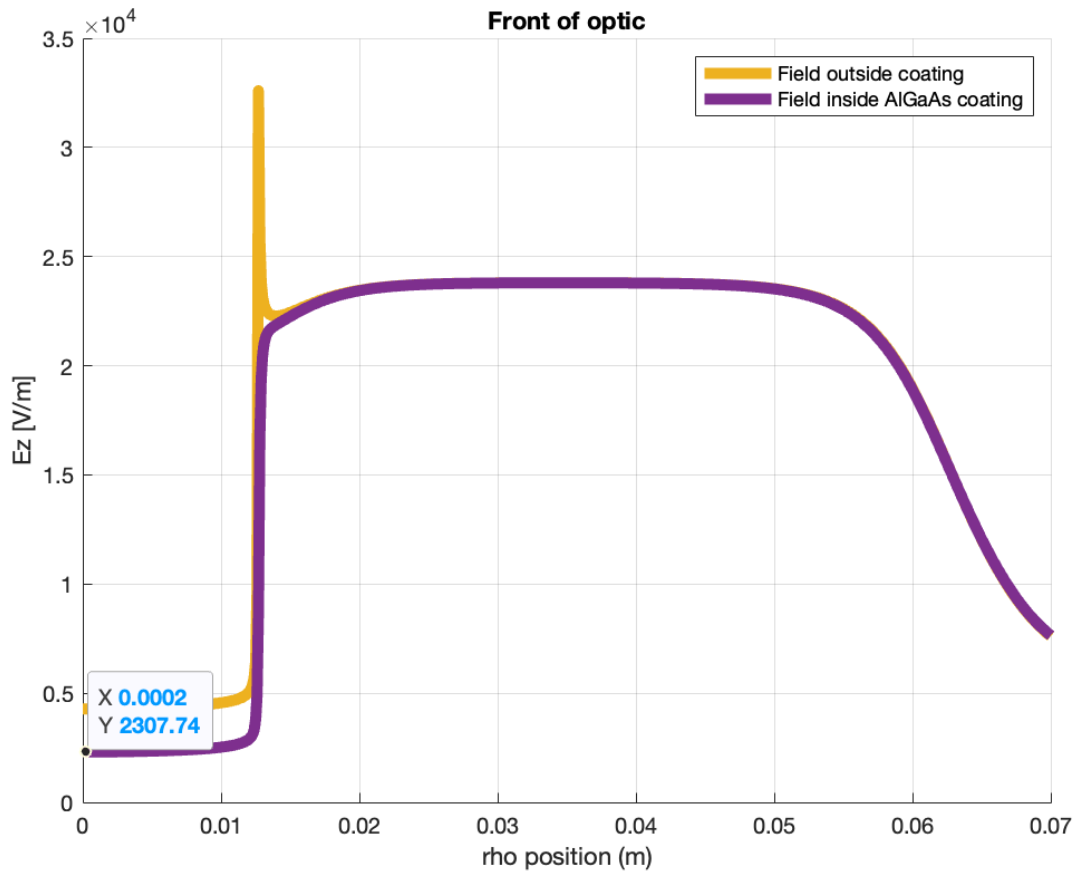


Figure 3.12: The availability of required voltage amplifiers during the course of this study was limited and lead to the use of multiple high voltage amplifiers with all transfer functions listed.

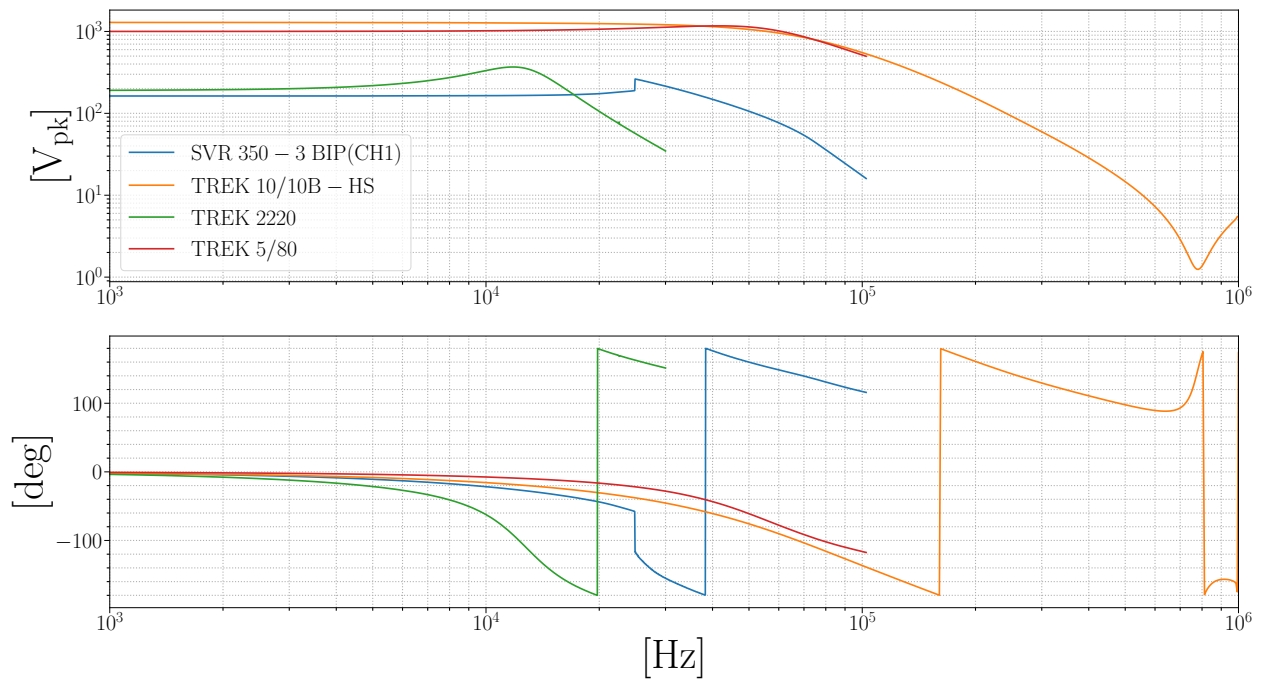


Figure 3.13: Different high voltage amplifier transfer functions used for the study

3.3 Results

A major challenge encountered in the design choice made for this experiment is the differential length noise of the cavity when mounting the optics in accessible non-conductive materials. Most commercial optical mounts are conductors which proved to be a barrier when attempting to find a mounting solution while reducing non-normal field gradients within the coating volume of interest within the sample. For this reason, efforts were focused on developing a suitable mounting solution that would provide the best isolation from any uncontrolled field magnitudes while driving a field normally incident on the surface with enough strength and uniformity across the beam area to extract a measurement of the differential length change from the Pockels effect. The mounts studied span different geometries and different material properties. The varying geometrical assembly differences created distinguishable mount solutions, and it is how this section will be divided. For reassurance, we compare displacement spectra against that of a nearly identical cavity with a flat non-crystalline mirror

coating to perform a null measurement reference; ruling out the Pockels effect and providing information for noise investigations.

3.3.1 Measurement Calibration

The error signal spectra probed at the FSS:

$$VFSSOUT_{rms}/\sqrt{Hz} \rightarrow m_{rms}/\sqrt{Hz} \quad (3.34)$$

With the known frequency response of the servo electronics, we calibrate the measurement into differential length:

$$\Delta L = \text{source} * \alpha(f)A(f) * \frac{1 + OLG(f)}{OLG(f)} * \frac{L_{cav}}{f_{laser}} \quad [m_{pk}/\sqrt{Hz}] \quad (3.35)$$

3.3.2 Mounting Strategies

The following section details measurements performed with various longitudinal pockel cell mounts. Further details (assembly parameters, blueprints, and visual aids) can be found in the appendix.

Assembly 1

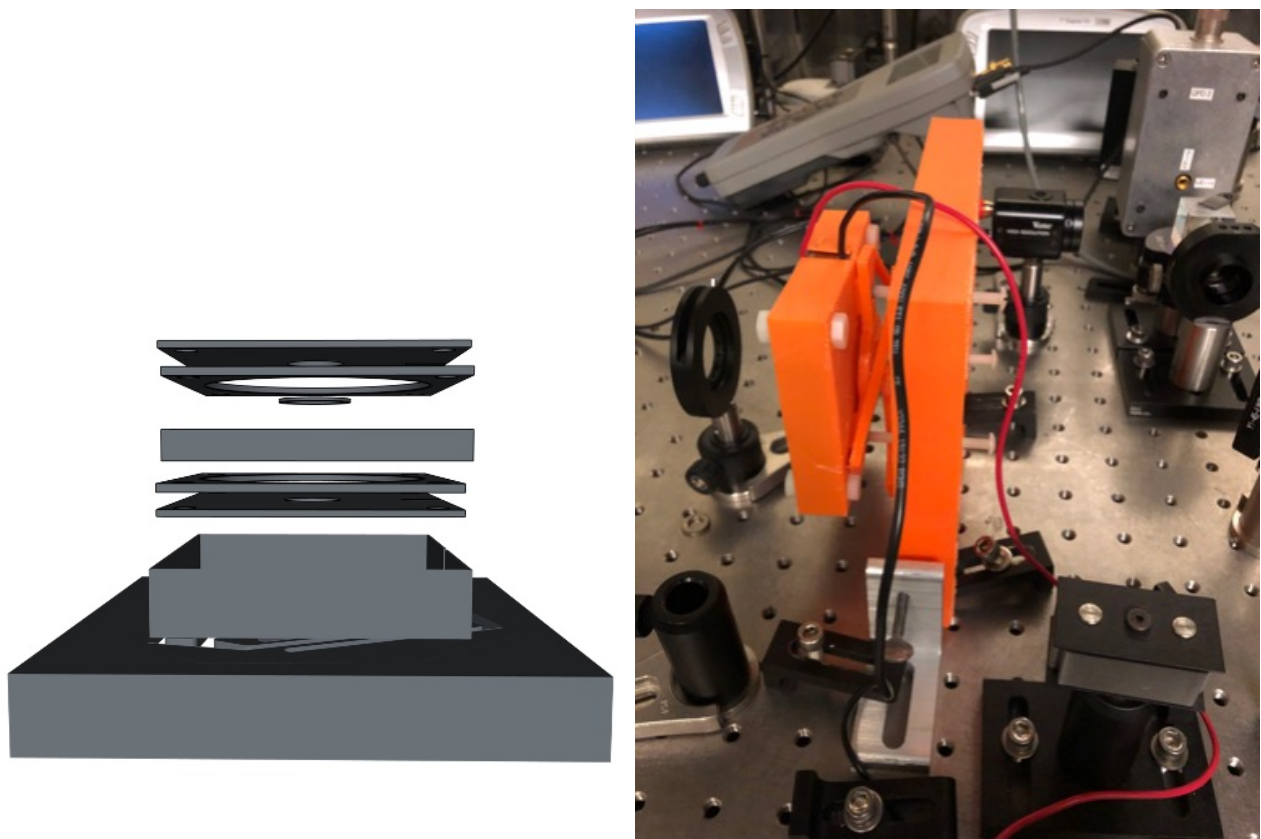


Figure 3.14: Assembly 1 was constructed to meet two criteria: the same solution of housing the sample and electrodes as Assembly 0, but also offer pitch / yaw control via an ortho-planar spring design (Brigham Young University).

The construction revealed flaws; made most obvious when comparing to displacement noise of traditional optical mounts. Pitch and yaw control via the ortho-planar spring were prioritized to avoid metal springs and further mount pieces. The solution became unjustifiable when observing the the displacement noise coupling from the mount.

Re-run this calibration with adequate voltage normalization for a response unit [$m_{pk}/[V/m]$]

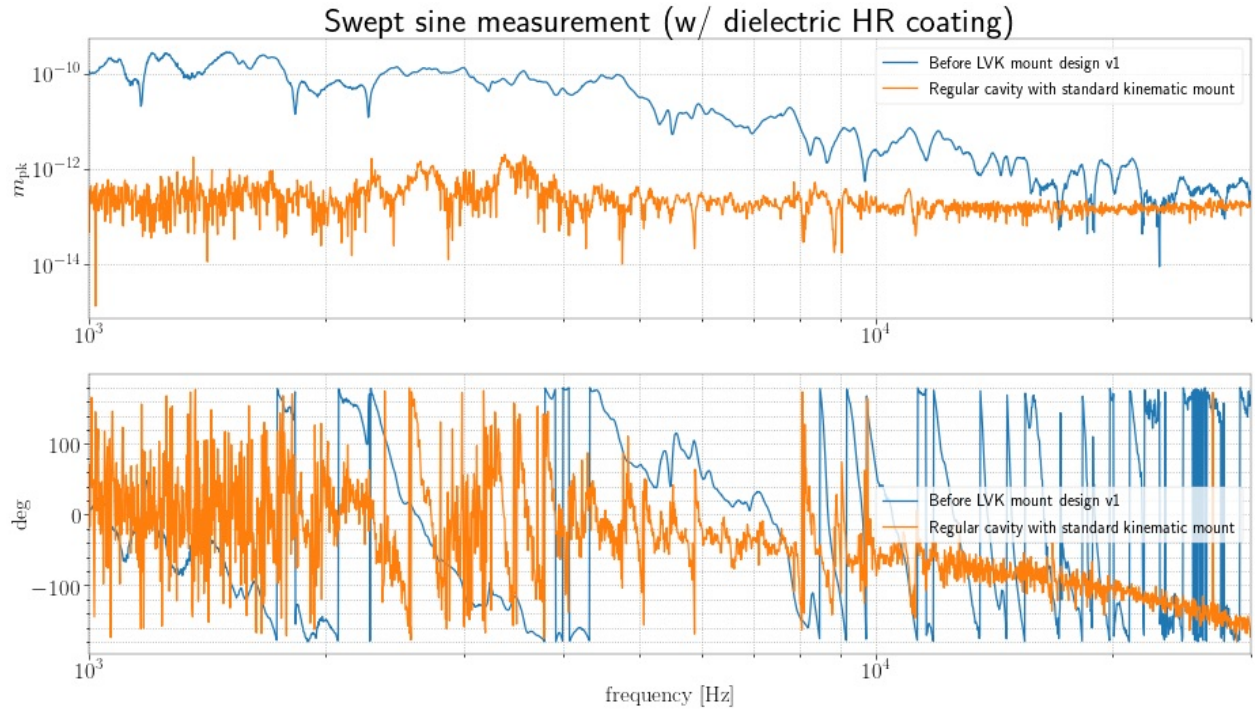


Figure 3.15: Measured displacement spectra for Assembly 1.2 of the longitudinal pockels cell mount compared to the standard kinematic mount. Both measurements were recorded with the the CVI Melles-Griot (amorphous) mirror coating sample installed in the assembly. **Units and legend labels need increase in font size. Remove Swept sine measurement title**

Attempts at improving the pitch dithering were tried with side set screws but mostly caused significant misalignment (less power in fundamental mode, locking issues, etc.). This lead to the final alternative for this assembly type; with the same PLA stack indicated in Assembly 1.

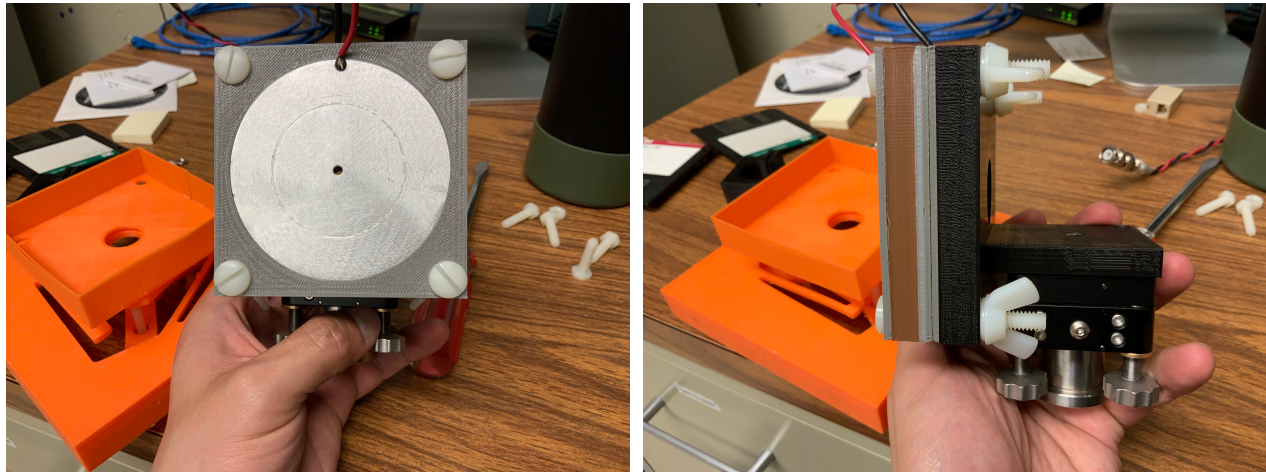


Figure 3.16: A modification implemented with the intention of reducing pitch dithering while still having control of DC YAW

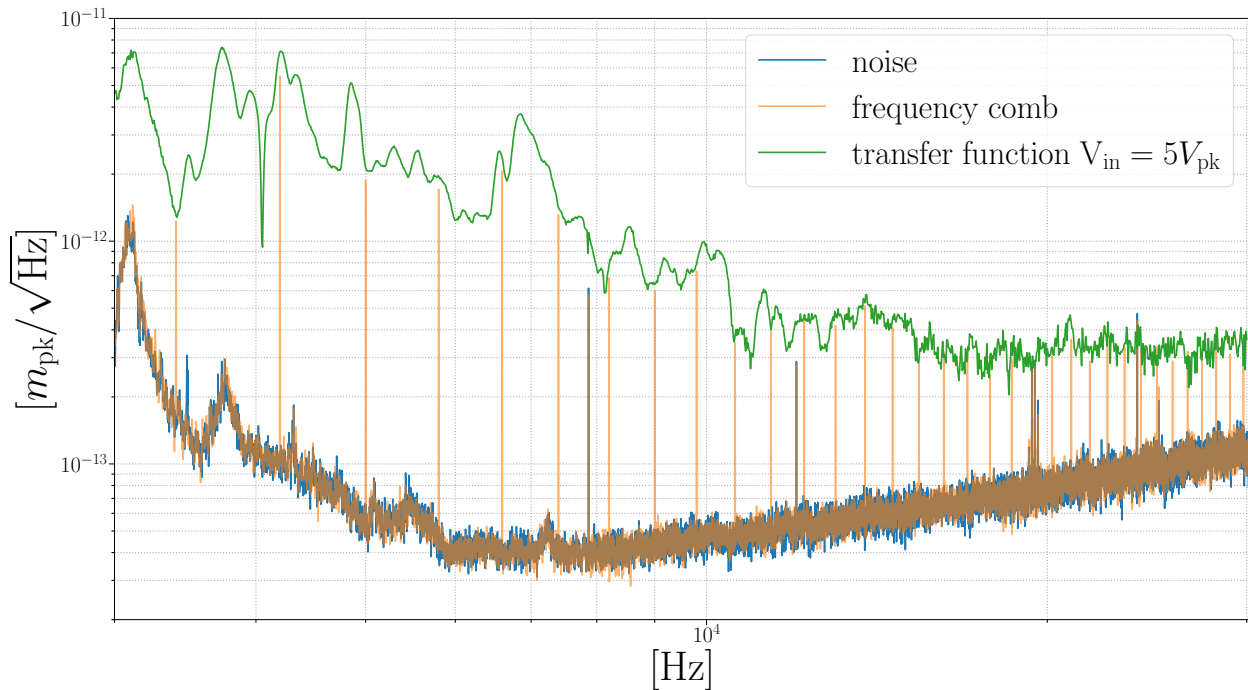


Figure 3.17: Assembly 1.2 and 1.3 transfer function measurement and separate noise displacement spectra measurement with the GaAs/Al_{0.92}Ga_{0.08}As sample installed. Measurements were taken from 3kHz up to 21kHz on using a Stanford Research 785 spectrum analyzer.

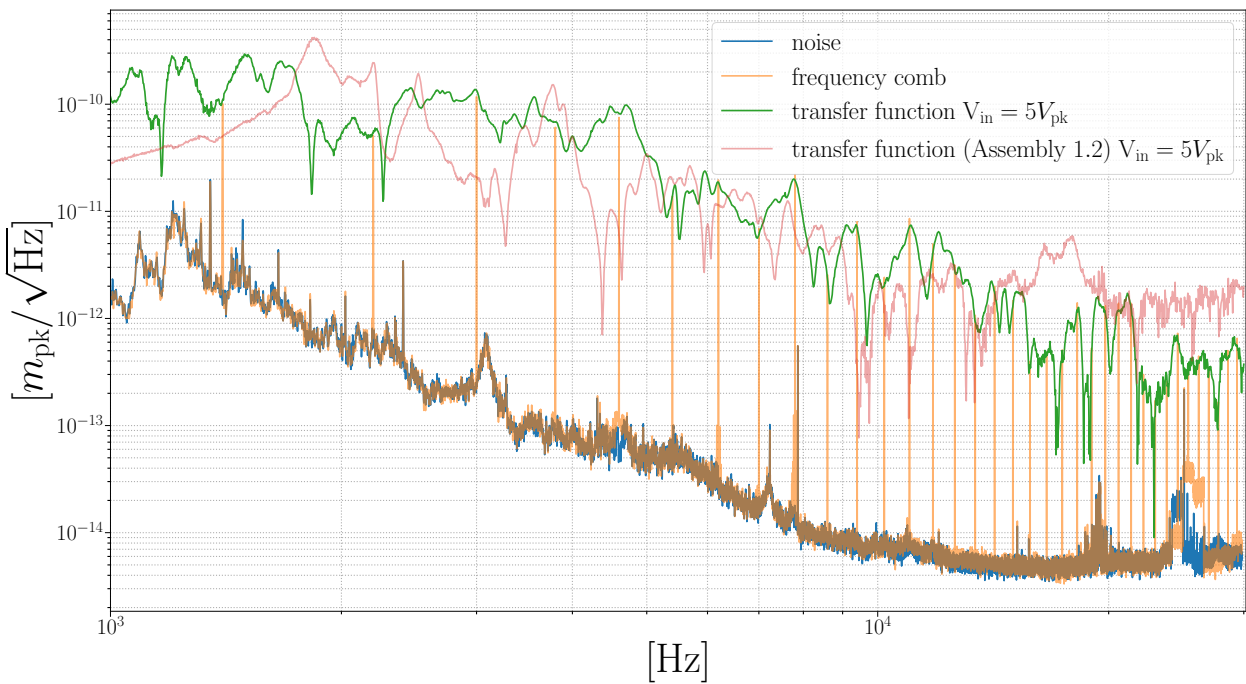


Figure 3.18: Assembly 1.2 and 1.3 transfer function measurement and separate noise displacement spectra measurement with a CVI Melles Griot flat mirror sample ($R \approx$ sample installed). Measurements were taken from 1kHz up to 30kHz on using a Stanford Research 785 spectrum analyzer.

Assembly 2

With considerations after Assembly 1, a more monolithic optical mount design with a simple geometry was imagined. PLA material compliance factoring to the seen drive noise. To see if it could be due to the compliance of the assembly material or printing, we tested this assembly design against different infills of PLA, PETG, and a version machined from solid PVC. With this modification, came also a different plate geometry. The assumption is the region of interest of the injection would not be heavily influenced by the non-circular plate geometry where it matters.

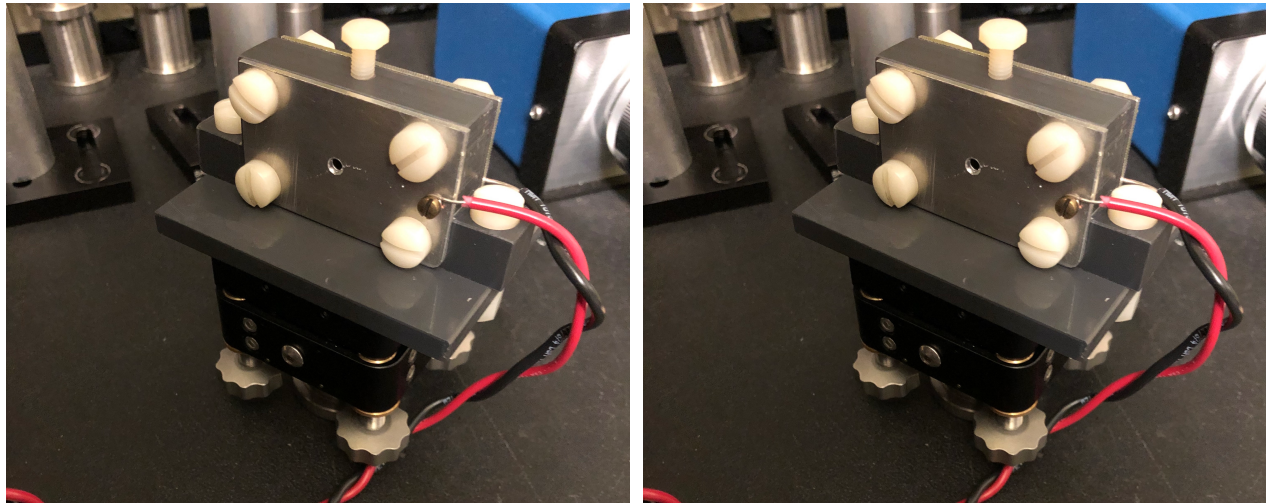


Figure 3.19: An iteration of assembly 2 comprised of a PVC mount with two rectangular (1.1"X2") plates with a central aperture of 3mm

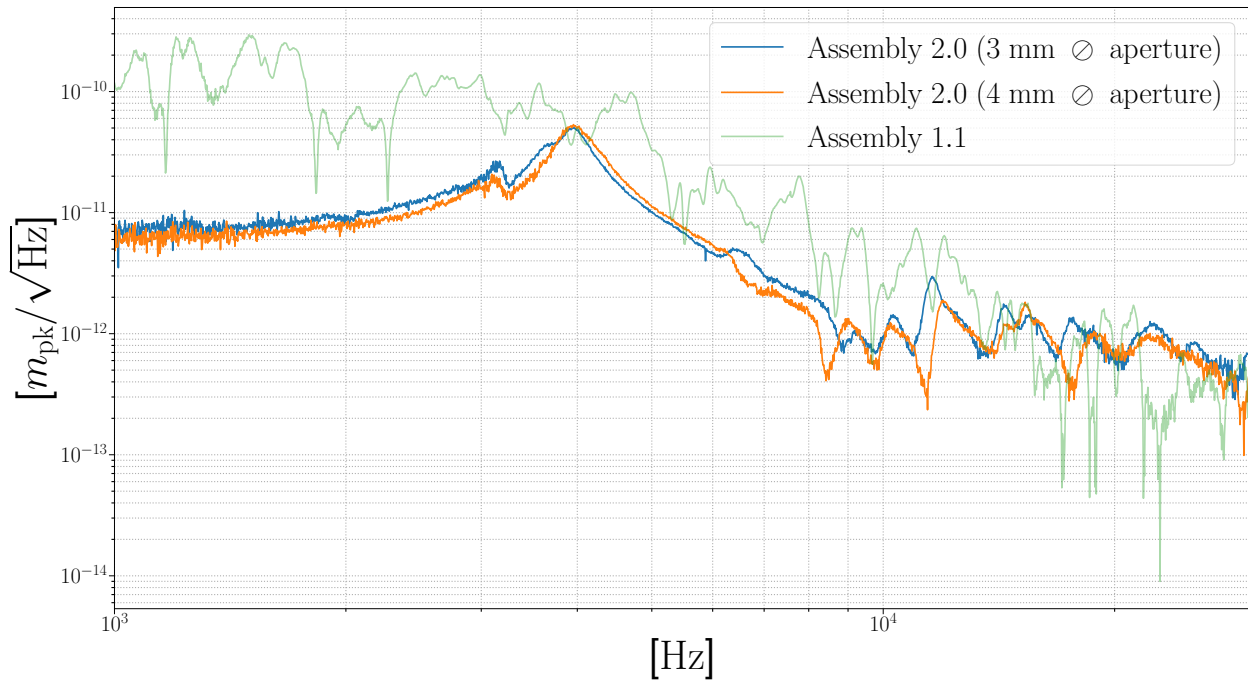


Figure 3.20: Assembly 2.0 transfer function measurements compared to Assembly 1.1, Measurements were taken from 1kHz up to 30kHz on using a Stanford Research 785 spectrum analyzer.

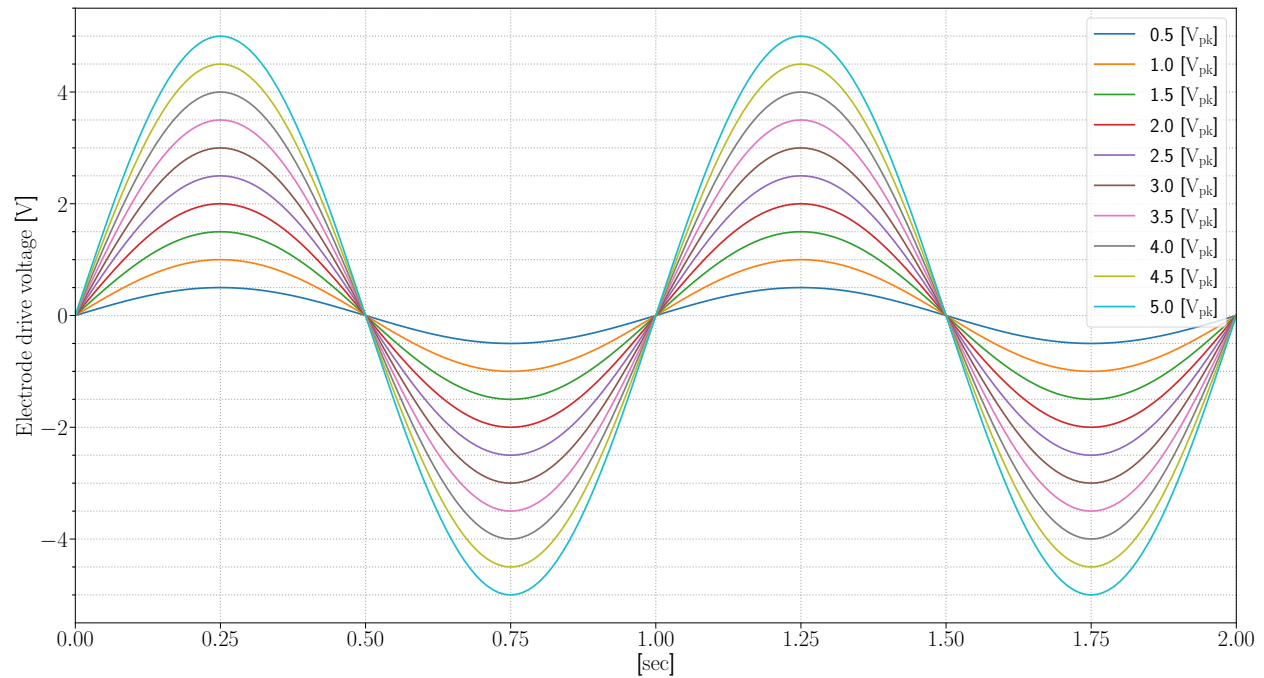


Figure 3.21: The varied drive amplitudes input into the HVA to perform the following test

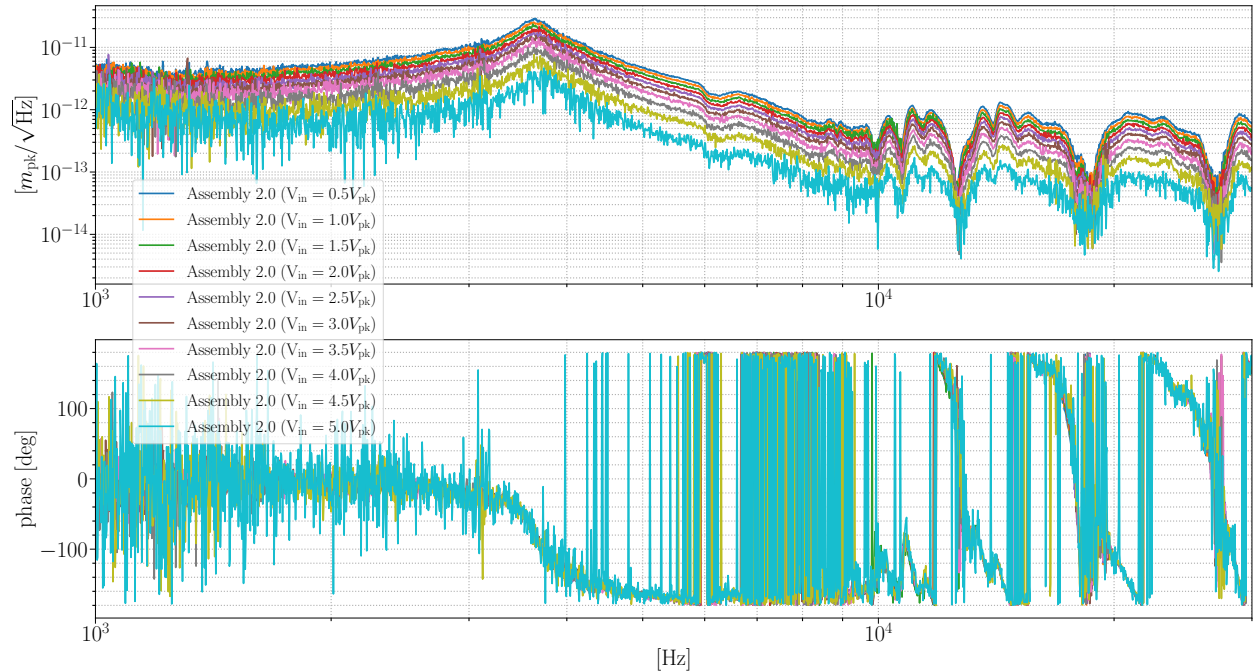


Figure 3.22: Assembly 2.0 transfer function measurements with varied drive amplitudes indicated in 3.21.

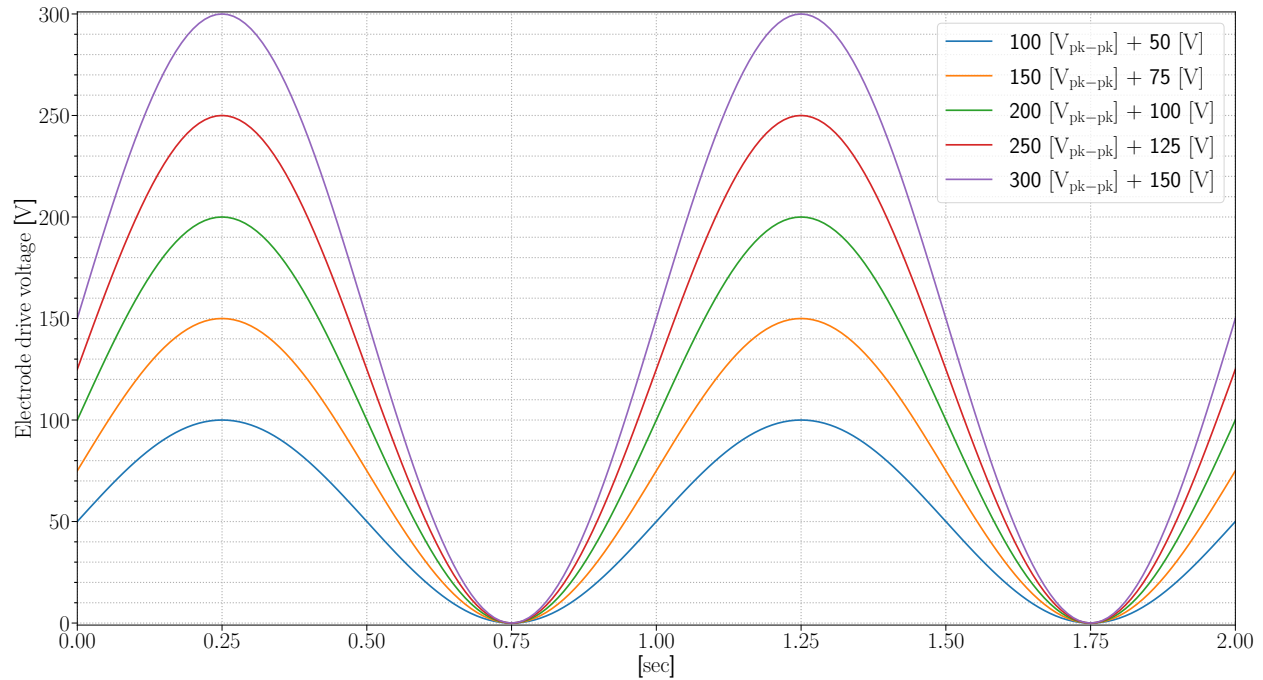


Figure 3.23: The varied drive amplitudes and offsets input into the HVA to perform the following test

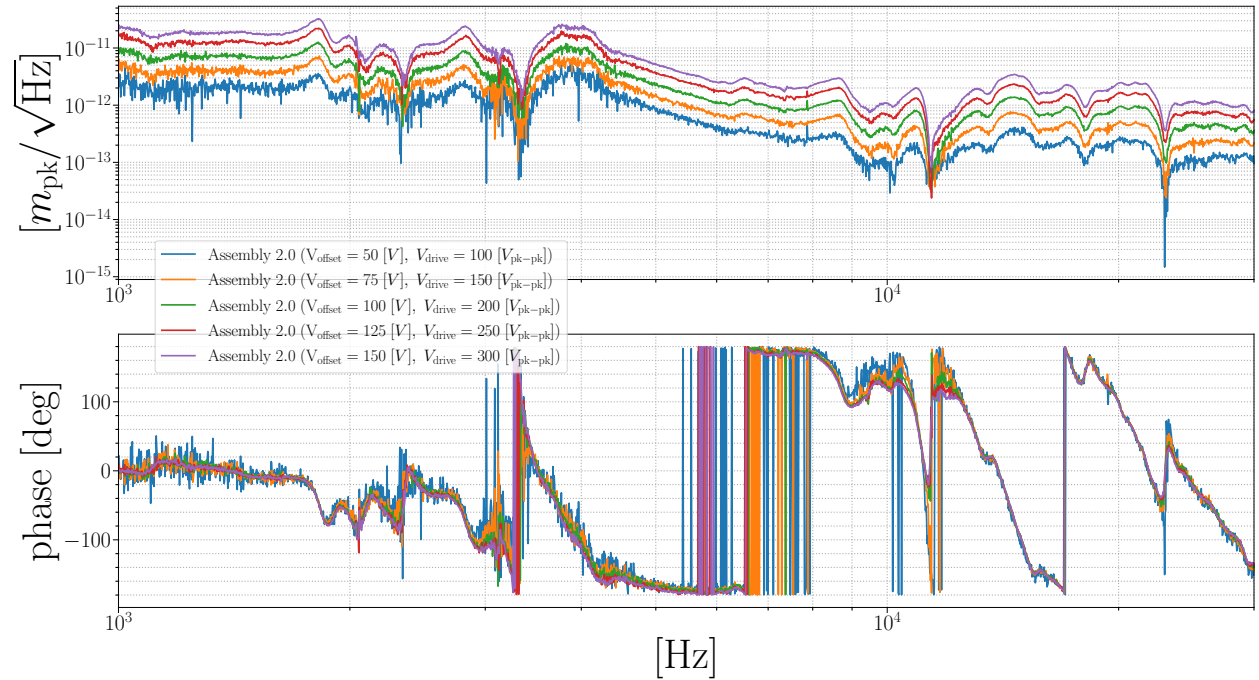


Figure 3.24: Assembly 2.0 transfer function measurements with varied drive amplitudes and offsets indicated in 3.23.

Assembly 3 (MACOR mount)

With most of the same characteristics from Assembly 3, an optical mount made of MACOR, a machinable ceramic, was constructed and installed. With the material's high Young's modulus (66.9 GPa), and a moderate Poisson ratio (.29) [21] making it by far the most durable / non-conductive mounting solution tried.

An optical mount for the sample made with MACOR, along with glass bearings .48 ± .01 cm Ø and a McMaster-Carr 8-32, 1/2" ceramic screw were used to clamp and suspend the optical sample. A 1.24" Ø hole was bored into the MACOR with a (**depth?**) depth so that there is a .351 ± mm clearance between the front and back surface of the sample to the electrode plates.

Figure with the sample in-situ

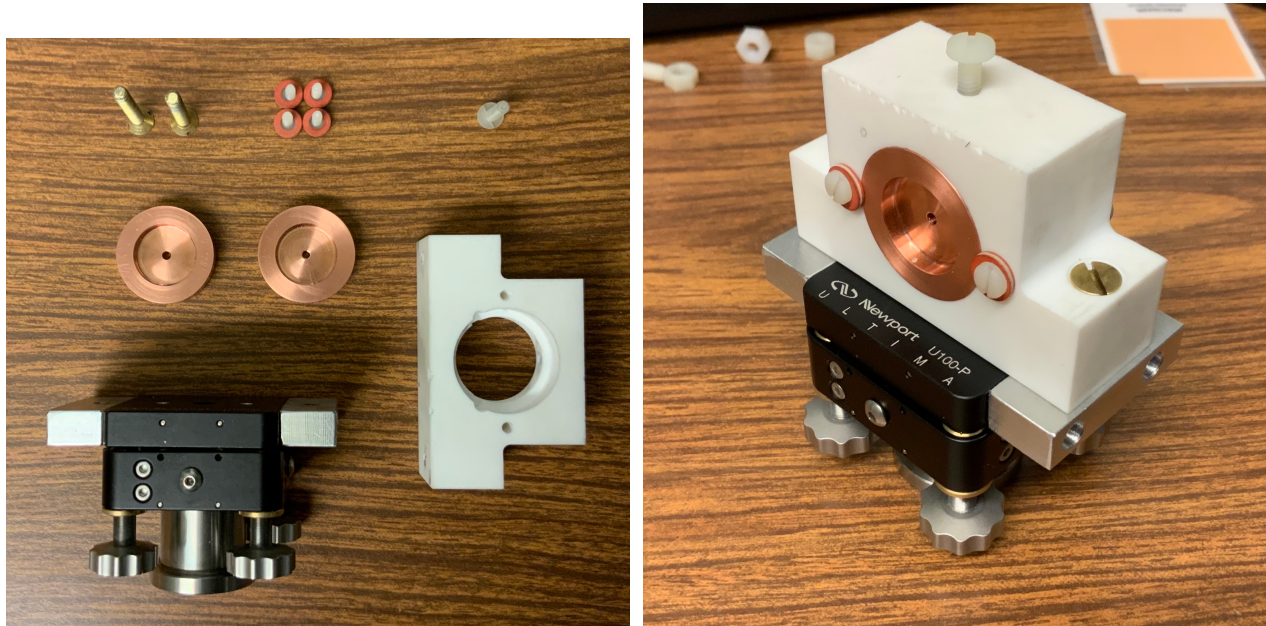


Figure 3.25: Assembly 3 the left hand figure is a disassembled configuration and the right hand side provides an isometric view of the assembled configuration.

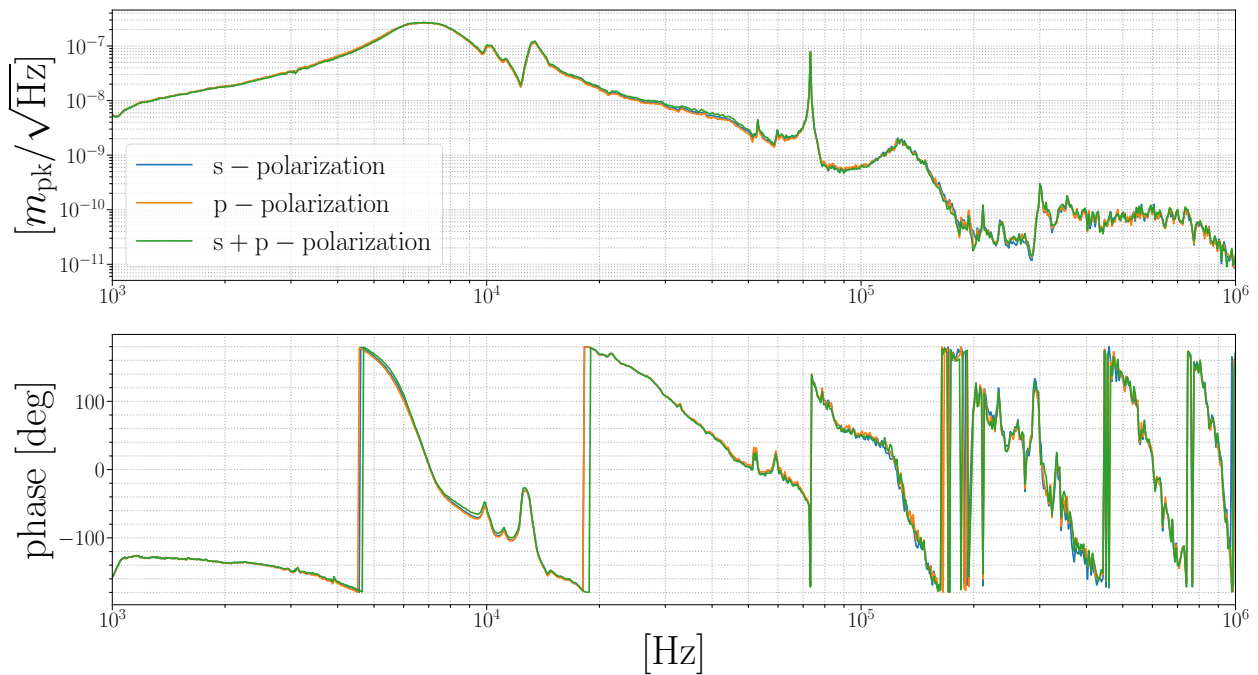


Figure 3.26: A polarization dependent test using the MACOR mont

Opto-mechanical coupling

During Assembly 2 tests the drive coupling seen in the transfer function measurements for all mounts tried was hypothesized to be due to mechanical action the assembly construction when driving the voltage on electrodes plates. Tracking consistent mechanical action for assemblies prior to Assembly 3 was difficult due to inconsistent mechanical settings between some measurements. More consistent measurements were realized when mechanical settings were tracked more carefully (i.e. set screw torque) and ceramic / glass materials used for suspending sample within the assembly. Sample and mount mechanical mode excitations. Seen with both AlGaAs and a HR coating from an AtFilm (IBS coating)

- **Vibration of plates (Leissa)** [22] Computing frequencies and order of magnitude
- Steve's COMSOL model results

Dual-polarization locked configuration

Chapter 4

Conclusion

4.1 Thermal compensation system comissioning for O3

Since the comissioning that had taken place in O3a, there has been heavy consideration into how point absorbers limits the high power operation of interferometric gravitational wave detectors and hence their sensitivity; from pre-installation measurements of ITM surface quality to the consideration of higher order thermal compensation.

4.2 AlGaAs Electro-optic effect

The discovery of driven mechanical couplings within the longitudinal pockels cell mount are discussed and was shown to be a major limitation when using large ([Mention range](#)) electric field injections indicated and have lead to an improved dual-polarization locked experimental design for improved sensitivity.

[Satoshi results](#) Though with limited sensitivity an upper limit with the experiment is established [cite paper with Satoshi notes](#).

Chapter 5

Appendix

5.1 The Equipartition theorem and the Fluctuation dissipation theorem

5.2 Mode matching data for Electro-optic sample cavity

5.2.1 Pre MMT beam scan

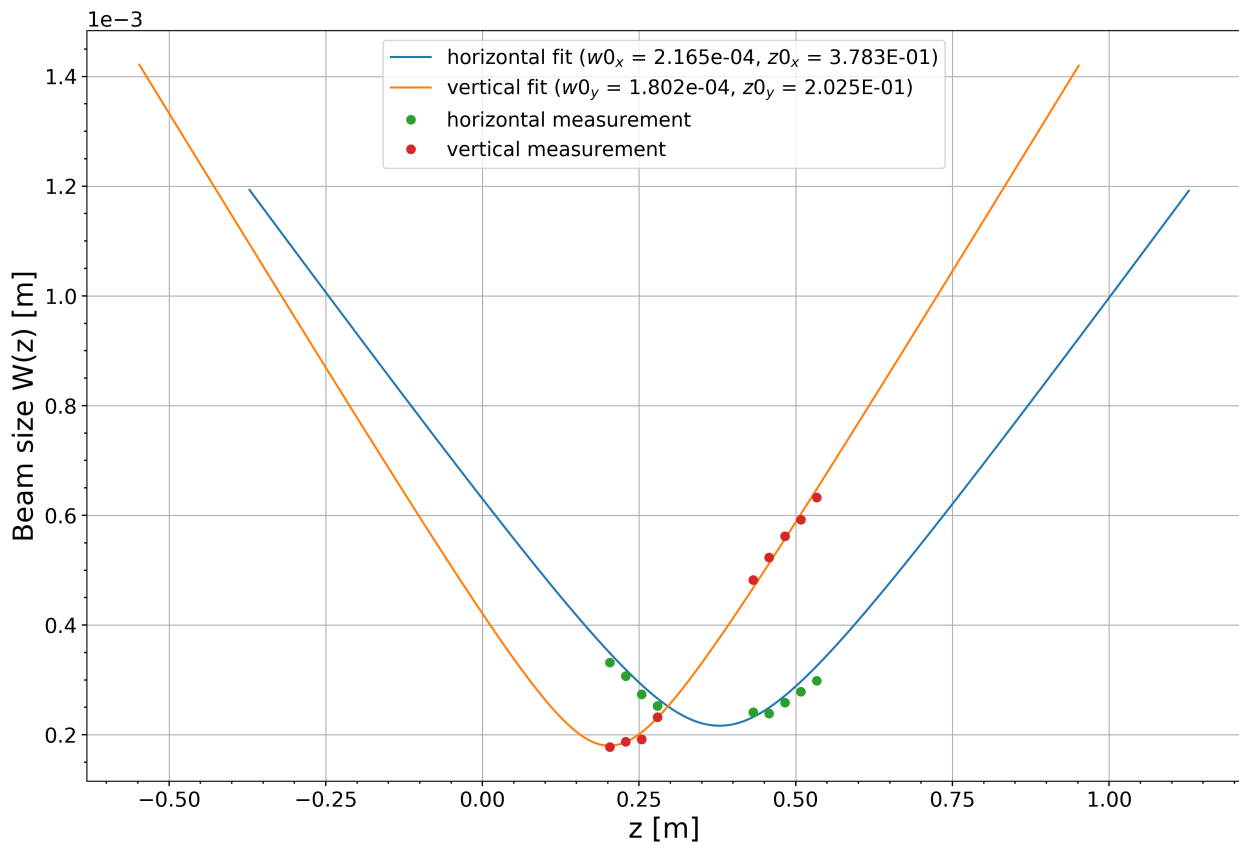


Figure 5.1: Beam scan taken from SM5 (Steering mirror 5)

5.2.2 “Just another mode matching tool” (JAMMT) solution

5.2.3 Post MMT beam scan

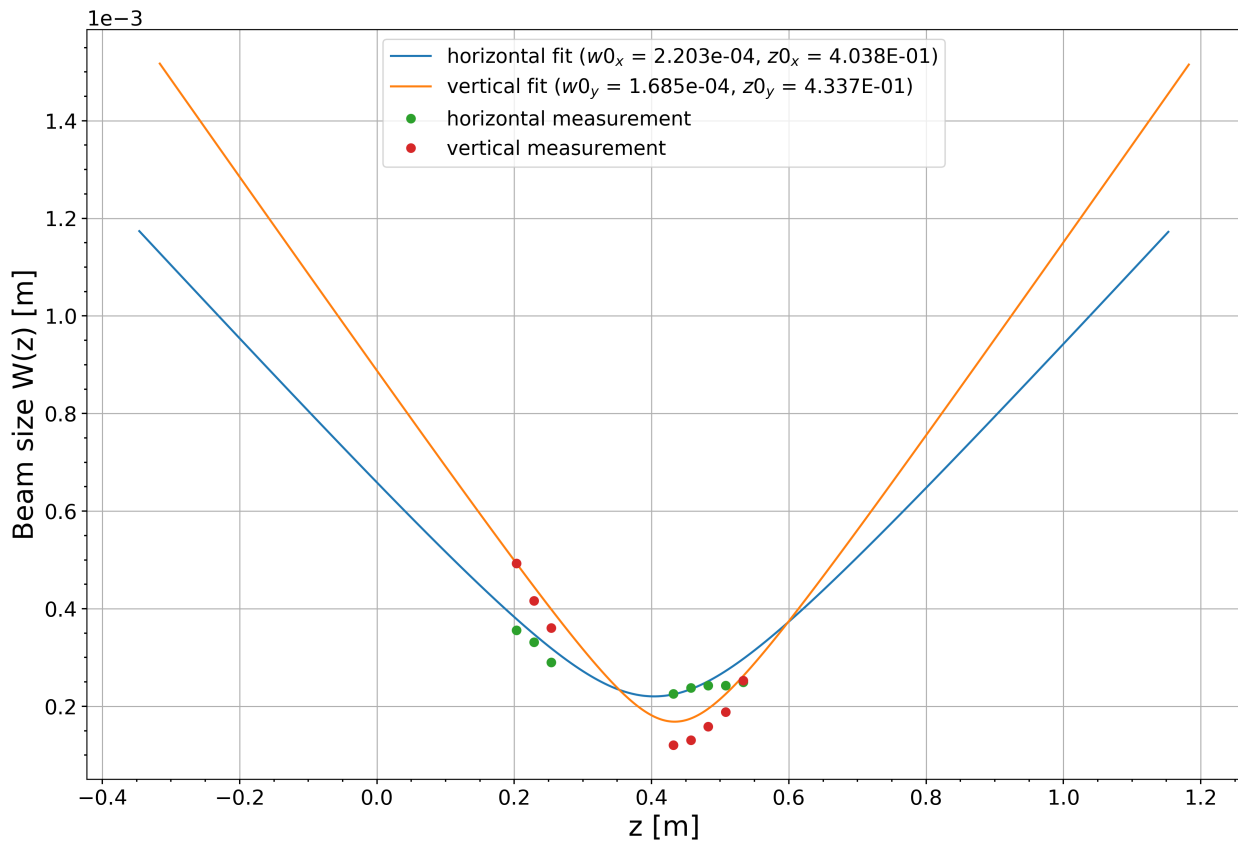


Figure 5.2: Beam scan taken from SM6. Sampling points before SM7 and after the first cavity iris.

5.2.4 Laser PZT sweep

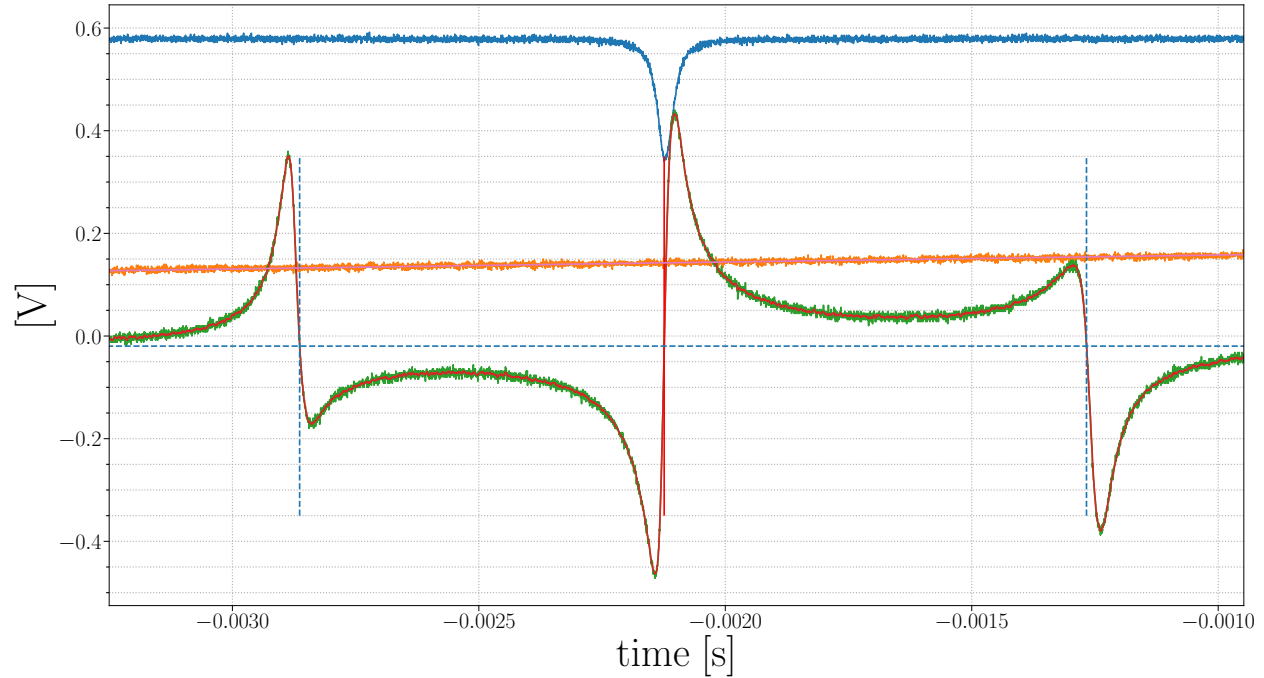


Figure 5.3: Ramping voltage sent to the laser PZT while probing the mixer output. The sweep was performed for sample cavity of length notes

5.3 Assembly blueprints and alternative views

5.3.1 Assembly 1

Cross section

Electrodes

Iteration 1.1

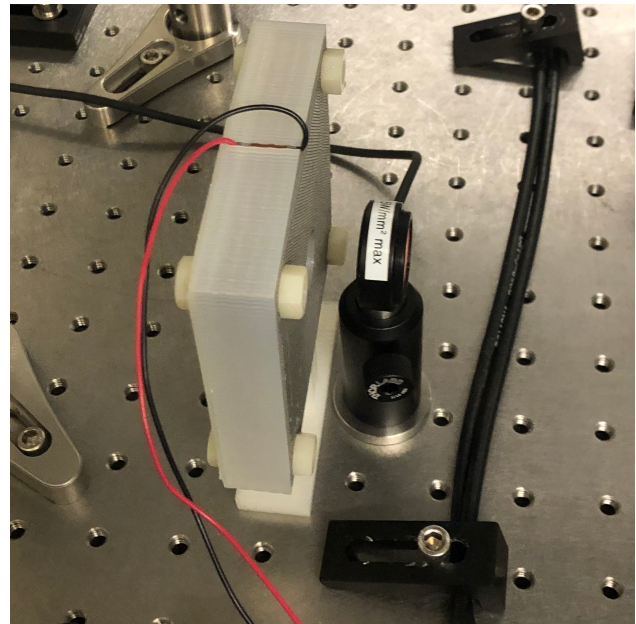
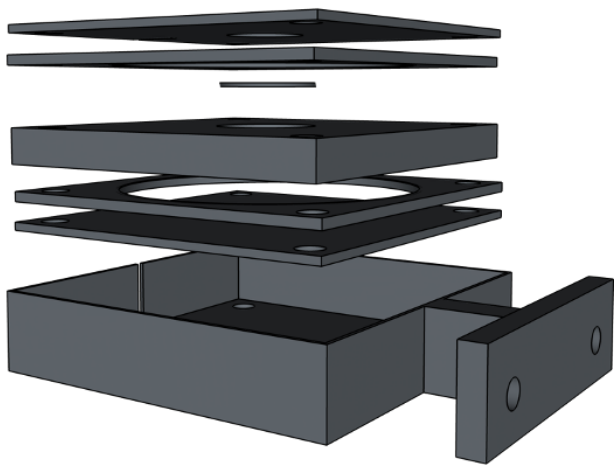


Figure 5.4: Assembly 0 was constructed to meet the criteria of providing a non-conductive housing for the electrode / sample assembly while maintaining a fixed length spacing using parts 3d printed with polylactic acid (PLA).

Iteration 1.2

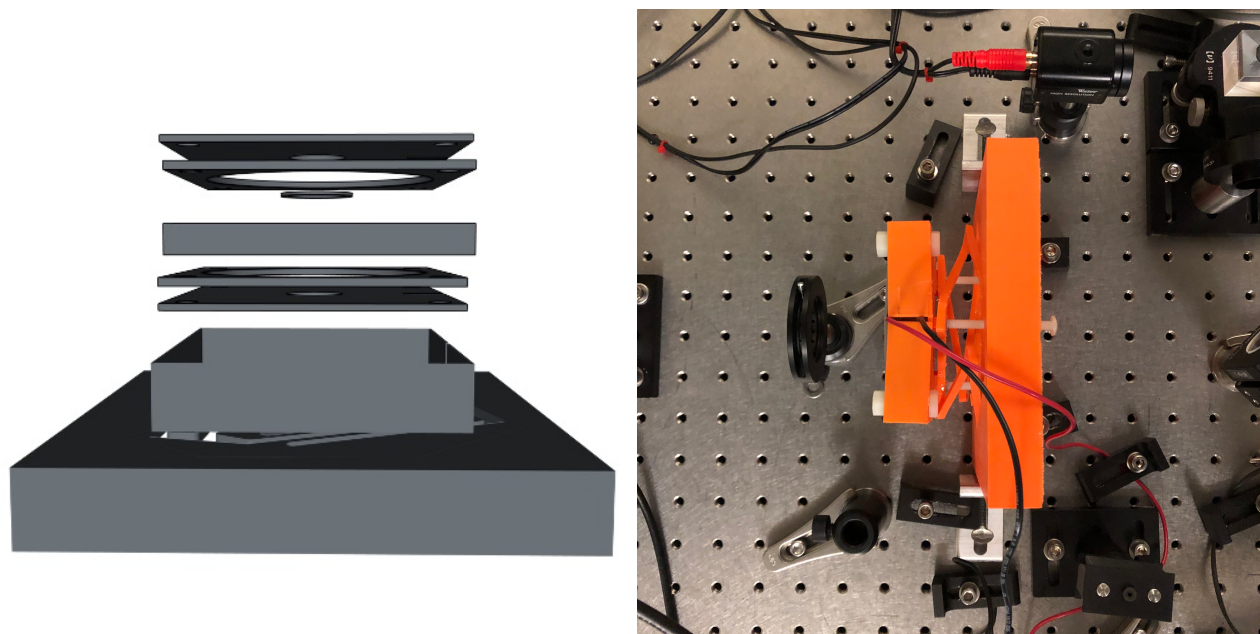


Figure 5.5: Assembly 1 was constructed to meet the criteria of providing a non-conductive housing for the electrode / sample assembly while maintaining a fixed length spacing using parts 3d printed with polylactic acid (PLA).

Iteration 1.3

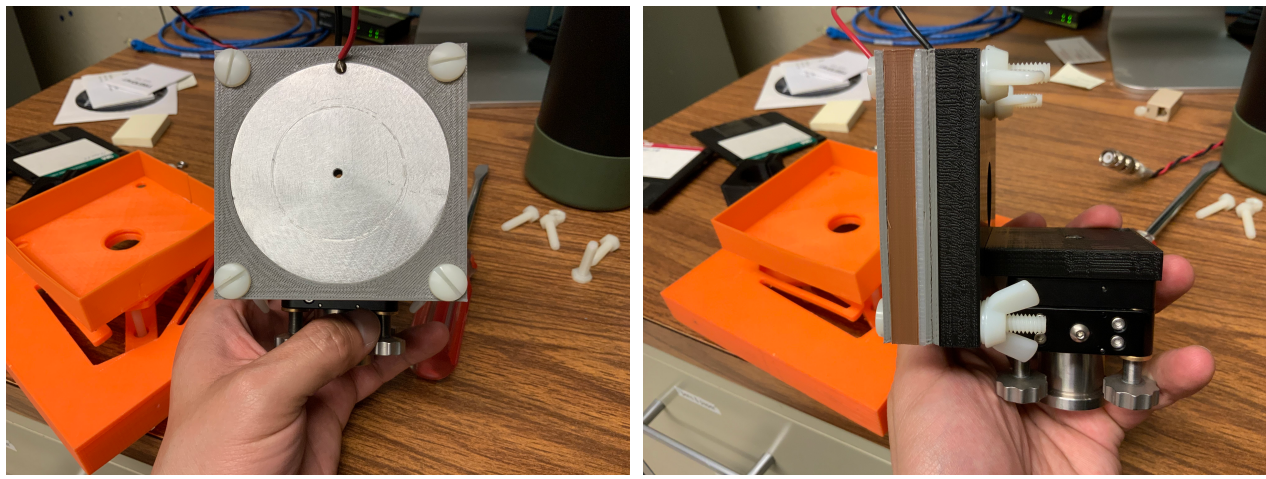


Figure 5.6: A modification implemented with the intention of reducing pitch dithering while still having control of DC YAW

5.3.2 Assembly 2

Cross section

Electrodes

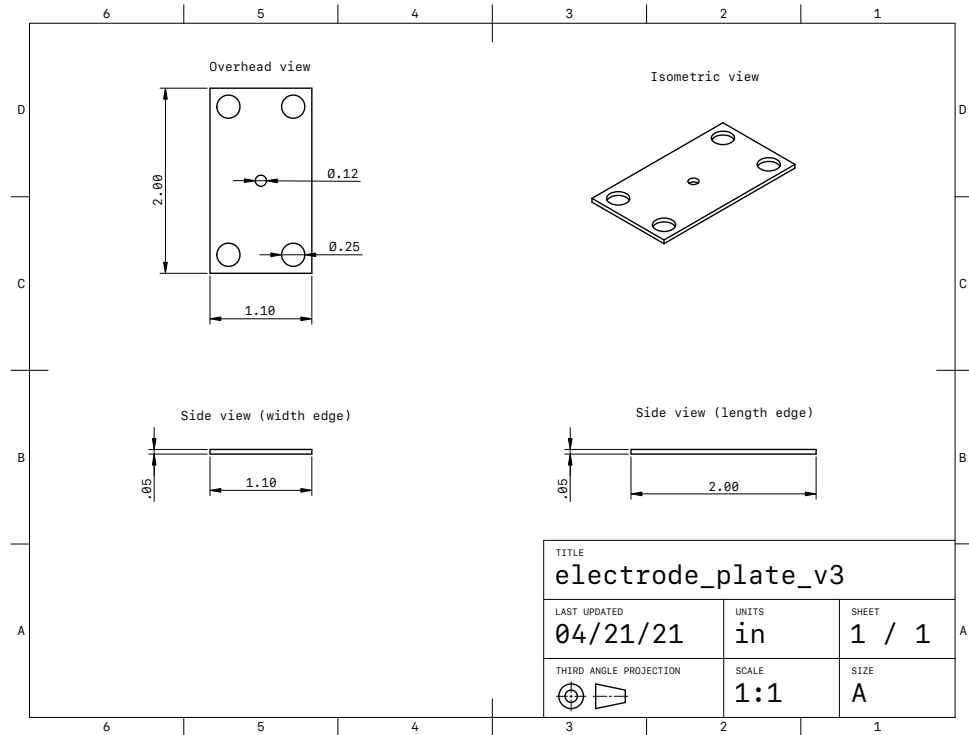


Figure 5.7: Rectangular (.05"X1.1"X2") plates made of aluminum.

Iteration 2.1

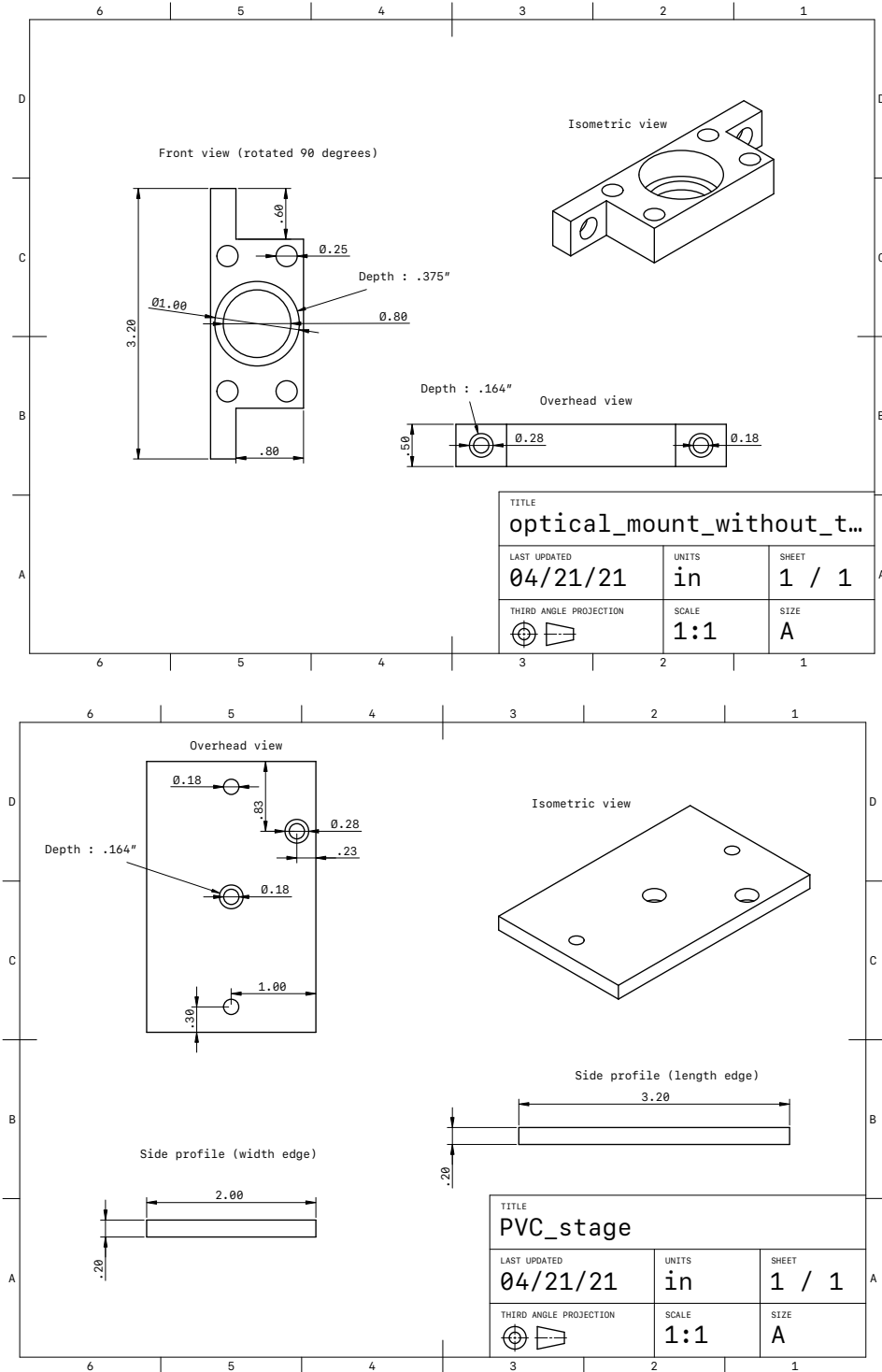


Figure 5.8: A design iteration of the assembly 2 mounts. Materials tried varied from PVC, PLA, and PETG. Quarter inch holes are bored in order to pass nylon screws holding electrode plates fixed to the mount.

Iteration 2.2

3D printed w/ MACOR spacers

Insert blueprints

Insert printed results

5.4 Assembly 3 [MACOR](blueprint)

Cross section

Electrodes

Iteration 3.0

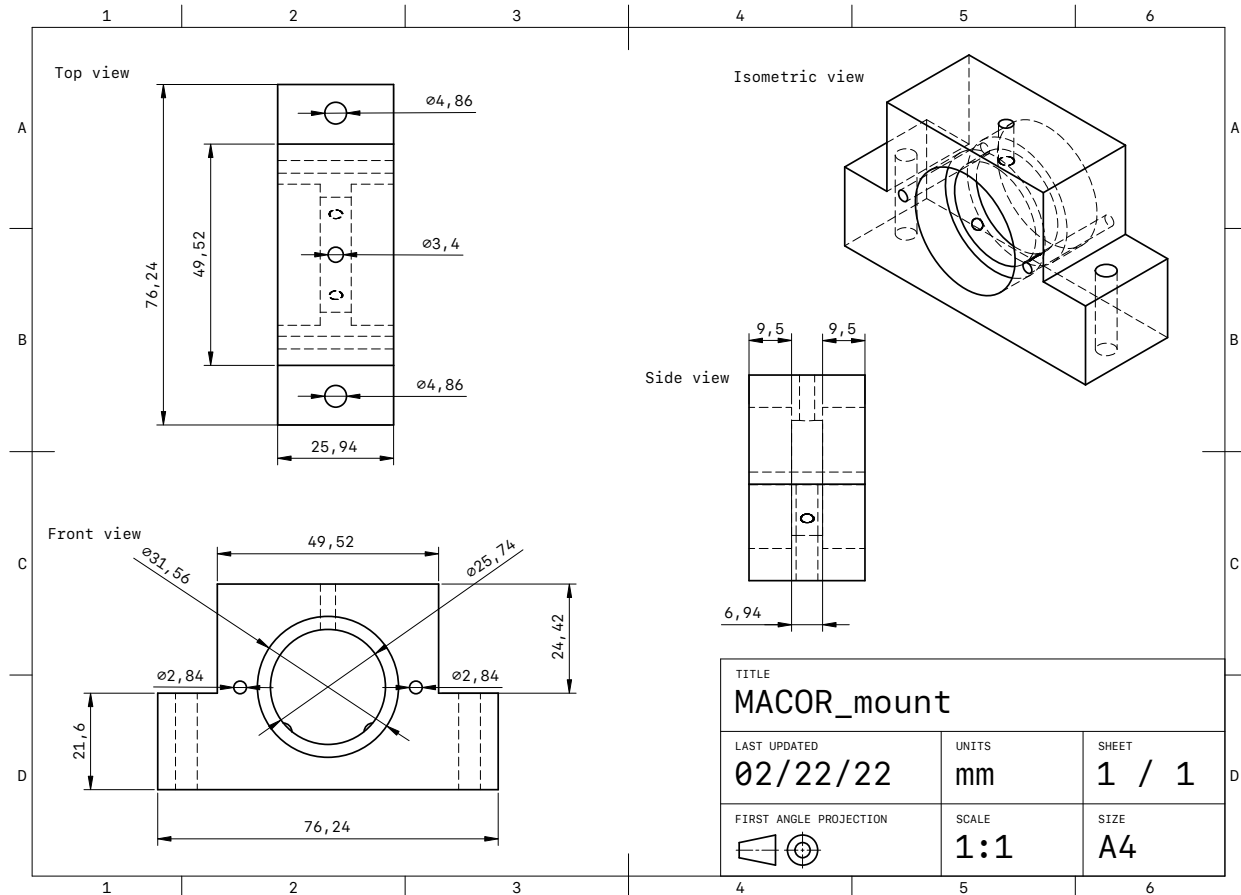


Figure 5.9: MACOR mount design constructed in Shapr3D

5.5 Calibration

Frequency dependent measurement : $\alpha(f)$

The calibration math for this measurement explicitly starts with what I call $\alpha(f)$ which is a vector of complex numbers that represents the transfer function $\text{CH2}(f)/\text{CH1}(f)$ where:

$$\text{CH1}(f) = \text{Source}(f)$$

and

$$\text{CH2}(f) = \frac{\text{S}(f) * \text{signal}(f)}{1 - \text{OLG}(f)}$$

Where

$$\text{OLG}(f) = \text{A}(f) * \text{S}(f)$$

and $\text{signal}(f)$ is the demodulated output from RFPD_{refl} and $\text{S}(f)$ is the transfer function of the frequency stabilization servo.

From here we solve for signal(f):

$$\text{signal}(f) = \text{CH2}(f) * \text{A}_1(f) * \text{A}_2 * \frac{(1 - \text{OLG}(f))}{\text{OLG}(f)}$$

Where $\text{A}_1(f)$ informs the frequency dependent drive sent to the laser PZT to keep the cavity locked and A_2 is the laser frequency detuning factor [Hz/V] (can be estimated from measuring PDH).

Currently $\text{signal}(f)$ provides a frequency noise spectra which then can be converted into a displacement spectra with the following relation:

$$\frac{\Delta f}{f_{\text{laser}}} = \frac{\Delta L}{L_{\text{cav}}}$$

This allows us to imagine the frequency noise spectra as a length noise spectra due to the drive on the electrodes:

$$\text{signal}(f) = \alpha(f) * \text{Source}(f) * \text{A}_1(f) * \text{A}_2 * \frac{(1 - \text{OLG}(f))}{\text{OLG}(f)} * \frac{L_{\text{cav}}}{f_{\text{laser}}} \quad [\text{m}_{\text{pk}}]$$

And for the measurement normalized by the drive voltage on the electrodes:

$$\frac{\text{signal}(f)}{\text{Source}(f) * \text{G}(f)} = \frac{\alpha(f)}{\text{G}(f)} * \text{A}_1(f) * \text{A}_2 * \frac{(1 - \text{OLG}(f))}{\text{OLG}(f)} * \frac{L_{\text{cav}}}{f_{\text{laser}}} \quad \left[\frac{\text{m}_{\text{pk}}}{V_{\text{pk}}} \right]$$

Noise or single frequency drive measurement : $n(f)$

The calibration math for this measurement is essentially equivalent to the transfer function measurement above. The only difference is:

$$\text{CH1}(f) = \frac{\text{S}(f) * \text{signal}(f)}{1 - \text{OLG}(f)}$$

and

$$\text{signal}(f) = \text{CH1}(f) * \text{A}_1(f) * \text{A}_2 * \frac{(1 - \text{OLG}(f))}{\text{OLG}(f)} * \frac{L_{\text{cav}}}{f_{\text{laser}}}$$

Where $\text{signal}(f)$ in this measurement represents the free running cavity displacement noise with the exception of a single frequency if it is not a noise measurement.

If $\text{CH1}(f)$ is in $\frac{V_{\text{rms}}}{\sqrt{\text{Hz}}}$ then $\text{signal}(f)$ will be in $\frac{m_{\text{rms}}}{\sqrt{\text{Hz}}}$

or

If $\text{CH1}(f)$ is in V_{pk} then $\text{signal}(f)$ will be in m_{pk}

Calibration code

Import packages

If it fails the first time try installing the following to a separate conda environment: /pydependencies/eo_calibrate.yml

```
[11]: import glob
import numpy as np
import matplotlib.pyplot as plt
from matplotlib import rc
import os
import h5py

plt_style_dir = 'pydependencies/stylelib/'

if os.path.isdir(plt_style_dir) == True:
    plt.style.use(plt_style_dir + 'pptsize') # This just sets a python figure style (you can adjust it to your preferences)
```

Frequently used functions:

```
[12]: def concat_vecs(directory):
    """
    Takes a directory filled with spectra measurements (from SR785) to be concatenated to a single vector. The output of the function is (frequency vector, amplitude vector)
    """
    txtcounter = len(glob.glob1(directory, "*.TXT"))
    freq = np.zeros((801,txtcounter))
```

CHAPTER 5. APPENDIX

```

freq1 = np.zeros((801,txtcounter))
vpk = np.zeros((801,txtcounter))

columns = range(0,txtcounter)
fff = 0
vpkn = 0
## import and measurements
for i in columns:
    data = np.loadtxt(directory + str(i).zfill(2) + '.TXT')
    freq[:,i] = data[:,0]
    vpk[:,i] = data[:,1]
    if i == columns[0]:
        fff = freq[:,i]
        vpkn = vpk[:,i]
    elif i == columns[-1]:
        fff = np.append(fff,freq[:,i])
        vpkn=np.append(vpkn,vpk[:,i])
    else:
        fff = np.append(fff, freq[:,i][:-1])
        vpkn = np.append(vpkn, vpk[:,i][:-1])
return fff, vpkn

def gen_concat_vecs(directory):
    """
    Takes a directory filled with spectra measurements (from SR785) to be
    concatenated to a single vector. The output of the function is (frequency
    vector, amplitude vector)
    """
    txtcounter = len(glob.glob1(directory,"*.TXT"))
    columns = range(0,txtcounter)

    data = np.loadtxt(directory + str(0).zfill(2) + '.TXT')
    master_freq = data[:,0]
    master_data = data[:,1]

    for i in columns:
        if i < columns[-1]:
            data = np.loadtxt(directory + str(i).zfill(2) + '.TXT')
            data1 = np.loadtxt(directory + str(i+1).zfill(2) + '.TXT')
            xy, xind, yind = np.intersect1d(data[:,0], data1[:,0], \
            return_indices=True)

            if sum(yind>400) != 0:
                xy2, xind2, yind2 = np.intersect1d(master_freq, data1[390:,0], \
                return_indices=True)
                master_freq = np.append(master_freq[:xind2[0]-11], \
                data1[390:,0])

```

CHAPTER 5. APPENDIX

```
    master_data = np.append(master_data[:,(xind2[0]-11)], \
        data1[390:,1])

    else:
        if len(xy) != 0:
            master_freq = np.append(master_freq, data1[yind[-1]+1:,0])
            master_data = np.append(master_data, data1[yind[-1]+1:,1])
        else:
            master_freq = np.append(master_freq, data1[:,0])
            master_data = np.append(master_data, data1[:,1])

    return master_freq, master_data

def transfer_function(amplitude, phase):
    """
    Takes frequency response data (amplitude and phase) combines it into a
    transfer function :  $Ae^{(i\phi)}$ 
    """
    return 10**((amplitude/20)* np.exp(1j*(phase/180)*np.pi))

def phase_wrap(phase_array, type='deg'):
    """
    Wraps phase from -180 -> +180 degrees if type == 'rad' then it wraps from
    -pi -> pi
    """
    if type == 'deg':
        fin_phase_array = (phase_array + 180) % (2 * 180) - 180
    if type == 'rad':
        fin_phase_array = (phase_array + np.pi) % (2 * np.pi) - np.pi
    return fin_phase_array

def function_transfer(freq,tf_in):
    """
    Converts transfer function back to amplitude and phase data (frequency, □
    ↳amplitude [dB], phase [deg])
    """
    db = 20*np.log10(abs(tf_in))
    deg = np.angle(tf_in, deg=True)
    return freq, db, deg

def tf_import(tf_path):
    """
    Takes a directory containing amplitude and phase data (dB and deg) and
    imports the data and outputs (frequency, amplitude, phase)
    """
    db = np.loadtxt(tf_path + 'db.TXT')
    deg = np.loadtxt(tf_path + 'deg.TXT')
```

```

ff = db[:,0]
return ff, db[:,1], deg[:,1]

def tf_interpolate(new_freq, tf_tuple):
    """
    """
    """
    new_db = np.interp(new_freq, tf_tuple[0], tf_tuple[1])
    new_deg = np.interp(new_freq, tf_tuple[0], tf_tuple[2])
    return new_freq, new_db, new_deg

def bode_plt(tf_tuple, save_path, lbl, title, ylbl='dB'):
    ff = tf_tuple[0]
    db = tf_tuple[1]
    deg = tf_tuple[2]
    bode_fig = plt.figure()
    plt.subplot(211)
    if not ylbl=='dB':
        plt.loglog(ff, db, label=lbl)
    else:
        plt.semilogx(ff,db, label = lbl)
    plt.xlim(ff[0], ff[-1])
    plt.ylabel(ylbl)
    plt.legend()
    plt.title(title.replace('_', '\_'))
    plt.subplot(212)
    plt.semilogx(ff,deg, label = lbl)
    plt.xlim(ff[0], ff[-1])
    plt.legend()
    plt.xlabel('Frequency [Hz]')
    plt.ylabel('phase [deg]')
    plt.savefig(save_path + '/' + title + '.png', dpi=300,bbox_inches='tight')
    plt.close()
    return bode_fig

def h5_import(dir):
    return h5py.File(dir + '/data.hdf5', 'r')

def printname(name):
    print(name)

def h5_peek(h5_file):
    if type(h5_file) == str:
        h5_data = h5_import(h5_file)
    else:
        h5_data = h5_file

```

CHAPTER 5. APPENDIX

```
return h5_data.visit(printname)

def qkh5plt(h5_file,meas,lbl,axis,yax='log',lgnd_size=30,peek=False):
    """
    Plotting tool that allows you to quickly plot any one of the traces from an
    h5 file.

    h5_file : Can be an already open h5 file or a directory to an h5 file

    meas : The measurement you wish to select from the options in the h5 file

    axis : needs to inherit axis from already established figure

    lbl : Label we want to tag onto the requested dataset

    yax : can swap between a logarithmic and linear yaxis

    lgnd_size : size of legend font
    """

    if type(h5_file) == str:
        h5_data = h5_import(h5_file)
    else:
        h5_data = h5_file

    if peek == True:
        h5_peek(h5_file)

    if yax == 'log':
        axis.loglog(h5_data['freq'][:,],h5_data[meas] [:],label=lbl)
    elif yax == 'lin':
        axis.semilogx(h5_data['freq'][:,],h5_data[meas] [:],label=lbl)

    axis.legend(prop={'size':lgnd_size})
    plt.xlim(h5_data['freq'][0],h5_data['freq'][-1])
```

Input variables

```
[23]: meas_data_dir = 'measurements/swept/algas/08_13_2021/meas1/'
      # directory where the uncalibrated data lives
date = '08_13_2021'
# date when measurement was taken ("mm_dd_yyyy")
final_dir = 'results/'
# directory where the final data will live
```

```

meas_type = 'swept'
    ↪# type of measurement taken tag (i.e. noise, swept)
spectra_type = 'pk'
    ↪# spectra type (i.e. pk, rms)
sample = 'algaas'
    ↪# sample tag (i.e. algaas, atfilms, sio2tao5, etc.)
xtradir = 'meas1'
    ↪# this label helps distinguish between measurements taken in a given day
cav_length = .165
    ↪# recorded length of cavity
inp_voltage_swept = 4.65
    ↪# voltage sent from SR785 to HVA connected to electrodes
plot_saving = False
    ↪# generate and save .png files for intermediate calibration functions
model = False
    ↪# boolean that decides whether or not the model estimate should be plotted
    ↪with calibrated data

```

[24]:

```

labl = date + '_' + meas_type + '_' + spectra_type + '_' + sample
    ↪# label of the directory containing all the figures and .h5 file
if xtradir != 'none':
    ↪# adjusted label if an extra directory was used
    labl = date + '_' + meas_type + '_' + spectra_type + '_' + xtradir + \
        '_' + sample
new_final_dir = final_dir + '/' + labl

if os.path.isdir(new_final_dir) == False:
    ↪# generates the directory containing the results if it doesn't already exist
    os.mkdir(new_final_dir)

```

Data import

[25]:

```

#HVA and OLG directory search
HVA_common_dir = 'measurements/HVASVR_tf/'                                # HVA and
    ↪OLG directories
OLG_common_dir = 'measurements/OLG/'
HVA_dir = HVA_common_dir + 'HVACH3_plus_pomona/' + date + '/'
#OLG_dir = OLG_common_dir + date + '/'
OLG_dir = OLG_common_dir + sample + '/' + date + '/'

if xtradir != 'none' and meas_type != 'noise':
    HVA_dir = HVA_dir + xtradir + '/'
    OLG_dir = OLG_dir + xtradir + '/'

```

```

HVA = tf_import(HVA_dir) #_
    ↳import the HVA and OLG data
OLG = tf_import(OLG_dir)
    ↳If the data is a swept frequency measurement
if meas_type == 'swept': #_
    ↳import HVA CH1 transfer function data for transfer function measurement
    HVA_CH1_dir = HVA_common_dir + 'HVACH1/' + date + '/'
        ↳HVA_CH1_dir = HVA_common_dir + 'HVACH1_w_LPF/' + date + '/'
    if xtradir != 'none':
        HVA_CH1_dir = HVA_CH1_dir + xtradir + '/'

electrode_type = 'disk' #_
    ↳import low pass measurement from resistor / electrode capacitance
if sample == 'sio2ta2o5' or sample == 'atfilms':
    Electcap_dir = 'measurements/electrode_capacitence/' + \
        electrode_type + '/' + sample + '/03_29_2021/'
if sample == 'atfilms':
    Electcap_dir = 'measurements/electrode_capacitence/' + \
        electrode_type + '/' + sample + '/06_04_2021/'
if sample == 'algaas':
    Electcap_dir = 'measurements/electrode_capacitence/' + \
        electrode_type + '/' + sample + '/03_10_2021/'

meas_swept = tf_import(meas_data_dir) #_
    ↳import transfer function measurement
if plot_saving == True: #_
    ↳plot uncalibrated transfer function measurement if requested
    bode=plt(meas_swept, new_final_dir, date.replace("_", "\_"), \
        'Pockels_effect_frequency_response_uncalibrated_dB')

swept_tf = transfer_function(meas_swept[1], meas_swept[2]) #_
    ↳combine amplitude and phase

HVA_CH1 = tf_import(HVA_CH1_dir) #_
    ↳HVA CH1 import and interpolation (interpolate to transfer function frequency vector)
HVA_CH1_inter = tf_interpolate(meas_swept[0], HVA_CH1)
HVA_CH1_tf = transfer_function(HVA_CH1_inter[1], HVA_CH1_inter[2])

#Electrode capacitance transfer function import and interpolation
ECAP = tf_import(Electcap_dir) #_
    ↳Import and interpolate LPF measurement (part of frequency dependent drive to electrodes)
ECAP_inter = tf_interpolate(meas_swept[0], ECAP)
ECAP_tf = transfer_function(ECAP_inter[1], ECAP_inter[2])

```

```

#interpolate related tfs
HVA_inter = tf_interpolate(meas_swep[0], HVA) #_
→HVA CH3 and OLG interpolation
OLG_inter = tf_interpolate(meas_swep[0], OLG)

else: #_
→if the measurement is not a transfer function (spectra measurement)
spectra = gen_concat_vecs(meas_data_dir) #_
→changed from concat_vecs to gen_concat_vecs (07-25-2021)
#interpolate related tfs
HVA_inter = tf_interpolate(spectra[0], HVA) #_
→HVA CH3 and OLG interpolation
OLG_inter = tf_interpolate(spectra[0], OLG)
if plot_saving == True:
    #Spectra plotting
    plt.loglog(spectra[0], spectra[1], label=lbl.replace("_", "\_"))
    plt.legend()
    plt.xlabel('frequency [Hz]')
    #plt.xlim([spectra[0][0],spectra[0][-1]])
    if spectra_type == 'pk':
        plt.ylabel('$$V_{\mathsf{pk}}$$')
    elif spectra_type == 'rms':
        plt.ylabel('$$V_{\mathsf{rms}}$$')
    plt.savefig(new_final_dir + '/v_spectra_' + lbl + '.png', dpi=300, \
bbox_inches='tight')
    plt.close()

if plot_saving == True: #_
→plot and HVACH3 and OLG if requested
    #HVA plotting
    bode_plt(HVA, new_final_dir, 'HVA.75\_total\_gain', 'HVACH3+pomona')
    #OLG plotting
    bode_plt(OLG, new_final_dir, date.replace('_', '\_'), 'OLG' )

```

Build calibration function

```
[26]: HVA_tf = transfer_function(HVA_inter[1], HVA_inter[2]) #_
→combine amplitude and phase of HVACH3 and OLG
OLG_tf = transfer_function(OLG_inter[1], OLG_inter[2])

if meas_type == 'swept':
    volt_divider = False #_
→Voltage divider if you want a smaller normalization factor
```

```

if volt_divider == True: #_
    ↵Voltage divider with r_1 as the first resistor and r_2 as the resistor_
    ↵connected to ground
    r_1 = 100000
    r_2 = 50
    pom_vdivider = (r_2)/(r_1+r_2)

    swept_tf = swept_tf*pom_vdivider
else:
    pom_vdivider = 1

stf_unnorm = swept_tf*inp_voltage_swept #_
    ↵Unnormalized transfer function measurement

s_unnorm = [meas_swept[0], abs(stf_unnorm), np.angle(stf_unnorm, \
deg=True)] #_
    ↵Unnormalized transfer function in triad format

if plot_saving == True: #_
    ↵Plot voltage spectra for transfer function measurement if requested
        bode=plt(s_unnorm, new_final_dir, date.replace('_', '\_'), \
        'Pockels_effect_frequency_response_vspectra', \
        ylbl='$V_{\mathrm{pk}}$')

v_direct = inp_voltage_swept*HVA_CH1_tf*ECAP_tf #_
    ↵This is the voltage directly across the coating for all measured frequencies_
    ↵(with phase information)
vdirec = [meas_swept[0], abs(v_direct), np.angle(v_direct,deg=True)] #_
    ↵Frequency dependent injection voltage (transfer function triad)
if plot_saving==True: #_
    ↵Plot frequency dependent injection voltage if requested
        bode=plt(vdirec, new_final_dir, date.replace('_', '\_'), \
        'Potential difference across electrodes', ylbl='$V_{\mathrm{pk}}$')

#laserV2Hz = 2.0e6
#laserV2Hz = 1.4706e6 #_
    ↵measurement from elog 831 (05-24-2021)
laserV2Hz = 1.748e6 #_
    ↵Laser PZT response acquired from PDH measurement
HzpV = HVA_tf*laserV2Hz #_
    ↵Actuation function A(f) = A_1(f)*A_2(f)

CLG = 1/(1-OLG_tf) #_
    ↵Closed loop gain

```

CHAPTER 5. APPENDIX

```

CAL = OLG_tf*CLG #_
    ↳ Loop gain calibration factor
#CALVpHz=CAL/HzpV #_
    ↳ Calibrated voltage to frequency
CALHzpV=HzpV/CAL #_
    ↳ Calibration factor using A(f) and OLG(f)

if meas_type == 'swept': #_
    ↳ Calibrate data
    freq_noise = CALHzpV*stf_unnorm
else:
    freq_noise = abs(CALHzpV)*spectra[1]

if plot_saving == True and meas_type != 'swept': #_
    ↳ if plotting spectra measurement this is plotting and saving the frequency noise if requested
    plt.loglog(spectra[0], freq_noise, label= date.replace('_', '\_'), \
    linewidth=3)
    #plt.xlim([spectra[0][0], spectra[0][-1]])
    plt.legend()
    plt.xlabel('Frequency [Hz]')
    plt.ylabel('$$\mathrm{Hz} \cdot \mathrm{pk}$$')
    plt.title("Laser frequency noise from measured voltage noise")
    plt.savefig(new_final_dir + '/Hz' + '_spectra_' + labl + '.png', \
    dpi=300, bbox_inches='tight')
    plt.close()

```

Cavity params

```
[27]: c = 299792458 #_
    ↳ Cavity parameters
lamb = 1.064e-6
nu = c/lamb
Lcav = cav_length
```

Calibrate voltage to displacement

```
[28]: #Displacement spect
displac_spect = freq_noise*Lcav/nu #_
    ↳ Calibrate to displacement spectra
if meas_type == 'swept':
    disp_spect_norm = displac_spect/v_direct #_
    ↳ Displacement spectra normalized by the frequency dependent injection (leaves us with mpk/Vpk)
```

```

model_freq = 10000 #_
    ↳ Model estimate
marty_estimate = 3.8e-16 #_
    ↳  $mpk/[V*m]$ 
Efield_strength_estimate = 4648 #_
    ↳  $[V/m]$  (changed from 6350 to 4648 on 07-13-2021)

#Displacement spectra
if meas_type == 'swept': #_
    ↳ Organizing and plotting displacement spectra
        displac_spect_unnorm = [meas_swept[0], abs(displac_spect), \
            np.angle(displac_spect, deg=True)]
        displac_spect_norm = [meas_swept[0], abs(disp_spect_norm), \
            np.angle(disp_spect_norm, deg=True)]
        final_fig = bode_plt(displac_spect_unnorm, new_final_dir, \
            date.replace('_', '\_'), \
            'Displacement spectra for AlGaAs Pockels effect measurement', \
            ylbl='Displacement [ $\mathrm{m} \cdot \mathrm{pk}$ ]')
    else:
        final_fig = plt.loglog(spectra[0],abs(displac_spect),color='m', \
            label=lbl, linewidth=3)
        plt.xlabel('frequency [Hz]')
        #plt.xlim([spectra[0][0], spectra[0][-1]])
        #plt.ylabel('$V_{\mathrm{rms}}$'.format(spectra_type))

if model == True and meas_type != 'swept': #_
    ↳ If model estimate is requested, will plot model estimate with data
        plt.axhline(y=marty_estimate*Efield_strength_estimate,linestyle='--', \
            color='k', label='Marty estimate')
        #plt.xlim([spectra[0][0], spectra[0][-1]])
        plt.legend()
        plt.xlabel('Frequency [Hz]')
        if spectra_type == 'pk':
            plt.ylabel('Displacement [ $\mathrm{m} \cdot \mathrm{pk}$ ]')
        if spectra_type == 'rms':
            plt.ylabel('Displacement [ $\mathrm{m} \cdot \mathrm{rms}$ ]')
        plt.title("Displacement spectra for AlGaAs Pockels effect measurement")
        plt.savefig(new_final_dir + '/' + 'pockels_displacement_spectra' + \
            lbl + '.png',dpi=300,bbox_inches='tight')

```

CHAPTER 5. APPENDIX

Save raw data, calibration functions, calibrated displacement function, and other metadata

```
[29]: with h5py.File(new_final_dir + "/data.hdf5", "a") as f: #_
    ↳ Store raw / calibrated data along with metadata in data directory

        #Raw data
        raw = f.create_group("raw")
        hva_save = f.create_group("raw/hva") #_
        ↳ where hva data will be saved
        hva_save_ch3 = f.create_group("raw/hva/ch3+pomona")
        if meas_type == 'swept':
            freq = f.create_dataset("freq", data=meas_swept[0]) #_
        ↳ common frequency vector
        hva_save_ch1 = f.create_group("raw/hva/ch1")
        hva_save_ch1.attrs['dir'] = HVA_CH1_dir
        pomona_vdiv=f.create_dataset("pomona_vdivider",data=pom_vdivider) #_
        ↳ Voltage divider factor
        trans_func = f.create_group("raw/meas_freq_resp")
        meas_db = f.create_dataset("raw/meas_freq_resp/db", \
        data=meas_swept[1])
        meas_deg = f.create_dataset("raw/meas_freq_resp/deg", \
        data=meas_swept[2])
        trans_func.attrs['dir'] = meas_data_dir
        direc_volt = f.create_group("raw/vdirect") #_
        ↳ the Vpk voltage and phase information of the signal directly sent to the electrodes
        ↳ electrodes
        else:
            freq = f.create_dataset("freq", data=spectra[0]) #_
        ↳ common frequency vector
            vdata_save = f.create_dataset("raw/v_spect", data=spectra[1])
            vdata_save.attrs['units'] = spectra_type
            vdata_save.attrs['dir'] = meas_data_dir #_
        ↳ where error signal spectra will be saved
            cav_length = f.create_dataset("cav_length", data=Lcav)
            laser_freq = f.create_dataset("laser_freq", data=nu)
            laserPZTresp = f.create_dataset("laserV2Hz", data=laserV2Hz )
            hva_save_ch3.attrs['dir'] = HVA_dir
            olg_save = f.create_group("raw/olg") #_
        ↳ where olg data will be saved
            cal_save = f.create_group("raw/cal") #_
        ↳ easily accessible loop calibration factor data
            olg_save.attrs['dir'] = OLG_dir
            if meas_type == 'swept':
                hvadb_save_ch1 = f.create_dataset("raw/hva/ch1/db",data=HVA_CH1[1])
                hvadeg_save_ch1 = f.create_dataset("raw/hva/ch1/deg", \
```

```

    data=HVA_CH1[2])
    vdirec_db = f.create_dataset("raw/vdirect/db", data=vdirec[1])
    vdirec_deg = f.create_dataset("raw/vdirect/deg", data=vdirec[2])
hvadb_save_ch3 = f.create_dataset("raw/hva/ch3+pomona/db", \
data=HVA_inter[1])
hvadeg_save_ch3 = f.create_dataset("raw/hva/ch3+pomona/deg", \
data=HVA_inter[2])
olgdb_save = f.create_dataset("raw/olg/db", data=OLG_inter[1])
olgdeg_save = f.create_dataset("raw/olg/deg", data=OLG_inter[2])
calgain_save = f.create_dataset("raw/cal/gain", data=abs(CAL))
caldeg_save = f.create_dataset("raw/cal/deg", data=np.angle(CAL, \
deg=True))

#Calibrated data
calibra = f.create_group("calibrated")
hvatf_save = f.create_group("calibrated/hva")
hvach3tf_save = f.create_dataset("calibrated/hva/ch3+pomona",\
data=HVA_tf)
olgtf_save = f.create_dataset("calibrated/olg",data=OLG_tf)
freqnoise_save = f.create_dataset("calibrated/HzpV",data=CALHzpV)
if meas_type == 'swept':
    hvach1tf_save = f.create_dataset("calibrated/hva/ch1",\
data=HVA_CH1_tf)
    displacement_spect = f.create_dataset("calibrated/disp_spect_unnorm"\,
    , data=displac_spect_unnorm[1])
    phase_resp1 = f.create_dataset("calibrated/phase_resp_unnorm", \
    data=displac_spect_unnorm[2])
    displacement_spect_norm = \
        f.create_dataset("calibrated/disp_spect_norm", \
        data=displac_spect_norm[1])
    displacement_spect_norm.attrs['units'] = 'm' + spectra_type + '/Vpk'
    phase_resp2 = f.create_dataset("calibrated/phase_resp_norm", \
    data=displac_spect_norm[2])

else:
    displacement_spect = f.create_dataset("calibrated/disp_spect",\
    data=displac_spect)
    displacement_spect.attrs['units'] = spectra_type
    displacement_spect.attrs['meas_type'] = meas_type
f.close()

```

5.6 Single frequency

5.7 Laplace calculator / code

Snippets of explicit code with a block diagram for clarity

5.8 HVA

5.9 FSS

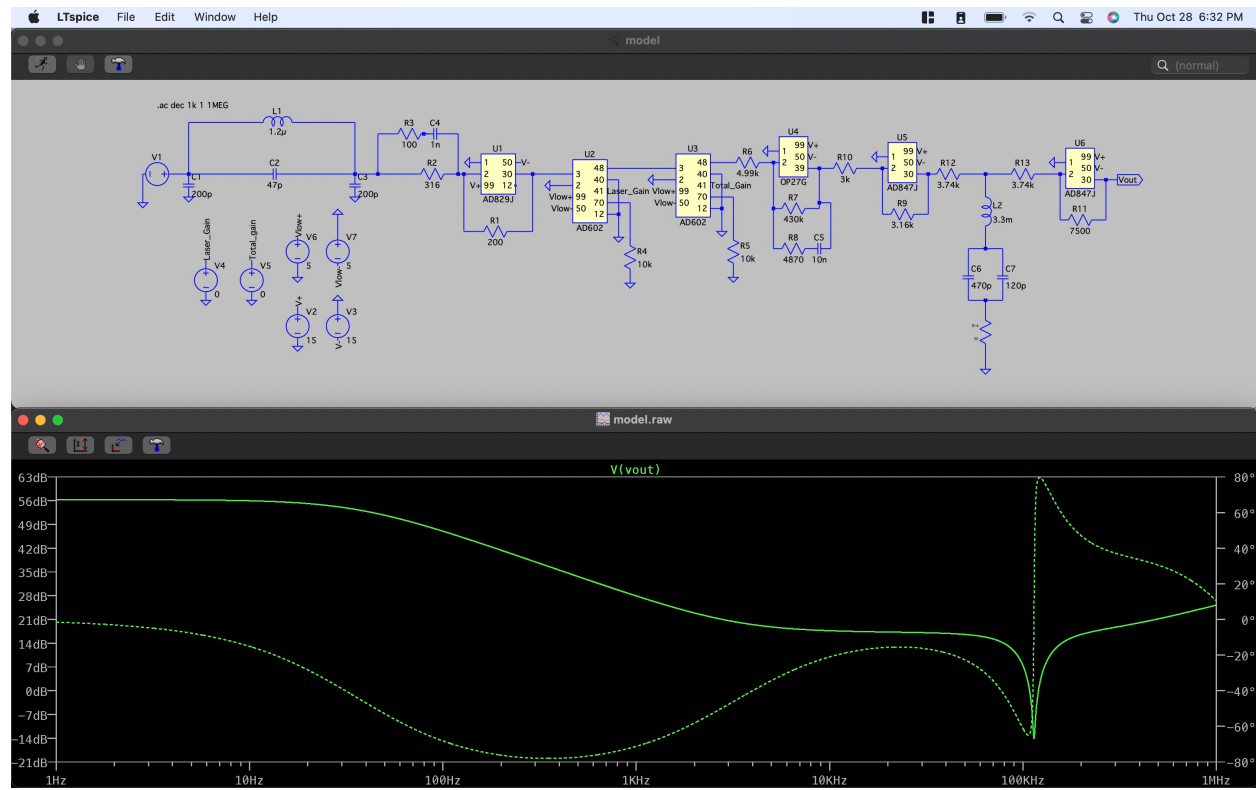


Figure 5.10: The FSS frequency response simulated in LTspice

5.10 Measuring OLG [H]

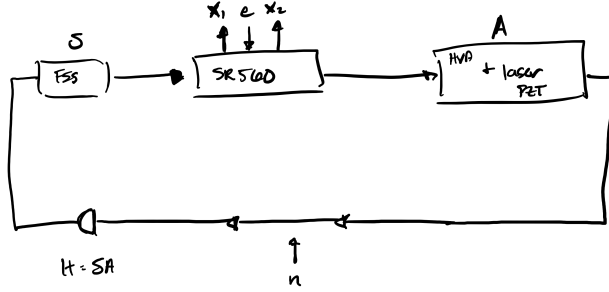


Figure 5.11: Open loop gain measurement drawn diagram

x2 is the PSD taken immediately after the excitation point

$$x_2 = e + He + H^2e + \text{H.O.T.s} = \frac{e + n}{1 - H} \quad (5.1)$$

x1 is the PSD taken immediately prior to the excitation point

$$x_1 = He + H^2e + H^3e + \text{H.O.T.s} = \frac{He}{1 - H} \quad (5.2)$$

We take the transfer function measurement ζ :

$$\zeta = \frac{x_1}{x_2} = \frac{He/(1 - H)}{(e + n)/(1 - H)} \quad (5.3)$$

Assuming the excitation is significantly larger than the noise ($e \gg n$):

$$\zeta \approx H \quad (5.4)$$

References

- [1] C. W. Misner, K. S. Thorne, and J. A. Wheeler, *Gravitation*. 1973.
- [2] P. Saulson, *Interferometric Gravitational Wave Detectors (2nd edition)*. World Scientific Publishing Co. Pte. Ltd., 2017.
- [3] P. R. Saulson, “If light waves are stretched by gravitational waves, how can we use light as a ruler to detect gravitational waves?,” *American Journal of Physics*, vol. 65, no. 6, pp. 501–505, 1997.
- [4] A. J. Mullavey, B. J. J. Slagmolen, J. Miller, M. Evans, P. Fritschel, D. Sigg, S. J. Waldman, D. A. Shaddock, and D. E. McClelland, “Arm-length stabilisation for interferometric gravitational-wave detectors using frequency-doubled auxiliary lasers,” *Opt. Express*, vol. 20, pp. 81–89, Jan 2012.
- [5] R. B. F. H. M. . R. A. V.P.L.S., “Xvii. a brief account of microscopical observations made in the months of june, july and august 1827, on the particles contained in the pollen of plants; and on the general existence of active molecules in organic and inorganic bodies,” *The Philosophical Magazine*, vol. 4, no. 21, pp. 161–173, 1828.
- [6] H. B. Callen and T. A. Welton, “Irreversibility and generalized noise,” *Phys. Rev.*, vol. 83, pp. 34–40, Jul 1951.
- [7] C. Zener, *Elasticity and Anelasticity of Metals*. University of Chicago Press, 1948.

- [8] Y. Levin, “Internal thermal noise in the ligo test masses: A direct approach,” *Physical Review D*, vol. 57, p. 659–663, Jan 1998.
- [9] T. Hong, H. Yang, E. K. Gustafson, R. X. Adhikari, and Y. Chen, “Brownian thermal noise in multilayer coated mirrors,” *Physical Review D*, vol. 87, Apr 2013.
- [10] G. M. Harry, H. Armandula, E. Black, D. R. M. Crooks, G. Cagnoli, J. Hough, P. Murray, S. Reid, S. Rowan, P. Sneddon, M. M. Fejer, R. Route, and S. D. Penn, “Thermal noise from optical coatings in gravitational wave detectors,” *Appl. Opt.*, vol. 45, pp. 1569–1574, Mar 2006.
- [11] G. D. Cole, W. Zhang, M. J. Martin, J. Ye, and M. Aspelmeyer, “Tenfold reduction of brownian noise in high-reflectivity optical coatings,” *Nature Photonics*, vol. 7, no. 8, pp. 644–650, 2013.
- [12] J. Ramette, M. Kasprzack, A. Brooks, C. Blair, H. Wang, and M. Heintze, “Analytical model for ring heater thermal compensation in the advanced laser interferometer gravitational-wave observatory,” *Appl. Opt.*, vol. 55, pp. 2619–2625, Apr 2016.
- [13] P. Hello and J.-Y. Vinet, “Analytical models of thermal aberrations in massive mirrors heated by high power laser beams,” *Journal de Physique*, vol. 51, pp. 1267–1282, 1990.
- [14] T. Vo, *Adaptive Mode Matching in Advanced LIGO and beyond*. PhD thesis, Syracuse NY, 2019.
- [15] M. Abernathy, “Noise in crystalline coatings,” Tech. Rep. G1401060-v1, LIGO Scientific Collaboration, August 2014.
- [16] J. F. Nye, *Physical properties of crystals (Their representation by tensors and matrices)*. Oxford University Press, 1985.
- [17] A. Yariv, *Quantum Electronics (3rd. ed)*. John Wiley & Sons, 1989.

REFERENCES

- [18] M. F. Edgard Bonilla, “Optical phase perturbations on the reflected wave of a dielectric mirror. application to the electro-optic effect in algaas coatings,” Tech. Rep. T1800528-v1, LIGO Scientific Collaboration, December 2018.
- [19] S. W. Ballmer, “Photothermal transfer function of dielectric mirrors for precision measurements,” *Physical Review D*, vol. 91, Jan 2015.
- [20] G. Mansell, “Electric field meter not coherent with darm (lho elog 56416).”
<https://alog.ligo-wa.caltech.edu/aLOG/index.php?callRep=56416>.
- [21] Corning, *MACOR (Machinable glass ceramic for industrial applications)*, 2012.
Available at <https://www.corning.com/media/worldwide/csm/documents/71759a443535431395eb34ebead091cb.pdf>.
- [22] A. W. Leissa, *Vibration of Plates*. National Aeronautics and Space Administration Special Publication (SP), 1969.